

ESD ACCESSION LIST

ESTI Call No. 70700

Copy No. 1 of 2 cys.

**ESD RECORD COPY**

RETURN TO  
SCIENTIFIC & TECHNICAL INFORMATION DIVISION  
(ESTI), BUILDING 1211

2

Solid State Research

1970

Prepared under Electronic Systems Division Contract AF 19(628)-5167 by

**Lincoln Laboratory**

MASSACHUSETTS INSTITUTE OF TECHNOLOGY

Lexington, Massachusetts



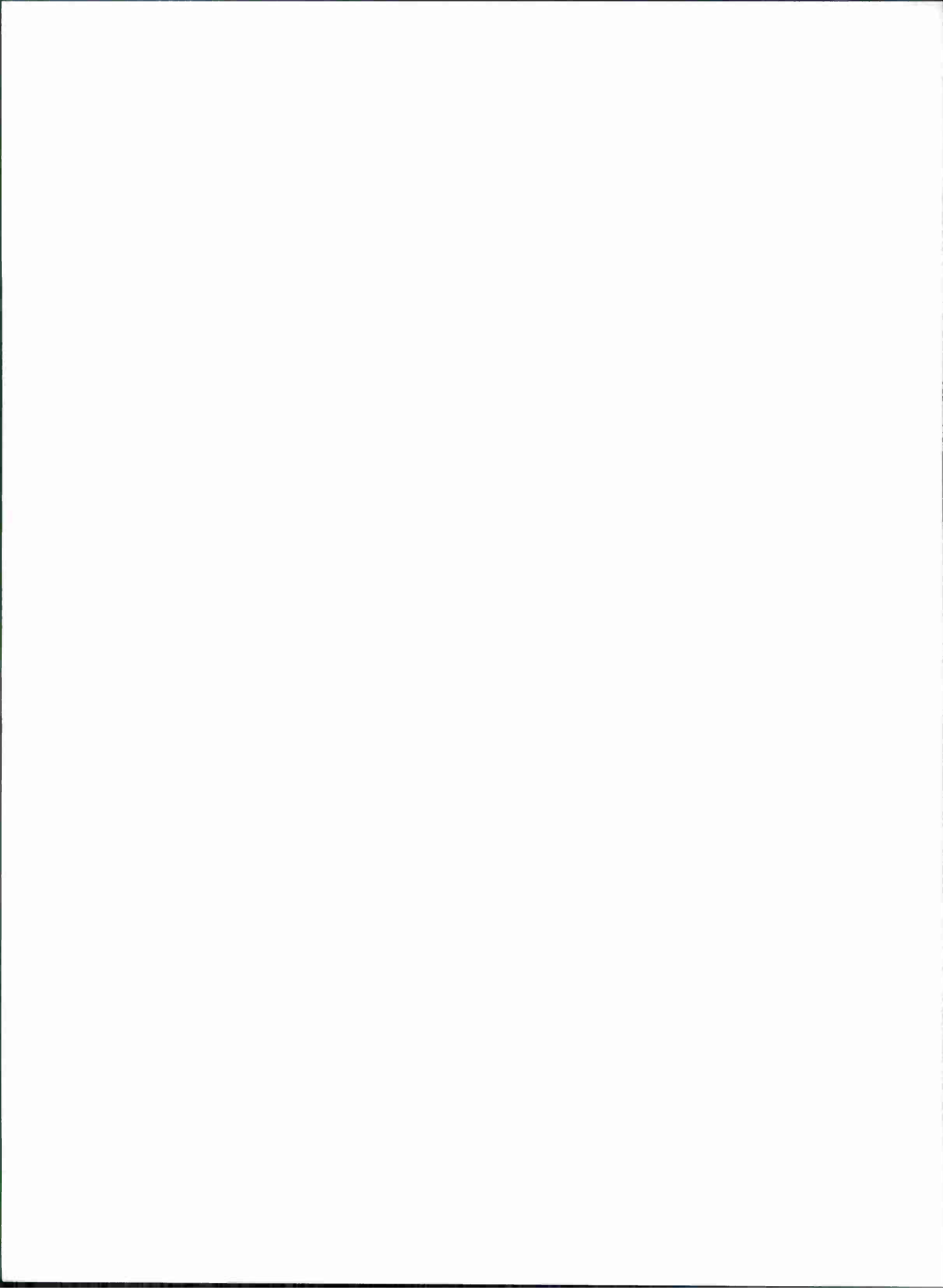
AD711074

This document has been approved for public release and sale;  
its distribution is unlimited.

## ABSTRACT

This report covers in detail the solid state research work of the Solid State Division at Lincoln Laboratory for the period 1 February through 30 April 1970. The topics covered are Solid State Device Research, Materials Research, Physics of Solids, and Microelectronics. The Microsound work is sponsored by ABMDA and is reported under that program.

Accepted for the Air Force  
Franklin C. Hudson  
Chief, Lincoln Laboratory Office



# INTRODUCTION

## I. SOLID STATE DEVICE RESEARCH

Three high purity epitaxial GaAs samples have been evaluated as far infrared detectors under different background conditions. Spectral response measurements at 4.2° and 1.93°K indicate that the long wavelength response from 200 to 350 $\mu$  is due primarily to a combined photo-thermal excitation process. The conductivity and thus the performance characteristics of the detectors consequently depend critically on both the detector temperature and background radiation. The best long wavelength response was observed at 4.2°K in reduced background.

Long wavelength laser emission at 28 $\mu$  has been observed from Schottky barrier diodes fabricated by evaporating Pb contacts on Bridgman-grown  $Pb_{0.715}Sn_{0.285}Te$ . The material used was  $4.5 \times 10^{17} \text{ cm}^{-3}$  p-type and was obtained as part of a study of the preparation and characterization of metal saturated  $Pb_{1-x}Sn_xTe$  as a function of isothermal annealing temperatures.

N-p junction photovoltaic detectors have been fabricated in p-type  $Hg_{0.5}Cd_{0.5}Te$  using proton bombardment to create the n-type region. The photovoltaic response of these diodes peaks at 1.8 $\mu$  with a quantum efficiency of 15 percent. The 300°K detectivity at the peak is  $2 \times 10^{10} \text{ cm Hz}^{1/2}/\text{W}$ .

A vidicon type television camera tube has been constructed employing an array of reverse biased GaAs Schottky barrier photodiodes to form the image sensing target. This target has many advantages over a conventional photoconductive vidicon target, and its simplicity of fabrication and stability make it an attractive alternative to the silicon p-n photodiode array target.

A new technique has been developed for the fabrication of semiconductor devices utilizing a thin semiconductor layer. The advantage of this is that different parts of the devices can be fabricated on both sides of the layer in close proximity to each other adding an additional dimension to the fabrication technology. The technique has been used to fabricate GaAs Schottky barrier field effect transistors in which the source and drain ohmic contacts separated by 5 $\mu$  are on one side of an 0.5- $\mu$  thick layer of GaAs and the 5 $\mu$  long Schottky barrier gate is on the opposite side positioned over the source-drain gap. This structure and others utilizing this technique should result in improved high frequency performance of many semiconductor devices.

Acousto-electric amplification coefficients have been measured at room temperature over the frequency range from 1.23 to 3.75 GHz in  $5 \times 10^{14} \text{ cm}^{-3}$  n-type GaAs using Brillouin scattering. Good agreement with theory is observed for the absolute value of the gain coefficient over this range and for the frequency of maximum gain.

## Introduction

## II. MATERIALS RESEARCH

A new seed rod, cooled by means of a heat pipe, has been used for pulling crystals in the tri-arc Czochralski furnace. Use of the heat pipe, a device in which extremely efficient heat transfer is accomplished by the evaporation and condensation of a volatile liquid, eliminates the disadvantages encountered with a water-cooled seed rod.

Single crystals of CdO with dimensions up to about  $5 \times 5 \times 8$  mm have been grown from the vapor phase at about  $1050^{\circ}\text{C}$  by an open tube method in which a stream of helium saturated with cadmium vapor is mixed with an oxygen stream inside a cylindrical liner made of high purity  $\text{Al}_2\text{O}_3$ .

Charts of the standard free energy of formation ( $\Delta G_f^{\circ}$ ) as a function of temperature have been constructed for binary selenides and tellurides on the basis of published thermodynamic data. No charts of this type have previously been available for these compounds.

The effects of deviations from stoichiometry on the lattice parameter and electrical resistivity of EuO have been confirmed by measurements on europium-saturated and oxygen-saturated single crystals. A marked increase in the optical transmission of EuS and EuSe single crystals grown from europium-rich solutions has been achieved by annealing the crystals in sealed tungsten crucibles.

Optical transmission measurements on  $\text{ZnTe}_{1-x}\text{Se}_x$  single crystals have confirmed the existence of an energy gap minimum in this alloy system. Similar measurements demonstrate a strongly nonlinear dependence of energy gap on composition in the  $\text{ZnTe}_{1-x}\text{S}_x$  alloys, although no minimum can be observed because the mutual solubility of ZnTe and ZnS is too low.

Optical transmission measurements on  $\text{CdTe}_{1-x}\text{Se}_x$  single crystals have established the existence of an energy gap minimum in this alloy system. The data indicate that the energy gap for a given composition is about 0.03 eV higher for samples with the hexagonal wurtzite structure than for those with the cubic zincblende structure.

An energy level scheme which takes account of the role of cation vacancies has been proposed for NiO. This scheme accounts for the optical and electrical properties of both undoped and Li-doped NiO.

The polaron morphology in vanadium spinels has been investigated by analyzing the observed variation in Seebeck coefficient with composition in the systems  $\text{Mg}[\text{B}_x^{2+}\text{V}_{2-x}]_{\text{O}}_4$  where B = Mg or Ni. The results indicate that with decreasing V-V separation (R), the polarons change from  $\text{V}^{4+}$  cations to  $\text{V}_2$ -cluster and  $\text{V}_4$ -cluster polarons, and finally to itinerant electrons, in a narrow range  $2.99 > R > 2.94 \text{ \AA}$ .

Integrated intensity data obtained in x-ray diffraction measurements on powdered samples have been used to carry out a structure refinement for the hexagonal (6H) form of  $\text{RbNiF}_3$ . The results are generally in agreement with published values, but there are significant discrepancies in the positions of the fluorine atoms.

The effect of high pressure on the crystal structure of  $\text{CsMnCl}_3$ ,  $\text{RbMnCl}_3$ , and  $\text{RbFeCl}_3$  has been determined by means of x-ray diffraction measurements. For each compound, the

proportion of hexagonal close packing decreases with increasing pressure, and the ultimate high pressure form has the perovskite structure, which is entirely cubic close packed.

The sources of error in measuring volume compression by means of x-ray diffraction studies at high pressures have been analyzed. The procedures required to obtain accurate lattice parameters for the sample and for a marker material such as NaCl used to determine the applied pressure, are discussed in detail.

The volume compression of  $TiO_x$  for samples with  $x$  between 0.83 and 1.25 has been investigated by means of x-ray diffraction studies made with diamond-anvil high pressure units. For pressures up to 140 kbars, the measured values of  $-V/V_0 \Delta P$  are between  $2.3 \times 10^{-4}$  and  $4.0 \times 10^{-4} \text{ kbar}^{-1}$ .

### III. PHYSICS OF SOLIDS

The quasi-particle approach to the optical properties of simple metals has now been applied to the calculation of the optical properties of potassium. Using nonlocal pseudopotentials and the experimental Fermi surface, both the photon energy threshold for interband absorption and the magnitude of the absorption have been calculated.

Work on  $Ti_2O_3$  continues. In an attempt to describe the nature of the insulator-metal transition, a model based on the competition between elastic and electronic free energies of the system as a function of temperature, is being investigated. Although this model is capable of giving a reasonable description of the change in c/a ratio with temperature, it predicts a very pronounced "mode softening" in the vicinity of the transition which is inconsistent with our Raman scattering data.

A mechanism for the description of a metal to semiconductor transition with increasing temperature has been found. The result is based on a comparison of the free energy for localized (Wannier) vs band (Bloch) states for a half-filled band Hubbard Hamiltonian.

The phonon pinning spectrum of an electron bound to an impurity in a semiconductor, as affected by the presence of the impurity, is under study. A preliminary calculation indicates pinning due to interaction with local or resonant modes, as well as pinning due to lattice modes.

A band theory of optical activity, which arises from terms in the dielectric constant linear in  $q$ , has been developed. The general results, when reduced to a simple four-band model, give a value for the ratio of rotary power parallel and perpendicular to the c-axis which is close to our previously measured ratio in  $\alpha$ -quartz.

Work on the magnetic semiconductor EuO has now been extended to studies of magnetic properties in the vicinity of the Curie temperature. Measurements have been analyzed to determine the magnetic critical indices.

In other magnetic work the study of two-magnon Raman scattering in  $KNiF_3$  has been extended to samples doped with  $Mn^{2+}$  impurities. In addition to the intrinsic two-magnon excitation previously observed in pure samples, a new, relatively narrow line has been observed, with

## Introduction

an intensity that is dependent on the Mn<sup>2+</sup> concentration. The line is tentatively identified as a resonant two-magnon state associated with an Mn<sup>2+</sup> impurity. The Raman spectrum of the antiferromagnet CsMnF<sub>3</sub> has been observed using the 4880-Å radiation from an argon laser. In addition to the active phonon modes, a mode has been observed whose shape, position, temperature dependence and polarization indicate that it arises from the excitation of two magnons.

Theoretical work on light scattering from acoustic plasma waves and single electron excitations in magnetoplasmas continues. A model calculation, involving only scattering due to density fluctuations and ignoring spin-orbit coupling, has been carried out to illustrate some of the general features of magnetoplasma quasi-elastic scattering.

In another phase of the laser program, heterodyne experiments with both millimeter and infrared sources have been performed in high purity, epitaxial GaAs. The millimeter waves produce avalanche breakdown, and mixing via hot electrons is observed. At laser frequencies the DC bias level determines whether detection proceeds via a similar hot electron mechanism or through photothermal ionization of shallow donor states. The time constant associated with the latter process is significantly faster than that of hot carrier relaxation.

Two nonlinear effects on the polarization and linewidth of an intense broadband maser signal have been calculated with application to the interstellar masers. One is the competition between opposite circularly polarized Zeeman modes by means of parametric down-conversion involving an electron cyclotron idler wave. The second is the saturation broadening in a two-level system due to a broadband signal having Gaussian statistics.

## IV. MICROELECTRONICS

The Microelectronics Group, which is now part of the Solid State Division, has a dual charter of service and research in integrated electronics. Service tasks have provided an opportunity to apply new processes and techniques that have been developed as part of the research program on integrated circuits. Typically, at any one time there are about 20 active programs ranging from special semiconductor devices to large hybrid integrated assemblies. In addition, about five or six research programs are in progress as long range support for Lincoln Laboratory programs.

The present programs in research and development include the following:

- (1) Rigid and nonrigid forms of beam lead substrates have been fabricated with gold and more recently with aluminum metallization for the beams and air gap crossovers. Some work remains to be done to improve yield and cost reduction in the fabrication and assembly of the substrates, but the basic techniques are developed for several forms of substrates including an automated version.
- (2) Aluminum beam leaded silicon chips have been developed as a complementary assembly method to the beam lead substrates. Air gap crossovers using aluminum metallization on the silicon chips also look promising as a means of providing an additional and high yield interconnection method at the chip level.

- (3) A silicon dioxide passivation method for mesa semiconductor devices has been developed which has several advantages over present passivation methods. Actual devices have been fabricated using this technique with excellent results.
- (4) A development effort on Impatt and Trapatt microwave devices with special geometries has been pursued during the past year. New packaging and die attachment techniques are being investigated to reduce the thermal coefficient and improve the efficiency.
- (5) A laser scanner for mask inspection and semiconductor chip evaluation has been built and tested. Improvements in the scanning mechanism are under way which will allow faster scanning. Metallization faults, mask misalignment, diffusion faults and oxide problems and device gain characteristics can be examined with the scanner.

Other programs that are more applications oriented and include some research or development are listed below.

- (1) A strip or an array of 64 silicon photodiodes spaced 6 mils on centers has been developed for a satellite stabilization system. Two approaches have been taken: one method employs 4 strips of 64 diodes assembled very accurately in a single package, and a second method employs a redundancy and discretionary wiring to allow the fabrication of the four diode arrays on a single silicon wafer.
- (2) Special diodes with very shallow junctions ( $0.5 \mu$ ) have been fabricated for use in high power applications with an electron beam as the input control. These devices hopefully will compete favorably with magnetrons and traveling wave tubes in power and frequency. Present results indicate an oxide charging problem and lower power capabilities than anticipated.
- (3) A multi-element particle detector using a silicon array is under development in cooperation with Dr. Kosta M. Tsipis (Laboratory for Nuclear Science, M.I.T.).

Other programs of a service nature that require moderate development are:

- (1) Surface wave transducer program.
  - (a) Fine line masks.
  - (b) Semiconductor amplifier substrates.
- (2) Microwave thin film assemblies.
- (3) Mixer diodes employing  $5-\mu$  Schottky barrier devices.

## CONTENTS

Abstract	iii
Introduction	v
Organization	xii
Reports by Authors Engaged in Solid State Research	xiii
<b>I. SOLID STATE DEVICE RESEARCH</b>	<b>1</b>
A. GaAs Far Infrared Detectors	1
B. Long Wavelength Metal-Semiconductor Barrier Laser on p-Pb <sub>0.715</sub> Sn <sub>0.285</sub> Te	5
C. Preparation of Material for Metal-Semiconductor Barrier Lasers	5
D. Type Conversion and n-p Junction Formation in Hg <sub>1-x</sub> Cd <sub>x</sub> Te Produced by Photon Bombardment	6
E. A Vidicon with a GaAs Schottky Barrier Diode Array Target	7
F. A New Technique for the Fabrication of GaAs Schottky Barrier Field Effect Transistors	7
G. Frequency Dependence of Acoustoelectric Amplification in n-GaAs	9
<b>II. MATERIALS RESEARCH</b>	<b>11</b>
A. Use of Heat Pipe in Crystal Pulling	11
B. Vapor Growth of CdO Single Crystals	12
C. Standard Free Energy Charts for Binary Selenides and Tellurides	14
D. Deviations from Stoichiometry in EuO	15
E. Composition Dependence of Energy Gap in ZnTe <sub>1-x</sub> Se <sub>x</sub> and ZnTe <sub>1-x</sub> S <sub>x</sub> Alloys	21
F. Energy Gap Minimum in CdTe <sub>1-x</sub> Se <sub>x</sub> Alloys	26
G. Energy-Level Scheme for Ni <sub>1-δ</sub> O:Li	29
H. Polaron Morphology in Vanadium Spinels from Seebeck Coefficients	31
I. Crystal Structure of Hexagonal RbNiF <sub>3</sub> (6H)	34
J. Effect of Pressure on Crystal Structure of CsMnCl <sub>3</sub> , RbMnCl <sub>3</sub> , and RbFeCl <sub>3</sub>	37
K. Volume Compression of TiO <sub>x</sub>	42

III. PHYSICS OF SOLIDS	47
A. Electronic Band Structure	47
1. Fermi Surface and Optical Properties of Potassium	47
2. Model of the Insulator-Metal Transition in $Ti_2O_3$	49
3. Variational Approach to the Metal-Semiconductor Transition	51
4. Interaction of Bound Electrons with Local and Resonant Modes in Semiconductors	52
5. Band Theory of Optical Activity	52
B. Magnetism	55
1. Critical Magnetic Properties of EuO	55
2. Impurity Magnon Modes in $KNiF_3:Mn$	57
3. Raman Scattering in $CsMnF_3$	58
C. Laser Scattering	58
1. Light Scattering from Acoustic Plasma Waves and Single-Electron Excitations in Magnetoplasmas	58
2. Millimeter and Far Infrared Frequency Mixing in GaAs	62
3. Nonlinear Effects on the Polarization and Linewidth of Intense Broadband Maser Signals	64
IV. MICROELECTRONICS	67
A. Aluminum Beam Leads and Beam-Lead Crossovers on Ceramic	67
B. Passivated Mesa Technique	68
C. Computer Aided Design and Development	70

# ORGANIZATION

## SOLID STATE DIVISION

A. L. McWhorter, *Head*  
P. E. Tannenwald, *Associate Head*  
C. R. Grant, *Assistant*  
E. P. Warekois

### SOLID STATE THEORY

H. J. Zeiger, *Leader*  
M. M. Litvak, *Assistant Leader*

Bari, R. A. Landon, S. N.  
Brine, N. S. Larsen, D. M.  
Brodersen, R. W.\* Ngai, K. L.  
Davies, R. W. Palm, B. J.  
Dresselhaus, G. F. Wilson, A. R.  
Kaplan, T. A. Young, C. Y.

### ELECTRONIC MATERIALS

J. B. Goodenough, *Leader*  
A. J. Strauss, *Associate Leader*

Anderson, C. H., Jr. Longo, J. M.  
Banus, M. D. Mastromattei, E. L.  
Batson, D. A. Owens, E. B.  
Brebrick, R. F., Jr. Pierce, J. W.  
Button, M. J. Plonko, M. C.  
Capes, R. N. Raccah, P. M.  
Delaney, E. J. Reed, T. B.  
England, R. E. Roddy, J. T.  
Fahey, R. E. Searles, I. H.  
Finn, M. C. Smith, F. T. J.  
Iseler, G. W. Stack, T. E.  
Kafalas, J. A. Steininger, J. M.  
LaFleur, W. J. Temkin, R. J.\*  
Lavine, M. C.†

### MICROELECTRONICS

R. E. McMahon, *Leader*

Bachner, F. J. Johnson, D. H.  
Beatrice, P. A. McBride, W. F.  
Childs, N. B. Mountain, R. W.  
Cohen, R. A. Pichler, H. H.  
Grant, L. G. Pybus, V. J.  
Gray, R. V. Wilde, R. E.

### SOLID STATE PHYSICS

J. G. Mavroides, *Leader*  
G. B. Wright, *Assistant Leader*

Allen, J. W. Henrich, V. E.  
Barch, W. E. Johnson, E. J.  
Blum, F. A. Kernan, W. C.  
Brandt, R. C. Kolesar, D. F.  
Burke, J. W. Melngailis, J.  
Chinn, S. R. Menyuk, N.  
DeFeo, W. E. Nill, K. W.  
Dresselhaus, M. S.† Parker, C. D.  
Dwight, K., Jr. Pine, A. S.  
Feldman, B. Scouler, W. J.  
Fetterman, H. Waldman, J.\*  
Groves, S. H. Weber, R.

### APPLIED PHYSICS

J. O. Dimmock, *Leader*  
T. C. Harman, *Assistant Leader*  
I. Melngailis, *Assistant Leader*

Belanger, L. J. Mooradian, A.  
Brueck, S.\* Murphy, R. A.\*  
Calawa, A. R. Oliver, M. R.\*  
Carter, F. B. Orphanos, W. G.  
Caswell, F. H. Paladino, A. E.  
Clough, T. F. Rossi, J. A.  
Donnelly, J. P. Spears, D. L.  
Ferrante, G. Stillman, G. E.  
Foyt, A. G. Ward, J. H. R., III  
Hurwitz, C. E. Wolfe, C. M.  
Krohn, L. Woods, R.  
Lindley, W. T. Youtz, P.

### MICROSOUND

E. Stern, *Leader*

Alusow, J. A. Murray, T. A.  
Burke, B. E. Smith, H. I.  
Chen, F. Waldron, R. A.

\* Research Assistant

† Part Time

# REPORTS BY AUTHORS ENGAGED IN SOLID STATE RESEARCH

15 February through 15 May 1970

## PUBLISHED REPORTS

### Journal Articles\*

#### JA No.

3281	Crystallographic and Magnetic Properties of Perovskite and Perovskite-Related Compounds	J. B. Goodenough J. M. Longo	<u>Landolt-Bornstein Tables</u> , Group III, <u>4</u> , Part A (Springer, Berlin, 1970), p. 126
3412A	Experimental Comparison of Hartree-Fock and Slater Exchange Potentials in Aluminum from the Charge Density Point of View	P. M. Raccah V. E. Henrich	Intl. J. Quant. Chem. <u>III S</u> , 797 (1970)
3498	Polarons Bound in a Coulomb Potential. I. Ground State	D. M. Larsen	Phys. Rev. <u>187</u> , 1147 (1969)
3501	Evidence for a Native Donor in ZnSe from High Temperature Electrical Measurements	F. T. J. Smith	Solid State Commun. <u>7</u> , 1757 (1969)
3517	Resonant Raman Scattering from LO Phonons in Polar Semiconductors	D. C. Hamilton	Phys. Rev. <u>188</u> , 1221 (1969)
3521	Ionized Impurity Density in n-type GaAs	C. M. Wolfe G. E. Stillman J. O. Dimmock	J. Appl. Phys. <u>41</u> , 504 (1970)
3524	Inelastic Light Scattering from Semiconductor Plasmas in a Magnetic Field	F. A. Blum	Phys. Rev. B, <u>1</u> , 1125 (1970)
3528	Linear Wave-Vector Shifts in the Raman Spectrum of $\alpha$ -Quartz and Infrared Optical Activity	A. S. Pine G. Dresselhaus	Phys. Rev. <u>188</u> , 1489 (1969)
3577	Reinterpretation of $^4A_2 \rightarrow ^2E$ Exciton Spectra in $YCrO_3$	J. W. Allen	Solid State Commun. <u>8</u> , 53 (1970)
3580	Electrically Active Point Defects in Cadmium Telluride	F. T. J. Smith	Metallurgical Trans. <u>1</u> , 617 (1970)

---

\* Reprints available.

Reports

JA No.

3591	Comparison of Theoretical and Experimental Charge Densities for C, Si, Ge, and ZnSe	P. M. Raccah R. N. Euwema* D. J. Stukel* T. C. Collins*	Phys. Rev. B, <u>1</u> 756 (1970)
3606	High Temperature Electrical Properties of CdSe: Evidence for a Native Donor	F. T. J. Smith	Solid State Commun. <u>8</u> , 263 (1970)
3625	Report on the Symposium on Magnetic Semiconductors held in Yorktown Heights, New York, Nov. 1969	J. O. Dimmock	Appl. Optics <u>9</u> , 438 (1970)
3650	Pressure-Induced Pyrochlore to Perovskite Transformations in the $\text{Sr}_{1-x}\text{Pb}_x\text{RuO}_3$ System	J. A. Kafalas J. M. Longo	Mat. Res. Bull. <u>5</u> , 193 (1970)
3660	Pressure Dependence of the Electrical Resistivity of EuO	M. R. Oliver J. A. Kafalas J. O. Dimmock T. B. Reed	Phys. Rev. Letters <u>24</u> , 1064 (1970)

MS No.

2387A	Some Applications of the Thermal Single Determinant Approximation	T. A. Kaplan P. N. Argyres	Intl. J. Quant. Chem. <u>III S</u> , 851 (1970)
2466	The Role of Oxygen Pressure in the Control and Measurement of Composition in 3d Metal Oxides	T. B. Reed	The Chemistry of Extended Defects in Non-Metallic Solids (North-Holland, Amsterdam, 1970)
2506	Structural, Electrical and Magnetic Properties of Vacancy Stabilized Cubic 'TiO' and 'VO'	M. D. Banus T. B. Reed	
2515	Evidence for a Continuous Sequence of Structures in the Bi-Te System	R. F. Brebrick	
2662	Two-Magnon Raman Scattering in $\text{KNiF}_3$	S. R. Chinn H. J. Zeiger J. R. O'Connor	J. Appl. Phys. <u>41</u> , 894 (1970)
2663	Multiplet Structure in the Reflectance Spectra of Europium Chalcogenides	J. O. Dimmock J. Hanus* J. Feinleib	J. Appl. Phys. <u>41</u> , 1088 (1970)

\* Author not at Lincoln Laboratory.

## MS No.

2666	Magnetic and Optical Properties of the High- and Low-Pressure Forms of $\text{CsCoF}_3$	J. M. Longo J. A. Kafalas J. R. O'Connor J. B. Goodenough	J. Appl. Phys. <u>41</u> , 935 (1970)
2668	Magnetic Ordering Effects in the Reflectance of EuO, EuS, EuSe and EuTe	W. J. Scouler J. Feinleib J. O. Dimmock T. B. Reed C. R. Pidgeon*	J. Appl. Phys. <u>41</u> , 1085 (1970)
2670	Theory of Localized vs. Band Magnetic Semiconductors	T. A. Kaplan R. A. Bari	J. Appl. Phys. <u>41</u> , 875 (1970)
2677	Onset of Magnetism in Vanadium Oxides: $^{51}\text{V}$ NMR Studies of VO	W. W. Warren, Jr.* A. C. Gossard* M. D. Banus	J. Appl. Phys. <u>41</u> , 881 (1970)
2679	Specific Heat of EuO	A. J. Henderson* G. R. Brown* T. B. Reed* H. Meyer*	J. Appl. Phys. <u>41</u> , 946 (1970)
2847	Lectures on Magnetism	N. Menyuk	Proceedings Winter School in Solid State Chemistry, Indian Institute of Technology, Kanpur, India, 26 November - 12 December 1969

\* \* \* \*

## UNPUBLISHED REPORTS

Journal Articles

## JA No.

3603A	Simple Model Potential Approach to the X-Ray Form Factor in Aluminum	P. Ascarelli* P. M. Raccah	Accepted by Phys. Letters
3618	Phase Diagram of the Zinc-Cadmium-Tellurium Ternary System	J. Steininger A. J. Strauss R. F. Brebrick	Accepted by J. Electrochem. Soc
3626	Simple, Versatile Techniques for Qualitative and Quantitative Evaluation of Spark Source Mass Spectrographic Plates	E. B. Owens	Accepted by Rev. Sci. Instr.
3633	Electron Mobility in High-Purity GaAs	C. M. Wolfe G. E. Stillman W. T. Lindley	Accepted by J. Appl. Phys.

\* Author not at Lincoln Laboratory.

Reports

JA No.

3645	Report on the Symposium on Magnetic Semiconductors, IBM Research Center, Yorktown Heights, N. Y.	J. B. Goodenough	Accepted by Phys. Today
3646	Quantitative Analysis of Ternary and Quaternary Semiconducting Alloys with the Electron Microprobe	M. C. Finn	Accepted by Anal. Chem.
3648	N-P Junction Photodetectors in InSb Fabricated by Proton Bombardment	A. G. Foyt W. T. Lindley J. P. Donnelly	Accepted by Appl. Phys. Letters
3651A	Anomalous Absorption of Microwaves by Interstellar H <sub>2</sub> CO	M. M. Litvak	Accepted by Astrophys. J. (Letters)
3657	X-ray Diffraction at High Pressures	M. D. Banus	Accepted by High Temperatures-High Pressures
3663	Crystal Structure of Hexagonal RbNiF <sub>3</sub> (6H)	R. J. Arnott* J. M. Longo	Accepted by J. Solid State Chem.
3672	Laser Emission from Metal-Semiconductor Contacts on PbTe and Pb <sub>0.8</sub> Sn <sub>0.2</sub> Te	K. W. Nill J. N. Walpole* A. R. Calawa T. C. Harman	Accepted by Appl. Phys. Letters
3681	Ultrasonic Attenuation Near the Spin-Alignment Transition of EuTe	Y. Shapira* T. B. Reed	Accepted by Phys. Letters
3684	Growth of EuO, EuS, EuSe and EuTe Single Crystals	T. B. Reed R. E. Fahey	Accepted by J. Cryst. Growth
3686	Polarized Maser Emission from Interstellar OH and H <sub>2</sub> O	M. M. Litvak	Accepted by Phys. Rev.
3691	Phase Transitions in Perovskite-Like Compounds of the Rare Earths	S. Geller* P. M. Raccah	Accepted by Phys. Rev.
3701	Analysis of Frozen Aqueous Solutions by Spark Source Mass Spectroscopy	E. B. Owens	Accepted by Anal. Letters

MS No.

2754	Narrow Gap Semiconductor Lasers	T. C. Harman	Accepted by J. Phys. Chem. Solids
2770	k · p Theory for the Conduction and Valence Bands of Pb <sub>1-x</sub> Sn <sub>x</sub> Te and Pb <sub>1-x</sub> Sn <sub>x</sub> Se	J. O. Dimmock	Accepted by J. Phys. Chem. Solids

\* Author not at Lincoln Laboratory.

## MS No.

2780	Raman Scattering from $Hg_xCd_{1-x}Te$	A. Mooradian T.C. Harman	Accepted by J. Phys. Chem. Solids
------	---	-----------------------------	-----------------------------------

Meeting Speeches

## MS No.

2420G	Recent Advances in Laser Spectroscopy	A. Mooradian	Physics Department Seminar, M.I.T., 8 April 1970
2496B-C	Pitfalls, Detours and Shortcuts on the Road to Single Crystal Growth	T.B. Reed	{ Regional Meeting of Electrochemical Society, Inc. New York, N.Y., 11 March 1970
			{ Materials Seminar, Northwestern University, Evanston, Illinois, 7 April 1970
2598A	Theory and Practice of Vapor Phase Crystal Growth	T.B. Reed	Materials Seminar, Case Western Reserve University, Cleveland, Ohio, 3 April 1970
2667A	A Gridded Thick Film Metalization Structure Employed in Multichip Circuit Fabrication	H.H. Pichler	NEPCON '70 West, 10-12 February 1970
2670A	Localized vs. Band Magnetic Semiconductors	T.A. Kaplan	Solid State Physics Seminar, General Electric Research and Development Center, Schenectady, N.Y., 12 March 1970
2702	Rigid and Nonrigid Beam Lead Substrates	R.E. McMahon F.J. Bachner R.A. Cohen	1970 IEEE International Solid State Circuits Conference Digest of Technical Papers, 18-20 February 1970
2720A	Spectroscopy of Shallow Donor Levels in GaAs Extrinsic Photodetectors	G.E. Stillman	Department of Physics Seminar, University of Illinois, 5 May 1970
2754	Narrow Gap Semiconductor Lasers	T.C. Harman	
2757	Metal-Semiconductor Contacts on $Pb_{1-x}Sn_xTe$	K.W. Nill J.N. Walpole * A.R. Calawa T.C. Harman	
2760	High-Resolution Magneto-spectroscopy of Graphite	P.R. Schroeder * M.S. Dresselhaus A. Javan *	
2763	Recent Experiments on Zero-Gap Semiconductors	S.H. Groves	Conference on Physics of Semimetals and Narrow Gap Semiconductors, Dallas, Texas, 20-21 March 1970

\* Author not at Lincoln Laboratory.

Reports

MS No.

2765	Electronic Properties of the Group V Semimetals	M. S. Dresselhaus	Conference on Physics of Semimetals and Narrow Gap Semiconductors, Dallas, Texas, 20-21 March 1970
2770	$k \cdot p$ Theory for the Conduction and Valence Bands of $Pb_{1-x}Sn_xTe$ and $Pb_{1-x}Sn_xSe$ Alloys	J. O. Dimmock	
2780	Raman Scattering from $Hg_xCd_{1-x}Te$	A. Mooradian T. C. Harman	
2754A	Narrow Gap Semiconductors	T. C. Harman	Materials Science Seminar, Purdue University, 12 May 1970
2740A	Magnetospectroscopy of Shallow Donors in CdTe	D. R. Cohn* B. Lax* D. M. Larsen	
2756	Shubnikov-deHaas Measurements in $Pb_{1-x}Sn_xTe$ Under Hydrostatic Pressure	J. Melngailis J. A. Kafalas T. C. Harman	
2776	Green's Function Theory of Strong Coupling Phonon Sideband Absorption	J. W. Allen	
2777	Fermi Surface and Optical Properties of Potassium	G. Dresselhaus A. R. Wilson C. Y. Young	
2784	Absolute X-ray Form Factor of Nickel	V. E. Henrich P. M. Raccah	
2785	Light Scattering from Drifted Carriers in n-GaAs	A. Mooradian A. G. Foyt	American Physical Society, Dallas, Texas, 23-26 March 1970
2789	Electrical Conductivity in the Hubbard Model	D. Adler* R. A. Bari R. V. Lange*	
2790	Energy Gap Minimum in $ZnTe_{1-x}Se_x$ Alloys	G. W. Iseler	
2791	Energy Gap Minimum in $CdTe_{1-x}Se_x$ Alloys	A. J. Strauss	
2792	Quasi Particle Approach to the Optical Properties of Simple Metals	C. Y. Young	
2795	Electron Spin Waves in Non-magnetic Semiconductors	F. A. Blum	

\* Author not at Lincoln Laboratory.

## MS No.

2796	The 2s( $T_2$ ) Level of Bi Donors in Si Observed by Optical Absorption	W.E. Krag W.H. Kleiner	American Physical Society, Dallas, Texas, 23-26 March 1970
2798	Raman Spectrum of $Ti_2O_3$	P.M. Raccah A. Mooradian	
2801	The Infrared Properties of Arsenic	R.W. Brodersen M.S. Dresselhaus	
2802	Theory of Surface Plasmon Excitation in Electron Tunneling, Low Energy Diffraction and in Photoemission	K.L. Ngai E.N. Economou* M.H. Cohen*	
2803	Optical, Magnetic, and Ultrasonic Studies of Antiferromagnetic EuTe with Magnetic Fields up to 260 kG	C.R. Pidgeon* S. Foner* Y. Shapira* J. Feinleib* T.B. Reed	
2804	Band Theory of Optical Activity	A.S. Pine G. Dresselhaus	
2822	Exciton-Magnon Transitions in $Cr_2O_3$	R.M. Macfarlane* J.W. Allen S. Sugano*	
2850	Comparison of Experimental Charge Densities with Band Calculation Predictions	P.M. Raccah	
2762	Anomalous Properties of the Vanadium Oxides	J.B. Goodenough	Purdue University, Lafayette, Indiana, 7 April 1970
2764	Composition Stability Limits of $(Pb_{1-y}Sn_y)_{1-x}Te_x$ from Lattice Parameters	R.F. Brebrick	Electrochemical Society Los Angeles, California, 15 May 1970
2775	Spin Waves in Plasma-Like Metals	A.R. Wilson	Physics Seminar, University of Alberta, Alberta, Canada, 6 February 1970
2782	Detection and Generation of Far Infrared Radiation in High Purity Epitaxial GaAs	G.E. Stillman C.M. Wolfe J.O. Dimmock	International Symposium on Sub-millimeter Waves, Polytechnic Institute of Brooklyn, New York, 31 March - 2 April 1970
2835	Millimeter and Far Infrared Frequency Mixing in GaAs	H. Fetterman P.E. Tannenwald C.D. Parker	

\* Author not at Lincoln Laboratory.

Reports

MS No.

2802A	Surface Plasmon Excitations and Their Role in LEED	E.N. Economou* K.L. Ngai	Fourth Leed Theory Seminar, National Bureau of Standards, Gaithersburg, Maryland, 1 May 1970
2839	Optical Properties and Electronic Structure of the Magnetic Semiconductors, EuO, EuS, EuSe and EuTe	W.J. Scouler	Seminar, University of Virginia, Charlottesville, Virginia, 20 February 1970
2866	The Thermal Single-Determinant Approximation - A New Generalization of Hartree-Fock Theory	T.A. Kaplan	Physics Seminar, Michigan State University, East Lansing, Michigan, 2 April 1970
2894	Behavior and Misbehavior of d Electrons in Some Vanadium Oxides	J.B. Goodenough	Materials Science Center Seminar, The Pennsylvania State University, University Park, Pennsylvania, 15 May 1970

---

\* Author not at Lincoln Laboratory.

## I. SOLID STATE DEVICE RESEARCH

### A. GaAs FAR INFRARED DETECTORS

Three high purity epitaxial GaAs samples have been evaluated as far infrared detectors under two different background conditions. The material properties of these samples are given in Table I-1. Although the samples fall in the range of purity generally obtainable today by epitaxial techniques, two of them have relatively low compensation ratios compared to those usually observed.

TABLE I-1 MATERIAL PROPERTIES OF DETECTOR SAMPLES					
Sample No.	$N_D$ ( $10^{14} \text{ cm}^{-3}$ )	$N_A$ ( $10^{14} \text{ cm}^{-3}$ )	$n_{300^\circ\text{K}}$ ( $10^{14} \text{ cm}^{-3}$ )	$\mu_{77^\circ\text{K}}$ ( $\text{cm}^2/\text{V-sec}$ )	$E_D$ (meV)
1	1.2	1.0	0.13	155,000	5.4
2	2.0	0.4	1.6	153,000	5.1
3	4.9	1.0	3.7	108,000	4.6

The experimental arrangement shown in Fig. I-1 was used for the optical evaluation of the detectors. The light pipe, which has a total length of about 3 feet, is made of  $\frac{1}{2}$ -inch diameter

gold plated thin wall stainless steel tubing. The cone and spherical integrating cavity for the detector are gold plated electroformed copper. The cone is about 5 inches long and the integrating sphere is  $\frac{1}{2}$  inch in diameter with a  $\frac{1}{8}$ -inch aperture. The integrating chamber was used to minimize differences in sample absorption. A rotating turret positioned between the bottom end of the light pipe and the entrance to the detector cone was used to insert cold filters into the light path or to block off the light pipe for dark resistance measurements. The light pipe, copper cone and filter holder were not evacuated, and the detectors and cold filters were immersed in liquid He. A warm black polyethylene filter was included at the top of the light pipe, and a cold crystal quartz filter wedged to about  $4^\circ$  was included at the entrance to the cone. For the detector calibration measurements a long wavelength pass filter

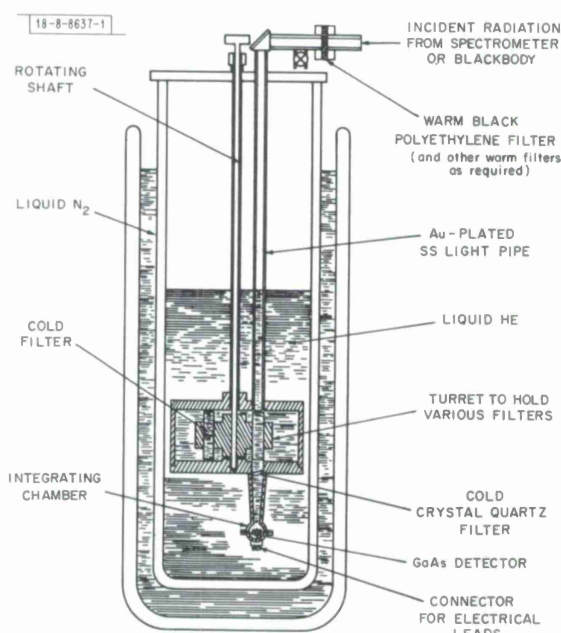


Fig. I-1. Detector mount and filter arrangement for spectral and blackbody calibration measurements.

## Section I

was also used. This filter has a sharp room temperature cutoff at about  $150\mu$ , and its transmittance does not change significantly on cooling from room temperature to  $4.2^{\circ}\text{K}$ . This filter was used for the blackbody calibration measurements either at room temperature (normal background) or at the detector temperature (reduced background).

Electrical contact to the sample was made by alloying pure tin to the epitaxial layer at about  $350^{\circ}\text{C}$  in a reducing atmosphere. The detector circuit used for these measurements consists of a cooled load resistor at the temperature of the He bath ( $R_L = 20$  megohms at  $4.2^{\circ}\text{K}$ , 26 megohms at  $1.93^{\circ}\text{K}$ ) in series with the detector element. One side of the detector was grounded, and a preamplifier was connected across the detector. The signal and noise measurements were made using a PAR model 112 preamplifier and either a Brower model 132 lock-in signal/noise meter or a GR-1900A wave analyser.

The  $4.2^{\circ}\text{K}$  and  $1.93^{\circ}\text{K}$  V-I curves for Sample 2 under normal and reduced background conditions are shown in Fig. I-2. Similar behavior was observed for the other samples. The general features for all four conditions are approximately the same. At low currents and voltages the curves are linear indicating ohmic behavior, but at higher currents the voltage does not increase as rapidly as the current. This decrease in sample resistance results mainly from impact ionization of the neutral shallow donor levels.<sup>1</sup> At a critical field, which depends on the electron mobility and the compensation ratio, the current increases several orders of magnitude while the field remains relatively constant. The breakdown field for Sample 2 was about  $1.5 \text{ V/cm}$  at  $4.2^{\circ}\text{K}$ . In samples which are more heavily compensated, the breakdown field is larger than the sustaining field so that a negative resistance region appears.<sup>2</sup> As shown in Fig. I-2, the background radiation has a negligible effect on the breakdown voltage, but there is a slight increase in the breakdown voltage as the temperature is decreased from  $4.2$  to  $1.93^{\circ}\text{K}$ . This is expected because of the corresponding decrease in mobility.

The resistance of this detector in the ohmic region at  $4.2^{\circ}\text{K}$  is about 600 kilohms for normal background conditions, 1.4 megohms for reduced background, and 8.6 megohms in the dark. At

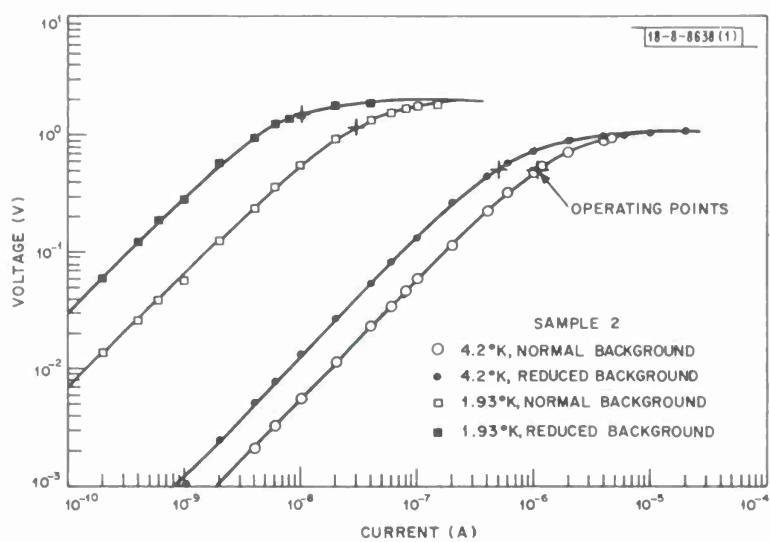


Fig. I-2. V-I characteristics for Sample 2.

1.93°K the corresponding ohmic resistances are 6.5, 28.5, and 330 megohms. For the normal and reduced background conditions at both temperatures, the sample resistance is limited by the generation of free carriers due to the background radiation.

The response of GaAs far infrared detectors at wavelengths longer than  $\sim 214 \mu$  is due primarily to a photothermal excitation process<sup>3</sup> in which electrons are optically excited to the higher bound states of the donor atoms and then thermally transferred into the conduction band. Consequently, although the optical absorption by the impurity centers does not change significantly as the temperature is reduced from 4.2 to 1.93°K, the photo-conductive response of the detectors at long wavelengths decreases relative to that for wavelengths shorter than the photoionization energy. This is because the probability of thermal transfer to the conduction band of an electron in an excited state is much smaller at the lower temperatures. This accounts for the factor of  $\sim 11$  increase in resistance of the detector between 4.2 and 1.93°K, due mainly to the smaller number of free carriers generated by the background radiation. (The mobility for this sample decreases by about a factor of 2 over the same temperature range.) The larger relative increase in resistance at 1.93°K between normal and reduced background conditions compared to that at 4.2°K results because the filter used for reduced background conditions blocks a larger percentage of the effective carrier-producing background radiation at the lower temperature.

The variations of the signal and noise voltages and the signal-to-noise ratio with sample current are shown in Fig. I-3. The signal increases linearly with current for low bias values, but then bends over and decreases for higher currents. The decrease in signal is related to the onset of impact ionization of the neutral shallow donor levels and the resulting decrease in detector resistance. Similar variation is observed for the different temperature and background conditions at currents which produce approximately the same sample voltage. The other samples have nearly the same signal characteristics.

The noise voltage at low currents is nearly constant, and results from a combination of the preamplifier noise with the Johnson noise from the sample and load resistor in parallel. At

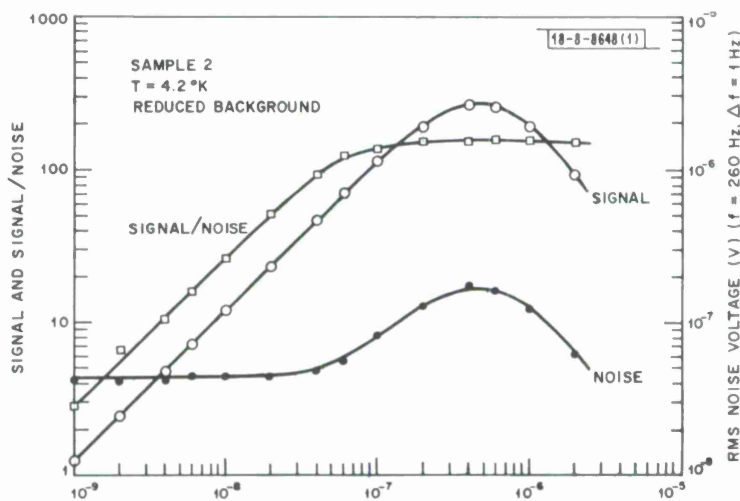


Fig. I-3. Signal, noise, and signal/noise dependence on bias current for Sample 2 at 4.2°K with reduced background conditions.

## Section I

higher currents the noise increases and reaches a maximum at about the same current which produces the maximum signal. The decrease in noise at the higher currents for this sample is about equal to the decrease in signal so that the signal-to-noise ratio is nearly constant over more than a factor of 10 range in bias current. This property is useful because it allows operation without loss in sensitivity at the higher bias currents where the dynamic resistance of the sample is less than at low bias. This is an advantage for those applications where response speed is critical since the dynamic RC time constant for the detector is reduced. If the current is increased to still larger values, the noise increases several orders of magnitude and in this range is apparently associated with the breakdown mechanism.

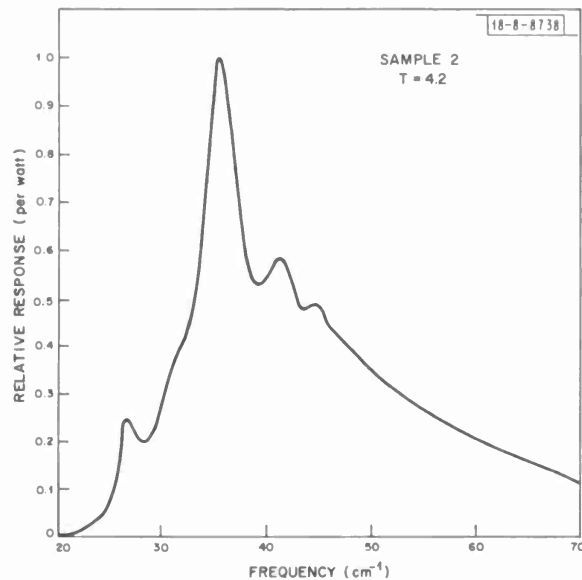


Fig. I-4. Relative spectral response of photoconductivity for Sample 2 at 4.2°K.

The relative spectral response of Sample 2 at 4.2°K is shown in Fig. I-4, and the response of the other samples showed the same general shape. The photoconductivity spectral response measurements were made using a Michelson interferometer. An Eppley Golay cell was used as a reference detector to correct for the beam splitter and source response. The dominant features of the spectral response have been discussed previously.<sup>3</sup>

The peak responsivities of the detectors were determined using a 500°K blackbody source chopped at 260 Hz and the warm or cold filter described above. A simple computer program was used to perform the required integrations of the product of the blackbody emission, the filter transmittance, and the relative spectral response of the detectors. Corrections to the power reaching the detectors were made for the emission from the 300°K chopper blade, which had a measured emissivity of 0.955 in the wavelength region of interest. The blackbody source and optical path were purged with dry nitrogen to reduce the water vapor absorption. The characteristics of the three GaAs detectors at 4.2°K for the two different background conditions are given in Table I-2.

TABLE I-2  
CHARACTERISTICS OF GaAs DETECTORS

Sample No.	Operating Conditions ( $T = 4.2^\circ\text{K}$ )	Peak Responsivity $R_{282\mu}$ (V/W)	$\text{NEP}_{282\mu} (\text{W-Hz}^{-1/2})$ ( $f = 260 \text{ Hz}$ )	Detector Dimensions $L(\text{mm}) \times W(\text{mm}) \times t(\mu)$
1	Normal Background	$4.0 \times 10^4$	$2.0 \times 10^{-12}$	$4.3 \times 4.3 \times 295$
	Reduced Background	$1.4 \times 10^5$	$9.0 \times 10^{-13}$	
2	Normal Background	$4.0 \times 10^4$	$1.3 \times 10^{-12}$	$6.3 \times 5.5 \times 73$
	Reduced Background	$2.4 \times 10^5$	$5.3 \times 10^{-13}$	
3	Normal Background	$3.0 \times 10^4$	$2.8 \times 10^{-12}$	$3.8 \times 3.0 \times 57$
	Reduced Background	$9.9 \times 10^4$	$1.1 \times 10^{-12}$	

G. E. Stillman  
C. M. Wolfe  
J. O. Dimmock

#### B. LONG WAVELENGTH METAL-SEMICONDUCTOR BARRIER LASER ON p-Pb<sub>0.715</sub>Sn<sub>0.285</sub>Te

Laser emission from evaporated metal barriers on p-Pb<sub>0.715</sub>Sn<sub>0.285</sub>Te has been observed at  $\lambda = 28 \mu$ . The barriers were fabricated by evaporating a 10,000-Å thick film on a freshly etched <100> surface. An ohmic back contact was obtained by evaporating gold. The laser emission observed in forward bias showed Fabry-Perot mode structure extending from  $\lambda = 27.5 \mu$  to  $28.9 \mu$  indicating an energy gap of about  $E_g = 0.043 \text{ eV}$ . Electron microprobe measurements of the composition were performed on the laser after etching away the evaporated Pb barrier. The composition Pb<sub>0.715</sub>Sn<sub>0.285</sub>Te determined in this manner and the energy gap of  $E_g = 0.043 \text{ eV}$  are in satisfactory agreement with the linearly extrapolated results for  $E_g$  vs  $x$  of Pb<sub>1-x</sub>Sn<sub>x</sub>Te alloys of lower mole fraction SnTe. These devices were fabricated from large Bridgman-grown crystals. The material growth and annealing results are discussed in the following section.

K. W. Nill  
A. R. Calawa  
T. C. Harman

#### C. PREPARATION OF MATERIAL FOR METAL-SEMICONDUCTOR BARRIER LASERS

Experimental results<sup>4</sup> for some isothermally annealed Bridgman-grown crystals of Pb<sub>1-x</sub>Sn<sub>x</sub>Te for  $x = 0.13$  to  $x = 0.27$  were reported some time ago. These annealing experiments have now been extended to  $x \approx 0.3$  for Bridgman-grown crystals equilibrated with a metal-saturated alloy (Pb<sub>0.7</sub>Sn<sub>0.3</sub>)<sub>0.51</sub>Te<sub>0.49</sub>. The carrier concentration results are displayed

## Section I

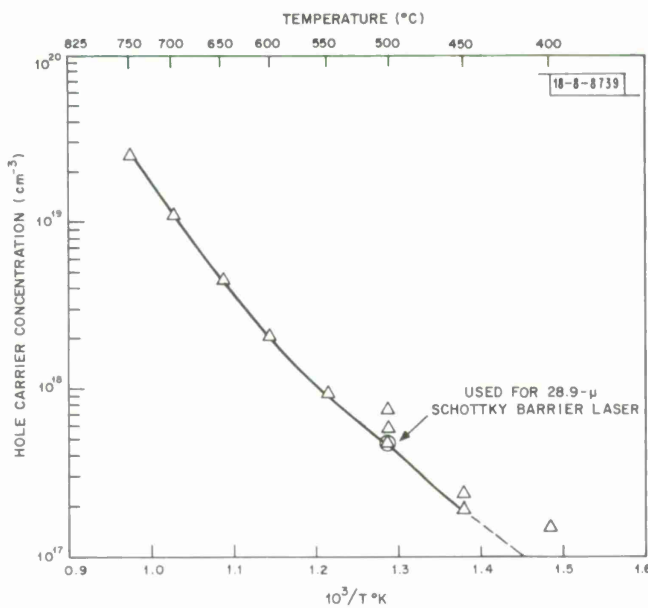


Fig. I-5. Hole carrier concentration determined at 77°K as a function of isothermal annealing temperature for metal-saturated  $\text{Pb}_{1-x}\text{Sn}_x\text{Te}$  for  $x \approx 0.3$ .

graphically in Fig. I-5. It is seen that the hole carrier concentration varies from  $2.5 \times 10^{19}/\text{cm}^3$  for equilibrium at 750°C to  $1.5 \times 10^{17}/\text{cm}^3$  at 400°C. Sample thicknesses were 0.025 cm. For the specimens annealed at lower temperatures, several annealing temperatures were used and total annealing times of approximately 90 days were employed for each crystal. The material used for the metal-semiconductor long wavelength laser described in the previous section is indicated in Fig. I-5.

T. C. Harman  
A. E. Paladino

### D. TYPE CONVERSION AND n-p JUNCTION FORMATION IN $\text{Hg}_{1-x}\text{Cd}_x\text{Te}$ PRODUCED BY PHOTON BOMBARDMENT

We have found that proton bombardment can be used to create n-type layers in p-type  $\text{Hg}_{1-x}\text{Cd}_x\text{Te}$ , and have used this technique to fabricate n-p junction photovoltaic detectors. We feel that this technique is exciting, as it is difficult to make junction photovoltaic detectors in this material by diffusion techniques.

Initial experiments were done using a crystal of  $\text{Hg}_{0.5}\text{Cd}_{0.5}\text{Te}$ , which was p-type ( $p \sim 2 \times 10^{16}/\text{cm}^3$  at room temperature). Using photoresist as a bombardment mask, 15-mil square areas in the sample were bombarded with 100 keV protons. Following bombardment, DC thermal probe tests and conductance measurements were made on both the bombarded and unbombarded areas. These measurements indicated that the bombarded areas had been converted to n-type, whereas the unbombarded areas remained p-type. Ohmic behavior was observed between contacts on a bombarded 15-mil square, while diode characteristics were observed between the bombarded squares and the substrate. At room temperature, zero-bias diode resistances as high as 90 kilohms were observed.

The photovoltaic response of these diodes has a peak at  $1.8\mu$ , with a quantum efficiency at the peak of  $\sim 15$  percent. The room temperature detectivity at the peak of  $2 \times 10^{10} \text{ cm} \sqrt{\text{Hz}}/\text{W}$  is limited by the thermal noise of the detector.

A. G. Foyt  
T. C. Harman  
J. P. Donnelly

#### E. A VIDICON WITH A GaAs SCHOTTKY BARRIER DIODE ARRAY TARGET

A vidicon type television camera tube has been constructed with an image sensing target consisting of an array of reverse biased Schottky barrier photodiodes on GaAs. The diodes are accessed by a low energy scanning electron beam as in a conventional vidicon.<sup>5</sup>

The n-type GaAs substrate with net electron concentration of  $1 \times 10^{14} \text{ cm}^{-3}$  was chemically polished to a thickness of approximately  $7\mu$  and the Schottky barrier diodes were fabricated by electroplating gold or platinum through photolithographically defined holes in a pyrolytic silicon oxy-nitride layer. The diodes are reverse biased sufficiently to totally deplete thin GaAs, and hence lateral diffusion of the photogenerated carriers is not a factor in determining the resolution of the tube. The spatial resolution is set by the  $17.5\mu$  center-to-center spacing of the diodes and the diameter of the scanning electron beam. The plated Schottky barriers are designed to shield the passivating silicon oxy-nitride layer and in this way the need for a "resistive sea" is eliminated. Typical dark currents for the array are less than  $50\text{nA}$ .

The GaAs Schottky barrier diode array vidicon exhibits freedom from image persistance due to photoconductive lag, is not damaged by exposure to intense light and can be vacuum baked at temperatures considerably in excess of  $200^\circ\text{C}$ .<sup>\*</sup> It is expected that the target will have a broad spectral response and an effective quantum efficiency greater than 50 percent. In these respects it should be superior to a conventional photoconductive vidicon.<sup>5,6</sup> Measurement of these parameters is now in progress. Although the device is still in the research stage, the simplicity of fabrication, lack of need for a resistive sea and possible benefits in long term performance and stability make the GaAs Schottky barrier diode vidicon an attractive alternative to the silicon array tube.<sup>7</sup>

C. E. Hurwitz  
W. T. Lindley  
C. M. Wolfe

#### F. A NEW TECHNIQUE FOR THE FABRICATION OF GaAs SCHOTTKY BARRIER FIELD EFFECT TRANSISTORS

A technique has been developed for the fabrication of GaAs Schottky barrier field effect transistors in which the source and drain ohmic contacts are on one side of a thin GaAs layer and the gate is on the other. This technique is particularly useful for the fabrication of high frequency devices since it allows a reduction of the source-drain spacing to values which are difficult or impossible to achieve using a conventional single-sided technique in which the gate must be placed on the same surface between the source and drain. Since this spacing is a critical parameter in determining the high frequency performance of the transistor, substantial improvement should result.

---

\* The platinum on GaAs Schottky barriers will withstand  $400^\circ\text{C}$  without degradation. Presently, the baking temperature is limited to about  $200^\circ\text{C}$  by the epoxy used to attach the GaAs to the glass or sapphire substrate and the substrate to the tube envelope.

## Section I

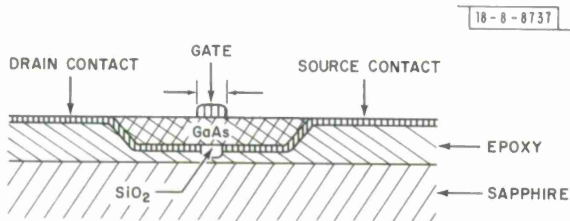


Fig. I-6. Cross section of completed FET.

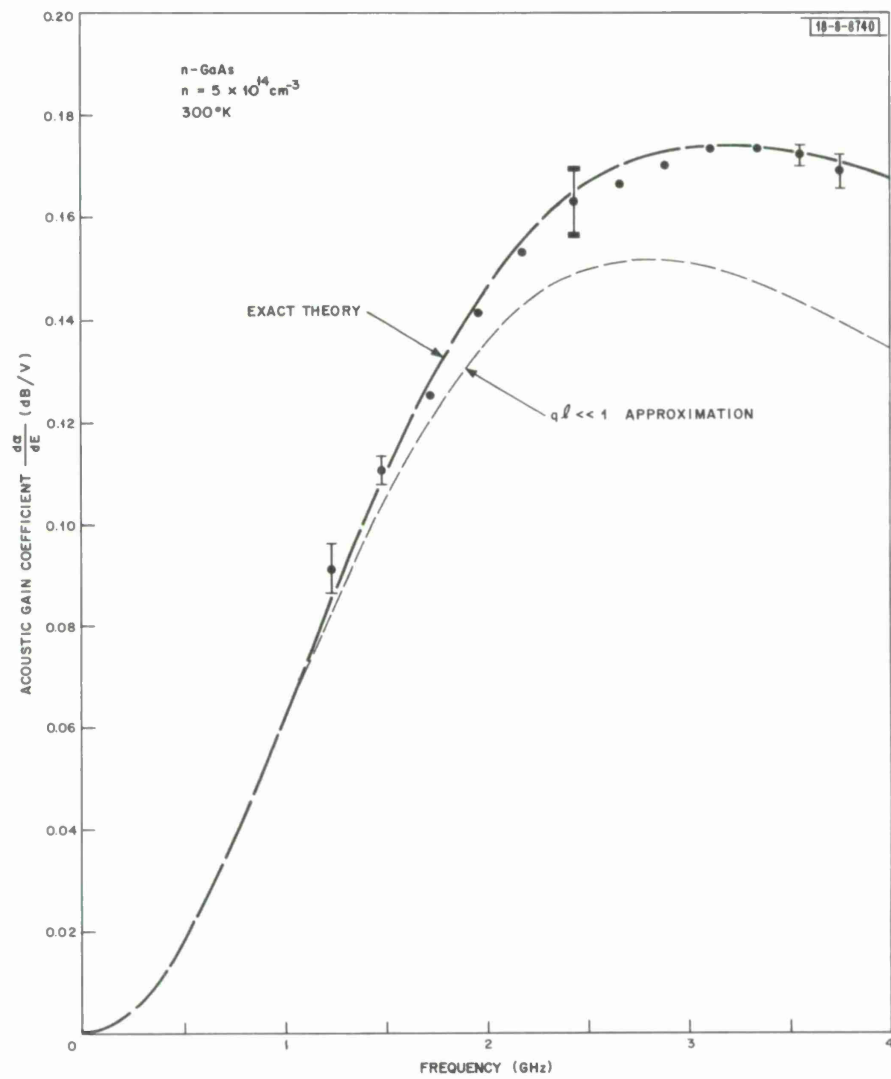


Fig. I-7. Experimental and theoretical frequency dependence of acoustic gain coefficient. Absolute error is indicated by heavy error bars at 2.43 GHz; other error bars show relative error.

The fabrication of the transistors begins with a slice of bulk GaAs, one surface of which is patterned and etched to form an array of shallow mesas. (Each mesa will eventually form an individual island of GaAs which will become a single FET.) This surface is covered with pyrolytic silicon dioxide, and openings are made for the microalloyed gold-tin source and drain ohmic contacts, with the source-drain gap on top of the mesa. Additional gold is electroplated over the ohmic contacts and extended out over the etched region to provide contacts to the source and drain. The wafer is mounted with epoxy onto a sapphire substrate with the source-drain side down and then lapped and chemically polished until only the individual GaAs islands, the source and drain contact pads, and the surrounding silicon dioxide remain. Finally, the gate pattern is defined and gold is electroplated onto the GaAs island to form the gate. A cross sectional diagram of the completed device is shown in Fig. I-6.

The initial results have been obtained on transistors fabricated using  $2 \times 10^6 \text{ cm}^{-3}$  n-type GaAs. The final GaAs layer was  $0.5 \mu$  thick; the source drain spacing,  $5 \mu$ ; the gate length,  $5 \mu$ ; and the channel width  $150 \mu$ . These transistors have shown normal FET characteristics, with a transconductance of 5 to 10 millimhos.

Several advantages accrue from this new fabrication technique. First, bulk GaAs can be used, thus obviating the need for difficult-to-make thin epitaxial layers. Second, the ability to carry out fabrication steps on both sides of the thin semiconductor layer greatly reduces problems in geometry control inherent in presently used techniques for FET fabrication. Finally, the ability to reduce source to drain spacing and gate capacitance should result in significant improvement of the microwave performance of GaAs Schottky barrier field effect transistors.

W. T. Lindley  
C. E. Hurwitz  
A. G. Foyt

#### G. FREQUENCY DEPENDENCE OF ACOUSTOELECTRIC AMPLIFICATION IN n-GaAs

Acoustoelectric amplification coefficients have been measured over a range of frequencies near the frequency of maximum gain in oxygen-compensated n-type GaAs ( $n \approx 5 \times 10^{14} \text{ cm}^{-3}$ ) at room temperature using the Brillouin scattering technique described previously.<sup>8</sup> A meaningful and accurate gain coefficient can be obtained from this material although it is relatively inhomogeneous (the most uniform samples exhibited 50 percent variations in resistivity over distances of 15 mm) by measuring the change in gain per unit length with respect to a change in applied field  $d\alpha/dE$ . This quantity is independent of the electrical properties of the material for low fields at the frequency of maximum gain in the  $q\ell \ll 1$  limit,<sup>9</sup> where  $q$  is the acoustic wave-vector and  $\ell$  the electronic mean free path.

The measured and calculated frequency dependence of  $d\alpha/dE$  for [110] shear waves is shown in Fig. I-7. Relatively good agreement with the exact theory<sup>10</sup> is obtained over the accessible frequency range from 1.23 to 3.75 GHz. Both the frequency of maximum gain and the magnitude of the gain coefficient were found to be about 15 percent larger than given by the  $q\ell \ll 1$  approximation,<sup>9</sup> which is expected since at 4 GHz  $q\ell = 0.6$ . The experimental accuracy  $\pm 5$  percent is somewhat better than the accuracy of the calculation  $\pm 10$  percent, which is limited primarily by the uncertainty in the best reported value of the piezoelectric constant.<sup>11</sup>

D. L. Spears

REFERENCES

1. D.J. Oliver, Phys. Rev. 127, 1045 (1962); R.A. Reynolds, Solid State Electron. 11, 385 (1968).
2. A.L. McWhorter and R.H. Rediker, Proc. IRE 47, 1207 (1959).
3. G.E. Stillman, C.M. Wolfe and J.O. Dimmock, Solid State Commun. 7, 921 (1969).
4. A.R. Calawa, T.C. Harman, M. Finn and P. Youtz, Trans. AIME 242, 374 (1968), DDC AD-678986.
5. P.K. Weimer, J.V. Forgue and R.R. Goodrich, RCA Rev. 12, 306 (1951).
6. E.F. de Haan, A. van der Drift and P.P.M. Schlampers, Philips Tech. Rev. 25, 133 (1963).
7. M.H. Crowell and E.F. Labuda, Bell Systems Tech. J. 48, 1481 (1969); T.R. Kohler, J. Kostelet, E. Stupp and E. Rasmanis, Proc. of the Technical Program of the Electro-Optical Systems Conference, September, 1969, edited by K.A. Kopetzky (Industrial and Scientific Conference Management, Inc., Chicago, 1970), p. 36; F.L. Skaggs, J.B. Horak, C.P. Stephens and D.L. Gilblom, ibid., p. 729.
8. Solid State Research Report, Lincoln Laboratory, M.I.T. (1970:1), p. 5.
9. D.L. White, J. Appl. Phys. 33, 2547 (1962).
10. C. Jacoboni and E.W. Prohofsky, J. Appl. Phys. 40, 454 (1969).
11. K.G. Hambleton, Phys. Lett. 16, 241 (1965).

## II. MATERIALS RESEARCH

### A. USE OF HEAT PIPE IN CRYSTAL PULLING

In the Czochralski method of crystal growth from the melt, a seed crystal attached to a metal or ceramic rod grows longer as it is gradually pulled from the melt by raising the seed rod. In most cases the rod is simultaneously rotated in order to give the crystal rotational symmetry and to remove impurities from the interface region by stirring the melt. It is advantageous and sometimes necessary to cool the rod, in order to increase the temperature gradient at the interface. This stabilizes the position of the interface and reduces the likelihood of constitutional supercooling. Cooling is generally accomplished by circulating water through the rod, but this requires a controlled flow of water and the use of rotating seals which tend to leak.

To eliminate the disadvantages of water cooling, we have constructed a seed rod for our tri-arc crystal puller<sup>1</sup> which is cooled by means of a heat pipe,<sup>2,3</sup> a device with extremely high effective thermal conductivity. The heat pipe is a hollow evacuated tube containing a volatile liquid and lined with a material which can act as a wick. When one end of the pipe is heated, the liquid partially vaporizes, the vapor is transported at sonic velocity to the cold end where it condenses, and the condensed liquid returns to the hot end (independently of gravity) via the wick. Because the heat of vaporization is absorbed at the hot end and liberated at the cold end, a large quantity of heat can be transferred with a temperature difference between the ends which is typically only a fraction of a degree.

The new seed rod is shown schematically in Fig. II-1, in position for crystal growth. The copper heat pipe, a commercial unit 1.25 cm in diameter and 30 cm long, has a maximum operating temperature of 240°C. The heat liberated at the cold end outside the furnace is transferred to the room by means of a finned heat exchanger 4 cm in diameter and 5 cm long. Because of the relatively high operating temperature, a teflon seal is used at the furnace gland, as shown in Fig. II-1.

The new seed rod has been used to grow a number of single crystals of VO and polycrystalline boules of Ti and Ni. Seed crystals were not used. Instead, a molybdenum stud screwed into the lower end of the heat pipe (Fig. II-1) was dipped into the melt to initiate growth. During one run with Ti, the temperature at the upper end of the heat pipe was monitored by means of a thermocouple. The

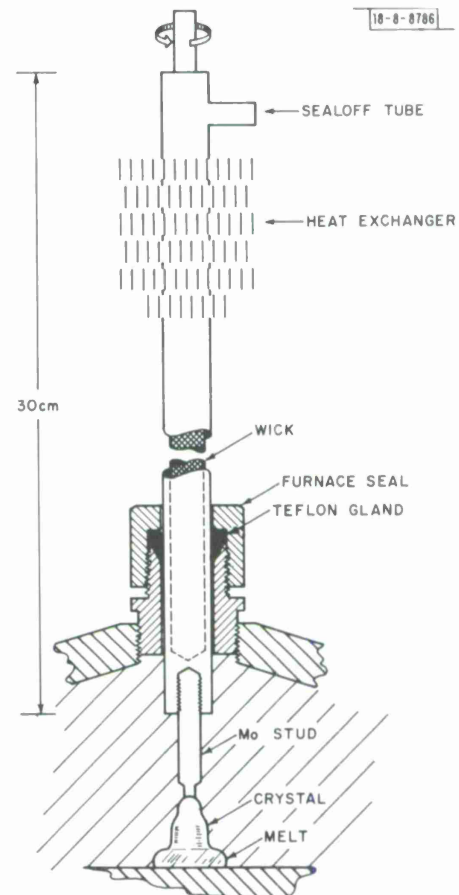


Fig. II-1. Seed rod, cooled by means of heat pipe, for tri-arc crystal puller.

## Section II

temperature was 210° to 235°C when the stud was in direct contact with the superheated melt (~1700°C) and dropped continuously during growth, reaching 120°C when the Ti boule was about 25 mm long and 8 mm in diameter.

In a calibration experiment the heat transfer properties of the heat pipe were measured in still and moving air. The lower 5 cm of the pipe was inserted into a soldering iron in place of the soldering tip, and asbestos insulation was wrapped around the iron. The temperature of the pipe just below the heat exchanger was measured with a chromel-alumel thermocouple wrapped around the pipe and covered with asbestos. Figure II-2 shows this temperature as a function of

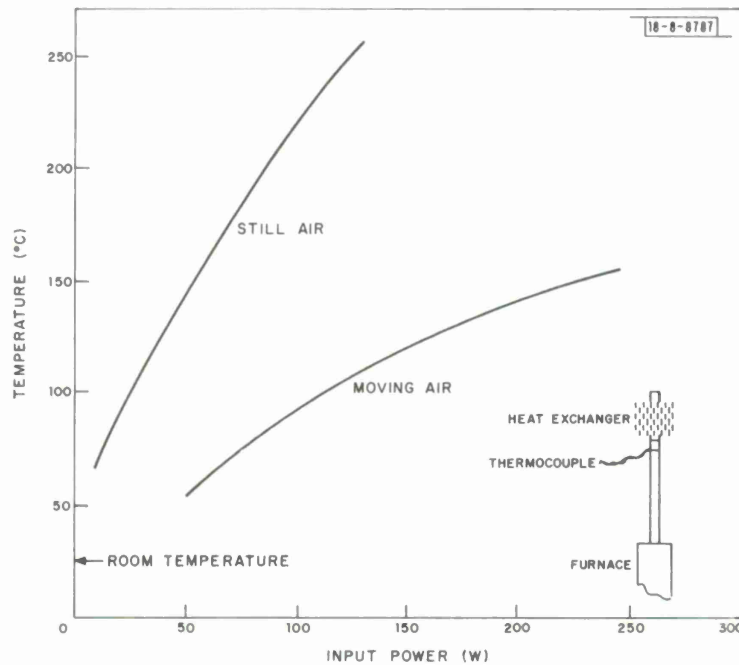


Fig. II-2. Temperature of heat pipe as a function of input power, for heat exchanger in still and moving air.

input power to the soldering iron for still air and for a stream of air produced by a 14-W muffin fan about 10 cm from the pipe. In still air, the power dissipation is 120 W at the maximum operating temperature of 240°C. For moving air, the highest available input power (250 W) gave a temperature of only about 150°C, and extrapolation of the experimental curve indicates that at 240°C the power dissipated would be about 600 W, probably more than required for any normal crystal growth experiment. At a power input of 250 W, the temperature difference along 10 cm of the heat pipe was only 9°C. Under the same conditions, the temperature difference along a copper cylinder of the same diameter would be 480°C.

T. B. Reed

### B. VAPOR GROWTH OF CdO SINGLE CRYSTALS

All samples of CdO, the only II-VI compound with rocksalt structure, are n-type. Generally they have carrier concentrations in the range  $10^{19} - 10^{20} \text{ cm}^{-3}$ , which are due to doubly ionized

native donor defects associated with the presence of Cd in excess of the stoichiometric composition.<sup>4</sup> The carrier concentration can be reduced to  $\sim 10^{18} \text{ cm}^{-3}$  by annealing at elevated temperatures in an oxygen atmosphere, and values as low as  $\sim 10^{14} \text{ cm}^{-3}$  have been reported for sputtered films doped with copper.<sup>5</sup>

Experimental investigations of CdO have been hindered by the high CdO carrier concentration and also because its high melting point (probably above 1600°C) and reactivity with other oxides, especially silica, make single crystal growth difficult. Consequently most studies of optical and electrical properties have been made either on sintered compacts or on sputtered thin films. Crystals approaching 1 cm in their largest dimension have been grown from the vapor phase by sublimation of CdO powder either in an open system utilizing an inert carrier gas<sup>6</sup> or in a closed system.<sup>7</sup> However, these methods require temperatures exceeding 1150°C for appreciable growth rates, and at these temperatures the reaction with container materials is severe. Crystals have also been grown from CdO powder by iodine vapor transport at only about 900 to 950°C,<sup>4</sup> but this method uses a sealed ampoule made of fused silica, which reacts strongly with CdO even at this temperature. In addition, iodine would be expected to act as a donor impurity if it were incorporated into the CdO lattice.

We have developed an open tube method for the vapor growth of CdO crystals from the elements. This method yields sizeable crystals of rather high purity at temperatures well below those required for sublimation of CdO. The apparatus is shown schematically in Fig. II-3. Its

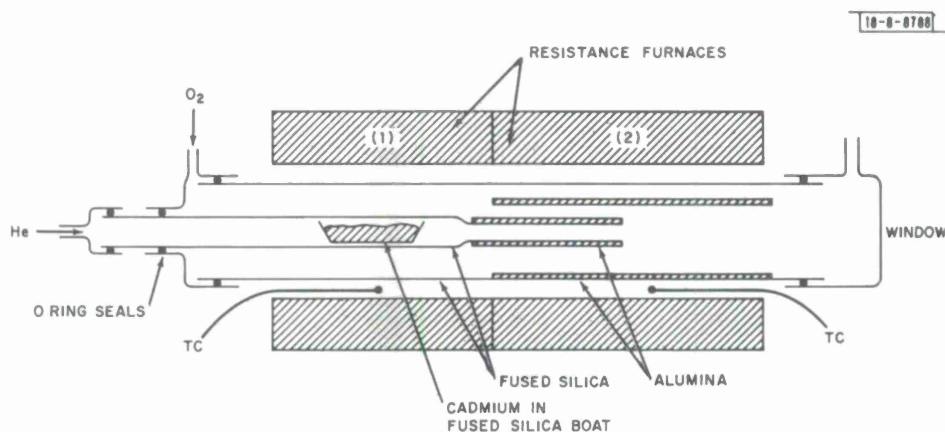


Fig. II-3. Open tube apparatus for growth of CdO single crystals from vapor phase.

principal components are two concentric tubes heated by two adjacent resistance furnaces, the second hotter than the first. The inner tube consists of a fused silica section inside the first furnace and a section made of high purity  $\text{Al}_2\text{O}_3$  which ends at the center of the second furnace. The outer tube is made of fused silica, and the portion inside the second furnace contains a cylindrical liner made of high purity  $\text{Al}_2\text{O}_3$ . Only the two alumina parts are exposed to CdO at high temperature. Attempts to use alundum, magnesia, thoria, and boron nitride instead of alumina were unsuccessful, since all these materials reacted strongly with CdO at high temperature.

During a growth run a stream of helium gas (80 to 100 ml/min), purified by being passed over titanium metal at 800°C, enters the inner tube. It is then saturated with cadmium vapor

## Section II

by being passed over a fused silica boat initially containing about 100 g of molten cadmium (nominal purity 99.9999 percent) heated by the first furnace to 460°C, where the vapor pressure of cadmium is 5 Torrs. A stream of pure oxygen (20 to 30 ml/min) enters the outer tube and mixes with the cadmium-helium stream inside the second furnace, whose center 5 inches are maintained at 1050°C with a temperature gradient of less than 5°C/in. The CdO crystals grow downstream from the end of the inner tube. At the beginning of each run the oxygen flow rate is adjusted while the growth process is being observed through a window at the end of the outer tube. Too high a rate causes CdO to deposit inside the inner tube, which would eventually be blocked, and too low a rate causes deposition of elemental cadmium at the downstream end of the liner. After the optimum flow rate is established, the run is continued until the cadmium boat is empty, which requires about 24 hours.

Most of the CdO crystals, which are black and quite highly reflective, are in the form of thick square plates adhering to the alumina liner by one of their large faces. The largest crystals are formed within 2 to 3 inches from the end of the inner tube. Several with dimensions between  $5 \times 5 \times 2$  mm and  $8 \times 8 \times 3$  mm are obtained from most runs. A number of intergrown and twinned crystals with multiple facets frequently grow from the tip of the inner tube, and smaller crystals are obtained in the cooler region near the end of the furnace.

X-ray diffraction analysis confirms that the crystals have the rocksalt structure. Typical impurity concentrations determined by mass spectrographic analysis are: Al, about 60 ppma; Na and Cl, each about 10 ppma; other impurities expected to be electrically active, less than 1 ppma (the limit of detection). The concentration of Al is not uniform. Presumably it is highest where the crystals adhered to the alumina liner.

A few measurements of the electrical resistivity ( $\rho$ ) and Hall coefficient ( $R_H$ ) have been made at room temperature on as-grown and annealed CdO crystals about 1 mm thick. The carrier concentrations ( $n = -1/R_H e$ ) are  $1.4 \times 10^{20}$  and  $1.5 \times 10^{20} \text{ cm}^{-3}$  for two as-grown samples,  $1.1 \times 10^{20} \text{ cm}^{-3}$  for a sample annealed 90 hours at 1000°C and an oxygen pressure of about 3.8 atm, and  $2.7 \times 10^{19}$  and  $1.8 \times 10^{19} \text{ cm}^{-3}$  for two samples from different growth runs annealed in air at 740°C for 24 and 28 days, respectively. The latter two values are significantly higher than the concentration of  $1.3 \times 10^{19} \text{ cm}^{-3}$  for the same temperature and oxygen pressure interpolated from the recent rather extensive data of Koffyberg<sup>4</sup> for the annealing of CdO crystals grown by iodine vapor transport. The Hall mobilities ( $\mu = R_H/\rho$ ) for the same five samples are 61, 65, 79,  $1.4 \times 10^2$ , and  $1.8 \times 10^2 \text{ cm}^2/\text{V-sec}$ , respectively. The latter two values are in good agreement with those of Koffyberg<sup>4</sup>, whose data do not extend above a carrier concentration of  $6 \times 10^{19} \text{ cm}^{-3}$ .

F. T. J. Smith

### C. STANDARD FREE ENERGY CHARTS FOR BINARY SELENIDES AND TELLURIDES

The standard free energy of formation,  $\Delta G_f^\circ$ , is one of the most useful thermodynamic quantities for chemical calculations. In order to provide a convenient source of  $\Delta G_f^\circ$  data, we are preparing an atlas of charts in which  $\Delta G_f^\circ$  is plotted over a wide range of temperatures for a large number of binary compounds. For the hydrides, nitrides, oxides, halides, and sulfides, the charts have been compiled from those scattered through the literature. For the selenides and tellurides, however, no charts of this type have been published, and it has been necessary

to construct them from the numerical data for the individual compounds. In order to make these new charts available before the complete atlas is published, they are given here.

For a compound  $MX_q$  (where X is Se or Te, M is any other element, and q is the ratio of small whole numbers in the stoichiometric formula), at a given temperature  $\Delta G_f^\circ$  is by definition the free energy change accompanying the reaction



when each reactant is in its standard state, i.e., its state at that temperature and a pressure of 1 atmosphere. (The reaction is written in terms of  $X_2$  rather than X because Se and Te are diatomic gases over most of the temperature range covered by the charts.) Within any temperature interval in which the reactants do not change state,  $\Delta G_f^\circ$  varies linearly with temperature according to the equation  $\Delta G_f^\circ = \Delta H_f - T\Delta S_f$ , where  $\Delta H_f$  and  $\Delta S_f$  are respectively the enthalpy and entropy of formation. (Although the latter quantities are weakly temperature dependent, their average values within each temperature interval represent  $\Delta G_f^\circ$  with a precision of better than 1 kcal/mole, while the probable accuracy of the experimental  $\Delta G_f^\circ$  data is about 3 kcal/mole.) Therefore each plot of  $\Delta G_f^\circ$  vs T consists of a series of straight-line segments, intersecting at the melting and boiling points of the various reactants, whose slopes differ by the entropies of fusion or vaporization.

The  $\Delta G_f^\circ$  charts which have been constructed for the selenides and tellurides are given in Figs. II-4 and II-5, respectively, and the values of  $\Delta H_f$  and  $\Delta S_f$  are listed in Tables II-1 and II-2, respectively. The standard states for each reactant, whether solid, liquid, or gas, are indicated.

The quantity  $\Delta G_f$  is related to the equilibrium constant for Eq. (II-1) and to the partial pressures  $p_i$  of the gaseous species by

$$\Delta G_f = -RT \ln K \equiv -RT \ln \frac{(p_{MX_q})^{2/q}}{p_{X_2} (p_M)^{2/q}}$$

By convention the pressure is taken to be 1 (unit activity) for any reactant not in the gaseous state. The quantity  $\Delta G_f$  is related to the electromotive force E of an electrochemical cell corresponding to Eq. (II-1) by  $\Delta G_f = -23.06 nE$ , where n is the number of electrons involved in the reaction, four in this case.

The  $\Delta G_f$  equations for which  $\Delta H_f$  and  $\Delta S_f$  values are listed in Tables II-1 and II-2 are applicable at pressures other than 1 atmosphere. In each case the equation to be used is the one for which the standard states are the same as those of the reactants at the experimental pressure and temperature, even if this temperature is outside the range specified for the equation in the table.

T. B. Reed

#### D. DEVIATIONS FROM STOICHIOMETRY IN EuO

A limited number of earlier observations on EuO crystals grown by directional freezing from Eu-O solutions of various compositions indicated that solid EuO could exist over a small but significant range of compositions.<sup>8</sup> As the oxygen content of the growth solution was increased,

Section II

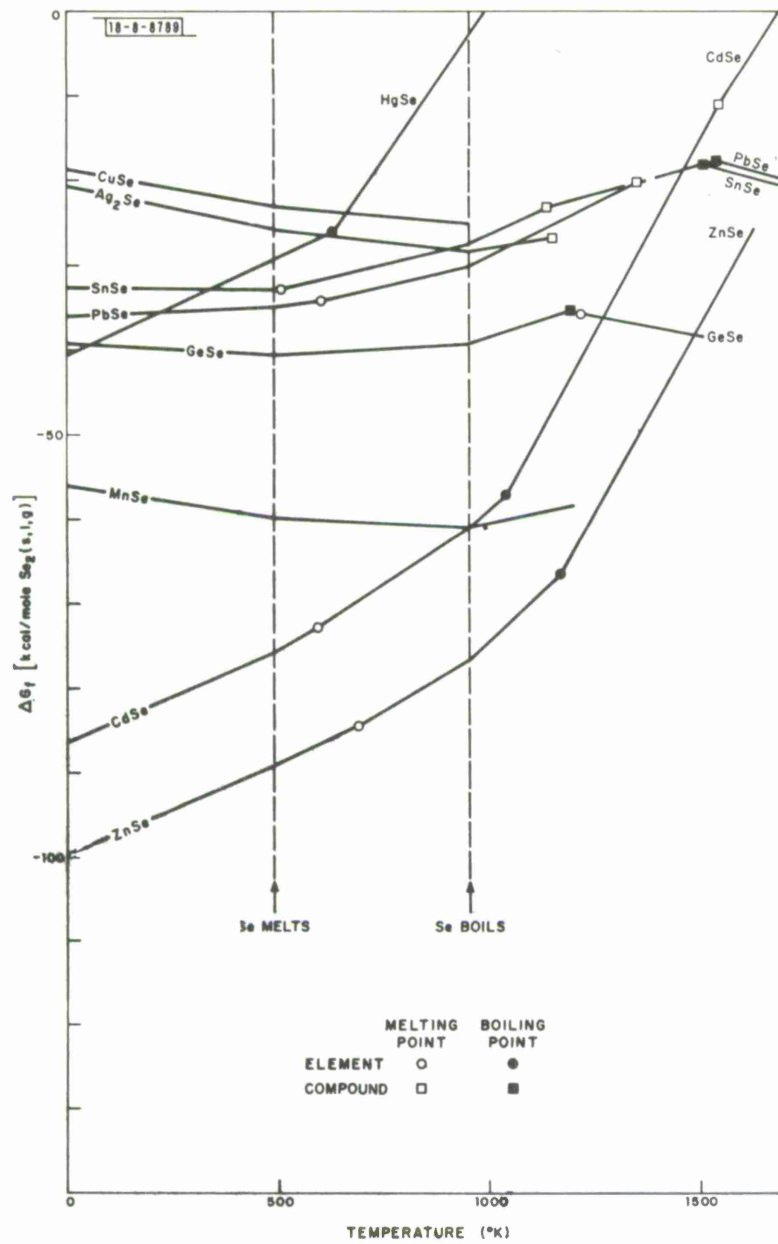


Fig. II-4. Chart of standard free energy of formation ( $\Delta G_f^\circ$ ) vs temperature for binary selenides.

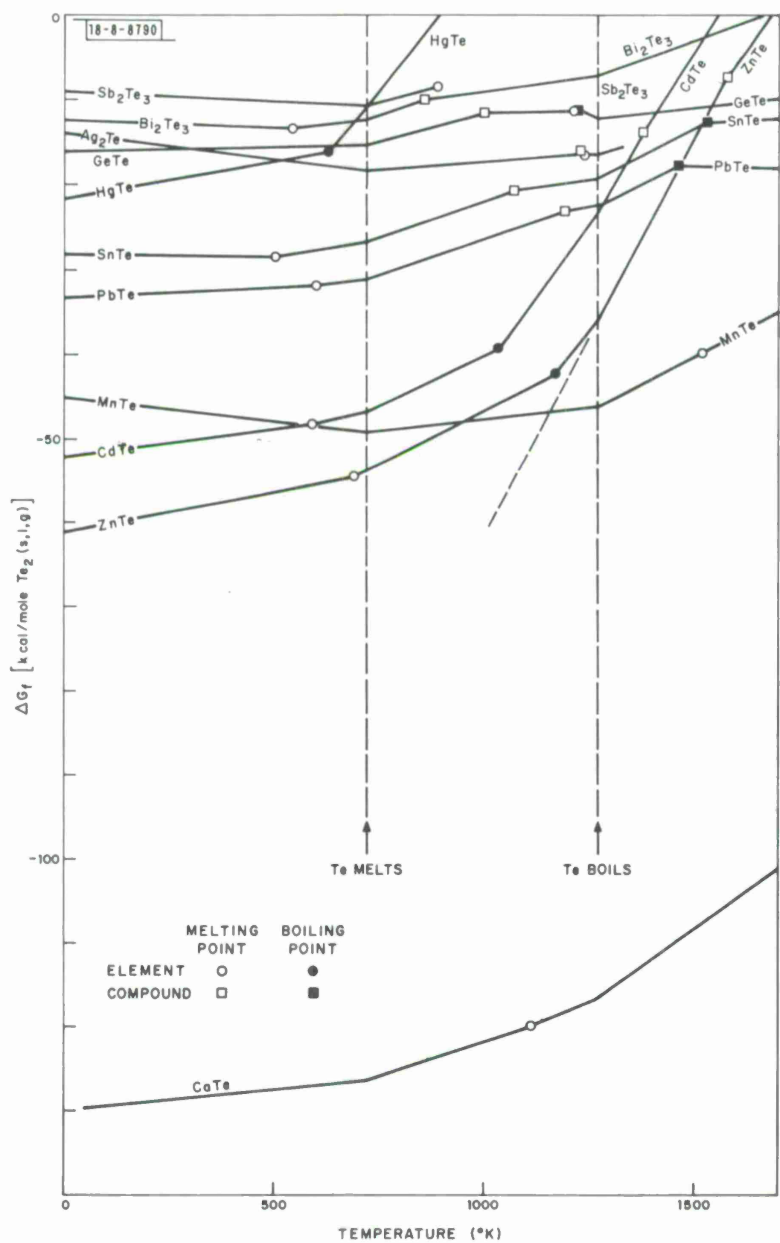


Fig. II-5. Chart of standard free energy of formation ( $\Delta G_f^\circ$ ) vs temperature for binary tellurides.

## Section II

TABLE II-1  
FREE ENERGY OF FORMATION OF SELENIDES

Compound	Temperature Range (°K)	$-\Delta H$ (kcal/mole)	$-\Delta S$ (cal/°mole)	Phase Change at Lower Temperature*
ZnSe	0- 490	99.6	20.2	—
	490- 693	102.2	25.5	SeM
	693- 952	105.7	30.6	ZnM
	952-1184	118.3	43.8	SeB
	1184-1803	172.9	90.2	ZnB
	1803-2000	151.3	78.2	ZnSeM
CdSe	0- 490	86.3	22.0	—
	490- 594	88.9	27.3	SeM
	594- 952	92.0	32.4	C M
	952-1038	104.6	45.6	SeB
	1038-1541	152.4	91.6	CdB
	1541-1680	133.9	79.6	CdSeM
HgSe	0- 490	40.4	21.5	—
	490- 630	43.0	26.8	SeM
	630- 952	71.2	71.6	HgB
	952-1072	83.8	84.8	SeB
	1072-1200	70.9	72.8	HgSeM
GeSe	0- 490	39.4	-2.6	—
	490- 952	42.0	2.7	SeM
	952-1195	54.6	15.9	SeB
	1195-1213	9.0	-22.2	GeSeS
	1213-1500	26.6	-7.7	GeM
SnSe	0- 490	32.8	-0.2	—
	490- 505	35.4	5.1	SeM
	505- 952	38.8	11.8	SnM
	952-1133	51.4	25.0	SeB
	1133-1506	37.8	13.0	SnSeM
	1506-1700	0.2	-12.0	SnSeB
PbSe	0- 490	36.0	2.2	—
	490- 600	38.6	7.5	SeM
	600- 952	40.9	11.3	PbM
	952-1349	53.5	24.5	SeB
	1349-1531	37.3	12.5	PbSeM
	1531-1700	-0.5	-12.2	PbSeB
$\text{Ag}_2\text{Se}$	0- 490	20.6	-10.7	—
	490- 952	23.2	-5.4	SeM
	952-1153	35.8	7.8	SeB
	1153-1200	21.9	-4.2	AgSeM
CuSe	0- 490	18.9	-9.2	—
	490- 952	21.5	-3.9	SeM
MnSe	0- 490	-56.0	-7.9	—
	490- 952	-58.6	-2.6	SeM
	952-1200	-71.2	10.6	SeB

\* M — melts  
B — boils  
S — sublimes

TABLE II-2  
FREE ENERGY OF FORMATION OF TELLURIDES

Compound	Temperature Range (°K)	$-\Delta H$ (kcal/mole)	$-\Delta S$ (cal/°Kmole)	Phase Change at Lower Temperature*
ZnTe	0- 693	60.9	9.2	—
	693- 723	64.4	14.3	ZnM
	723-1184	72.8	25.9	TeM
	1184-1271	127.4	72.3	ZnB
	1271-1576	152.4	92.0	TeB
CdTe	1576-1700	133.5	80.0	ZnTeM
	0- 594	52.4	6.9	—
	594- 723	55.5	12.0	CdM
	723-1038	63.9	23.6	TeM
	1038-1271	111.7	69.6	CdB
	1271-1378	136.7	89.3	TeB
HgTe	1378-1700	120.2	77.3	CdTeM
	0- 630	21.7	9.3	—
	630- 723	49.9	54.1	HgB
	723- 943	58.3	65.7	TeM
GeTe	943-1271	47.0	53.7	HgTeM
	0- 723	16.0	1.2	—
	723- 998	24.4	12.8	TeM
	998-1213	12.4	0.8	GeTeM
	1213-1215	30.0	15.3	GeM
	1215-1271	-6.0	-14.3	GeTeB
SnTe	1271-1700	19.0	5.4	TeB
	0- 505	28.4	0	—
	505- 723	31.8	6.7	SnM
	723-1063	40.2	18.3	TeM
	1063-1271	27.4	6.3	SnTeM
	1271-1530	52.4	26.0	TeB
PbTe	1530-1700	12.5	-0.1	SnTeB
	0- 600	33.2	2.2	—
	600- 723	35.5	6.0	PbM
	723-1190	43.9	17.6	TeM
	1190-1271	29.6	5.6	PbTeM
	1271-1464	54.6	25.3	TeB
$\text{Ag}_2\text{Te}$	1464-1700	15.4	-1.5	PbTeB
	0- 723	14.0	-6.4	—
	723-1230	22.3	5.2	TeM
	1230-1233	0.2	-12.8	$\text{Ag}_2\text{TeM}$
	1233-1271	5.1	-8.5	AgM
	1271-1600	30.1	11.2	TeB
MnTe	0- 723	45.0	-5.8	—
	723-1271	53.6	5.8	TeM
	1271-1517	78.6	25.5	TeB
	1517-1800	85.0	29.7	MnM
CoTe	0- 723	130.0	5.1	—
	723-1116	138.4	16.7	TeM
	1116-1271	142.4	20.3	CaM
	1271-1756	167.4	40.0	TeB
	1756-2000	239.4	81.0	CuB
$\text{Sb}_2\text{Te}_3$	0- 723	9.0	-1.7	—
	723- 893	17.4	9.9	TeM
	893-1271	8.5	-0.1	SbM
	1271-1600	33.5	24.9	SbB
$\text{Bi}_2\text{Te}_3$	0- 544	12.5	-1.3	—
	544- 723	15.9	5.1	BiM
	723- 860	24.3	16.7	TeM
	860-1271	15.7	6.7	$\text{Bi}_2\text{Te}_3\text{M}$
	1271-1600	40.7	26.4	TeB

\* M - melts  
B - boils  
S - sublimes

## Section II

there was an increase in the oxygen content of the crystal measured by combustion analysis (with  $x$  in  $\text{EuO}_x$  increasing from a minimum value of 0.970 for an Eu-rich solution to a maximum value of 1.017 for an O-rich solution) and a decrease in the lattice parameter (from  $5.1450\text{\AA}$  to  $5.1423\text{\AA}$ ). In addition, the electrical resistivity of the crystals varied with solution composition and crystal position in the ingot. The resistivities of the first-to-freeze portions were too high to be measured, while those of the last-to-freeze portions ranged from  $10^{-1}$  ohm-cm for crystals grown from Eu-rich solutions to about 50 ohm-cm for crystals grown from solutions expected to be congruently melting.

In order to obtain further data on the influence of deviations from stoichiometry on the electrical properties of  $\text{EuO}$ , samples with compositions on the Eu-rich and O-rich limits of the homogeneity range have been prepared by annealing high-resistivity samples from the first-to-freeze portions of a crystal grown from a Eu-rich solution. (The total impurity content of the crystal detected by mass spectrographic analysis was less than 200 ppma.) Each sample was annealed at  $1400^\circ\text{C}$  for 48 hours, in a sealed tungsten capsule, in the vapor over a mixture of two solid phases: Eu-EuO for Eu saturation and  $\text{EuO}-\text{Eu}_3\text{O}_4$  for O saturation. Since in each case three phases (including the gas phase) are present, according to Gibbs' phase rule the partial pressures of  $\text{Eu(g)}$  and  $\text{O}_2(\text{g})$  are fixed by the temperature only. In order to achieve equilibrium with the vapor, the sample must change its composition by solid state diffusion until it becomes either as Eu-rich or as O-rich as possible at the annealing temperature, depending on whether excess Eu or excess  $\text{Eu}_3\text{O}_4$  is present in addition to  $\text{EuO}$ .

The annealed samples differ markedly from the as-grown crystal, whose resistivity was too high to measure at any temperature, and from each other. The resistivity of the O-saturated sample is about  $5 \times 10^3$  ohm-cm at room temperature and increases slowly and smoothly with decreasing temperature to about  $5 \times 10^4$  ohm-cm at  $50^\circ\text{K}$ . The resistivity of the Eu-saturated sample is about  $10^2$  ohm-cm at room temperature, rises to a maximum of about  $10^3$  ohm-cm near  $80^\circ\text{K}$ , and then drops by almost 6 orders of magnitude to about  $10^{-3}$  ohm-cm at  $50^\circ\text{K}$ . This behavior, which is associated with the ferromagnetic transition in  $\text{EuO}$  (Curie point of  $69^\circ\text{K}$ ), has also been observed in some as-grown samples taken from the last-to-freeze portions of solution-grown ingots, and has been discussed previously.<sup>9</sup>

The striking differences between the Eu-saturated, as-grown, and O-saturated crystals show that deviations from stoichiometry are of great importance in determining the properties of  $\text{EuO}$ , although no detailed mechanism will be proposed at this time. The earlier results of combustion analysis on as-grown samples indicate that the homogeneity range extends on both sides of the stoichiometric composition, but even this conclusion should be regarded as tentative until the annealed samples are analyzed. It should be noted that lattice parameter measurements on these samples are apparently inconsistent with those made earlier on as-grown samples. The parameters measured for the Eu-saturated, as-grown, and O-saturated samples are respectively  $5.1422$ ,  $5.1432$ , and  $5.1438\text{\AA}$ , with an estimated uncertainty of  $+0.0005\text{\AA}$ . Thus the parameter increases with increasing oxygen content, whereas exactly the opposite trend was observed with as-grown samples.

The method used to prepare Eu-saturated and O-saturated  $\text{EuO}$  is based on the mutual dependence of the compositions of solid  $\text{EuO}$  and the vapor phase with which it is in equilibrium. At any temperature, solid  $\text{EuO}$  is stable only over a limited range of  $\text{Eu(g)}$  partial pressures. The maximum possible  $\text{Eu(g)}$  pressure is that in equilibrium with Eu-saturated  $\text{EuO}$ , and the

minimum possible pressure is that in equilibrium with O-saturated EuO. The available data on these limiting pressures are summarized by the  $\log p - 1/T$  plot shown in Fig. II-6. The pressures of Eu(g) are given by the upper loop, whose upper leg should give the pressure over Eu-saturated EuO. The solid line shown is actually the vapor pressure of pure liquid Eu metal,<sup>10</sup> which is given by  $\log p_{\text{Eu}}(\text{atm}) = 4.22 - 7,900/T$ . This represents an upper limit for the pressure over EuO over the entire temperature range, and over most of the range it should be a very good approximation to the actual Eu-saturated pressure, since the solubility of oxygen in Eu is small except at temperatures approaching the melting point of EuO.

The lower leg of the Eu(g) pressure loop in Fig. II-6 gives the pressures in equilibrium with O-saturated EuO. The solid portion gives

recent data<sup>11</sup> for these pressures, obtained by measurements on EuO-Eu<sub>3</sub>O<sub>4</sub> mixtures, which are represented by the equation  $\log p_{\text{Eu}}(\text{atm}) = 6.25 - 16,590/T$ . The loop was completed by extrapolating this leg and the upper leg to meet at the melting point of EuO, 2015°C (Ref. 8).

The lower loop in Fig. II-6 gives the limiting O<sub>2</sub>(g) pressures in equilibrium with EuO. In this case the upper leg is for O-saturated and the lower leg for Eu-saturated EuO. The pressures shown were calculated from the Eu(g) pressures of the upper loop by using the equilibrium constant  $\log K = \log (p_{\text{Eu}}^2 p_{\text{O}_2}) = 18.4 - 80,200/T$ , which was evaluated from published data for the free energy of formation of EuO (Ref. 12).

It is seen from Fig. II-6 that at any fixed temperature the maximum O<sub>2</sub>(g) pressure in equilibrium with EuO is many orders of magnitude less than the minimum Eu(g) pressure. Therefore EuO has no congruently subliming composition. If a sample is heated in a dynamic vacuum or an inert gas stream it will lose Eu until it reaches the O-saturated boundary of the homogeneity range, after which continued vaporization will result in the formation of Eu<sub>3</sub>O<sub>4</sub>.

T. B. Reed  
R. E. Fahey  
M. R. Oliver

#### E. COMPOSITION DEPENDENCE OF ENERGY GAP IN ZnTe<sub>1-x</sub>Se<sub>x</sub> AND ZnTe<sub>1-x</sub>S<sub>x</sub> ALLOYS

The II-VI compounds ZnTe and ZnSe form a complete series of solid solutions. On the basis of diffuse reflectance measurements at room temperature on alloy powder samples, Larach, Shrader, and Stocker<sup>13</sup> reported a minimum in the energy gap as a function of composition at about 35 mole percent ZnSe. Although later reflectivity measurements by Halsted, Marple,

Section II

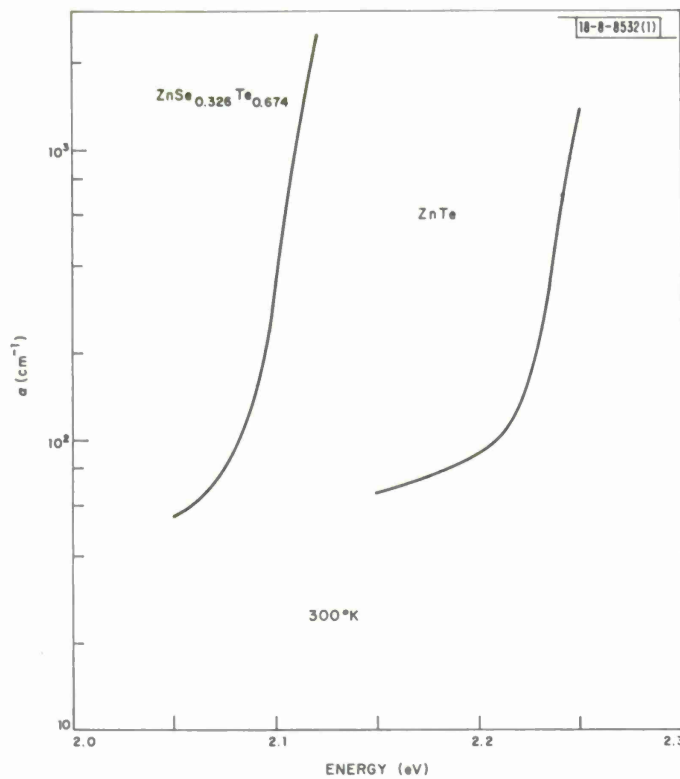


Fig. II-7. Absorption coefficient ( $\alpha$ ) at room temperature vs photon energy for ZnTe and  $\text{ZnSe}_{0.326}\text{Te}_{0.674}$ .

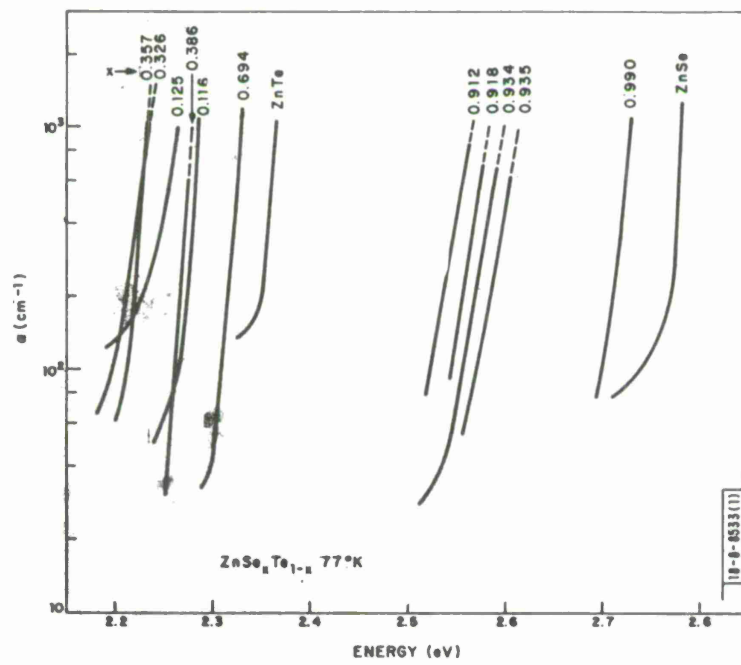


Fig. II-8. Absorption coefficient ( $\alpha$ ) at 77°K vs photon energy for  $\text{ZnTe}_{1-x}\text{Se}_x$  alloys.

and Aven<sup>14</sup> and absorption measurements by Aten,<sup>15</sup> all on single crystals, supported this finding, some workers still questioned the existence of a minimum. We became interested in this problem because of our work with the oxygen photoluminescence band in these alloys.<sup>16</sup> In order to resolve the issue, we have made an extensive series of optical transmission measurements on thin samples prepared from alloy single crystals. Our results confirm the existence of the energy gap minimum.

All the crystals, including those of ZnTe and ZnSe, were grown from the vapor phase at temperatures ranging from 1080°C for ZnTe to 1180° for ZnSe. Annealing under Zn saturation at 1000° to 1050°C and furnace cooling generally left the samples fairly homogeneous and largely free of precipitates. Alloy compositions were determined by electron microprobe analysis. Mass spectrographic analysis of several boules showed a few ppma of a small number of impurities, always including Cu and Na. The resistivity of typical Zn-annealed samples ranged from about 100 ohm-cm for ZnTe to 10<sup>6</sup> ohm-cm or higher for alloy samples containing more than 50 mole percent ZnSe. Samples large enough to cover a 1/2-mm diameter aperture were ground and polished to thicknesses between 20 and 70 μm. Transmission measurements were made with a grating spectrometer with resolution better than 2 Å. Absorption constants in the region of interest, generally from 100 to 1000 cm<sup>-1</sup>, were calculated by using a value of 0.26 for the reflectivity.

Figure II-7 shows the absorption coefficient ( $\alpha$ ) at room temperature as a function of photon energy for a ZnTe sample and an alloy sample containing 33 mole percent ZnSe. The absorption edge of the alloy, which has been measured to  $\alpha = 3000 \text{ cm}^{-1}$ , is seen to be comparable in steepness to that of ZnTe. For both samples there is a tail below about 100 cm<sup>-1</sup> which is probably due either to impurity absorption, work damage produced by polishing, or both. For ZnTe, the energy for  $\alpha = 1000 \text{ cm}^{-1}$  is within 0.020 eV of the energy gap, which is known to be 2.25 eV from electroreflectance measurements.<sup>17</sup> Figure II-8 shows similar data for a number of samples immersed in liquid nitrogen. In general the absorption edges for the alloys are comparable in steepness to those for ZnTe and ZnSe.

Figure II-9 is a plot of the energy for which  $\alpha = 1000 \text{ cm}^{-1}$  vs  $x$ , the mole fraction of ZnSe. At both 77° and 300°K there is a minimum in this energy close to  $x = 0.3$ . The minimum value is about 0.14 eV below the value for ZnTe. We believe that the energy gaps can be obtained with considerable accuracy by simply adding 0.020 eV to the plotted values. The data of Larach, *et al.*,<sup>13</sup> for the energy gap at room temperature, obtained by diffuse reflectance measurements, are in excellent agreement with our results. The energy difference between 300° and 77°K is essentially constant across the whole composition range. It looks larger near the minimum but this is an optical illusion due to the changing slopes of the curves.

For several pseudobinary III-V alloy systems Thompson and Woolley<sup>18</sup> have found that energy gap data as a function of composition can be fitted by the parabolic expression  $E_G = A + Bx + Cx^2$ . This expression also gives a moderately good fit to the present data, as shown by Fig. II-10 where the room temperature data have been replotted. Van Vechten and Bergstresser<sup>19</sup> have recently reported that with one adjustable parameter a dielectric two-band model in the virtual crystal approximation can semi-quantitatively predict the coefficient of  $x^2$  in the parabolic expression for the energy gaps of many III-V and II-VI alloy systems.

Section II

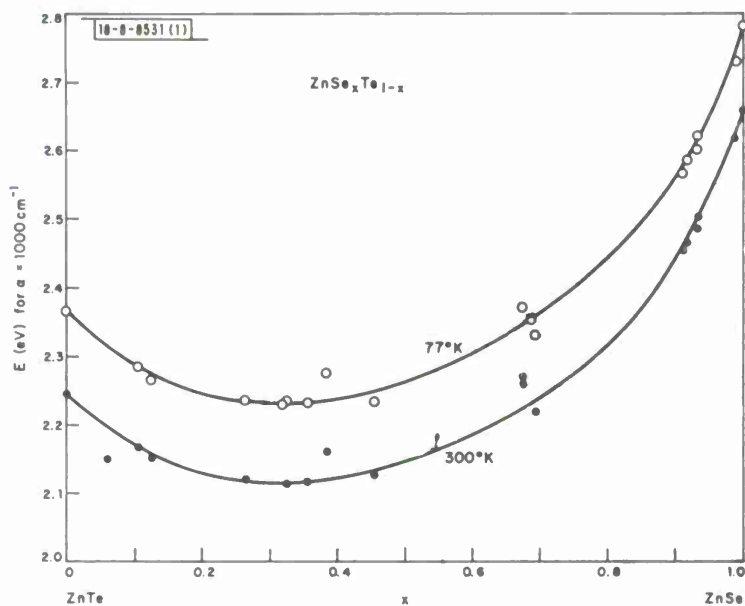


Fig. II-9. Photon energy for  $\alpha = 1000 \text{ cm}^{-1}$  at  $77^\circ$  and  $300^\circ\text{K}$  vs mole fraction  $x$  in  $ZnTe_{1-x} Se_x$  alloys.

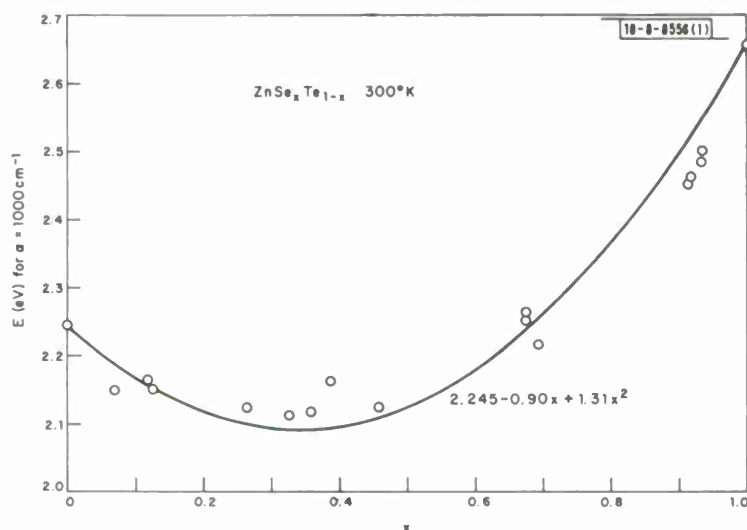


Fig. II-10. Photon energy for  $\alpha = 1000 \text{ cm}^{-1}$  at  $300^\circ\text{K}$  vs mole fraction  $x$  in  $ZnTe_{1-x} Se_x$  alloys: comparison of parabolic equation with experimental data.

Having confirmed the energy gap minimum in the ZnTe-ZnSe system, we turned our attention to the ZnTe-rich side of the ZnTe-ZnS system, which is also of interest because of the oxygen photoluminescence band. The solubility of ZnS in ZnTe is limited to about 5 mole percent at 900°C and about 20 mole percent at 1200°C.<sup>20</sup> Single crystals containing up to 15 mole percent ZnS were grown from the vapor phase, although the yield was much lower than for the ZnTe-ZnSe system. The samples were prepared and measured in the same manner as the ZnTe-ZnSe samples except that after annealing they were quenched in water in order to prevent decomposition due to the retrograde solubility of ZnS.

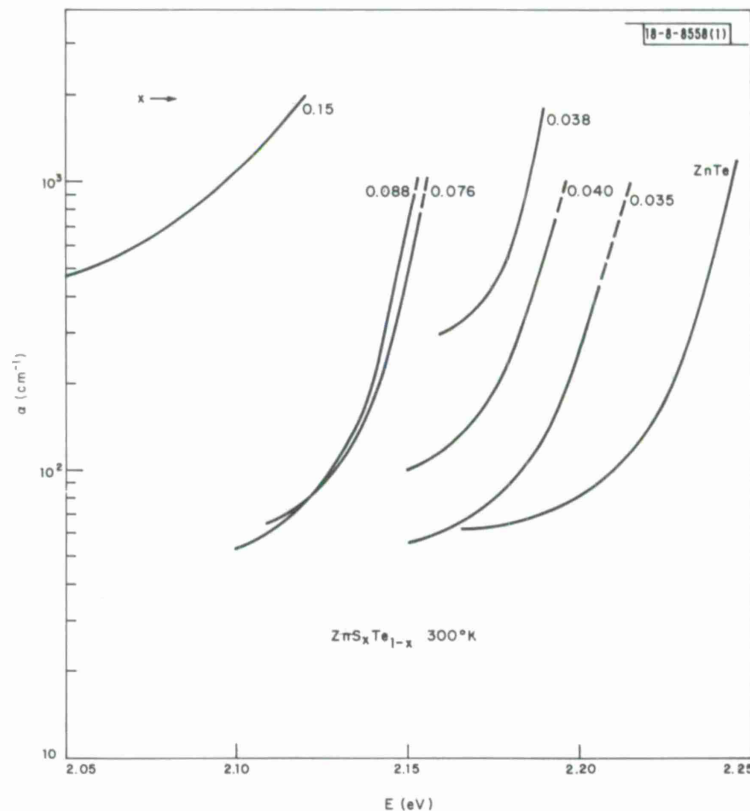


Fig. II-11. Absorption coefficient ( $\alpha$ ) at room temperature vs photon energy for  $ZnS_x Te_{1-x}$  alloys.

Figure II-11 shows the room temperature absorption data for the ZnTe-ZnS alloys. Except for the sample with an average composition of 15 mole percent ZnS, the absorption edges at sufficiently high absorption coefficients are comparable in steepness to that of ZnTe. The 15 mole percent sample was inhomogeneous, with measured composition varying from about 12 to 18 mole percent ZnS, while the others were homogeneous to within 0.5 mole percent.

In Fig. II-12 the energy for  $\alpha = 1000 \text{ cm}^{-1}$  is plotted versus  $x$ , the mole fraction of ZnS. Although the energy gap of ZnS is 1.5 eV greater than that of ZnTe, adding ZnS to ZnTe causes a rather rapid decrease in the energy gap of the alloys. The curve shown is not extended to the point at  $x = 0.15$  because of the uncertainty in that point. A minimum cannot be observed because

Section II

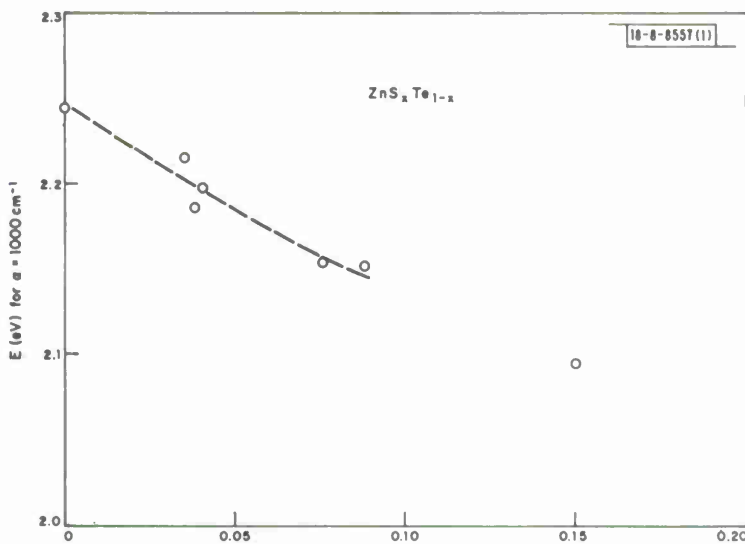


Fig. II-12. Photon energy for  $\alpha = 1000 \text{ cm}^{-1}$  at room temperature vs mole fraction  $x$  in  $\text{ZnTe}_{1-x}\text{S}_x$  alloys.

samples with high enough ZnS content cannot be prepared. However, it is clear that the ZnTe-ZnS system provides another example of a strongly nonlinear dependence of energy gap on alloy composition.

G. W. Iseler

#### F. ENERGY GAP MINIMUM IN $\text{CdTe}_{1-x}\text{Se}_x$ ALLOYS

The composition dependence of the energy gap in CdTe-CdSe alloys has been determined by means of optical transmission measurements at room temperature. The data establish the existence of an energy gap minimum, which was anticipated at the outset of the investigation because such a minimum had been reported in the ZnTe-ZnSe system,<sup>13</sup> although it was not universally accepted at that time. (The minimum in the ZnTe-ZnSe system has now been confirmed by the study described in the preceding section of this report.)

The phase diagram for the CdTe-CdSe system has recently been determined.<sup>21</sup> Since CdTe has the cubic zincblende structure and CdSe has the hexagonal wurtzite structure, a complete series of solid solutions with the same structure is not formed. Instead, there are two broad single-phase regions in the solid phase, one including CdTe and alloys with zincblende structure and the other including CdSe and alloys with wurtzite structure. These are separated by a two-phase region only about 3 mole percent wide, whose boundaries shift toward increasing CdSe content with decreasing temperature. For compositions between about 30 and 50 mole percent CdSe it is possible to obtain alloys with either structure, depending upon preparation, annealing, and cooling conditions.

The samples studied in this investigation were single crystals cut from polycrystalline ingots grown from the melt by directional freezing. Most of the ingots were prepared from stoichiometric melts by the Bridgman method. One ingot containing about 60 mole percent CdSe was prepared from stoichiometric material by a zoning technique, and an ingot of CdSe was obtained from an Se-rich solution by the temperature gradient solution zoning method.<sup>22</sup> According to the

phase diagram, melts containing more than 20 mole percent CdSe crystallize in hexagonal form. However, three cubic crystals were obtained with compositions between 30 and 45 mole percent CdSe. One of these was transformed to the cubic form during furnace cooling of a Bridgman-grown ingot, and the others were transformed from as-grown hexagonal crystals by annealing at temperatures below the hexagonal-to-cubic transition temperature. Measurements were also made on a sample containing 49 mole percent CdSe which X-ray diffraction data indicated to be a polytype of unidentified structure. This polytype was apparently formed during furnace cooling as a metastable intermediate in the hexagonal-to-cubic transformation.

Transmission measurements in the vicinity of the absorption edge were made at room temperature with a single pass prism spectrometer on samples ground to a thickness of about  $80\mu\text{m}$  and optically polished but not etched. Absorption coefficients were calculated by assuming a fixed reflectivity for each composition, ranging from 0.24 for CdTe to 0.20 for CdSe.

Figure II-13 shows semi-logarithmic plots of absorption coefficient vs photon energy for representative samples with cubic, hexagonal, and polytype structure. The compositions of the alloys, which were determined by electron microprobe analysis, are specified by giving the mole fraction of CdSe, that is,  $x$  in  $\text{CdTe}_{1-x}\text{Se}_x$ . For CdTe, CdSe, and alloys with  $x$  less than 0.4, the plots are linear at the upper end of the absorption coefficient range. For these alloys, the absorption edges are comparable in steepness to that of CdTe, which is in good agreement with the data of Marple.<sup>23</sup> The absorption edges for alloys with higher CdSe content are nonlinear and less steep. In all cases there is a tail at the lower end of the absorption range which is probably due to impurity absorption, work damage produced during polishing, or both.

The energy gap for each sample was found by adding 0.020 eV to the photon energy for which the absorption coefficient is  $400\text{ cm}^{-1}$ . This procedure gives values of 1.50 and 1.71 eV for the energy gaps of CdTe and CdSe, respectively, in good agreement with the published values. The energy gaps obtained in this manner for all the samples are plotted vs mole fraction of CdSe in Fig. II-14. Data have been obtained for cubic samples with  $x$  between 0 and 0.45. Alloying CdTe with CdSe initially produces a marked decrease in the energy gap. This continues until about  $x = 0.35$ , after which there is no significant change. These results are sufficient to establish the existence of an energy gap minimum in the CdTe-CdSe system. The density of data points for hexagonal samples is much lower than for cubic, because the preparation of alloys with high CdSe content is made difficult by their high melting points. The limited data available, particularly for the point at  $x = 0.35$ , indicate that the energy gap is systematically higher by about 0.03 eV for hexagonal samples than for cubic. A difference of this magnitude would not be surprising, since the energy gap of ZnS, which is about 3.8 eV at room temperature, is about 0.1 eV greater for the hexagonal form than for the cubic. The energy gap value for the polytype alloy sample, which appears to be intermediate between the values for hexagonal and cubic samples, is also consistent with the results for ZnS, since the energy gaps of ZnS polytypes lie between those of the wurtzite and zincblende forms.<sup>24</sup>

The energy gap data for the cubic and hexagonal CdTe-CdSe alloys as a function of  $x$  are well represented by the curves in Fig. II-14 labelled (1) and (2), respectively. These curves were calculated from the equations shown, which have the parabolic form used by Thompson and Woolley<sup>18</sup> to fit energy gap data for a number of III-V alloy systems. The same coefficients of  $x$  and  $x^2$  have been chosen for both equations, so that the only difference between them is in the

## Section II

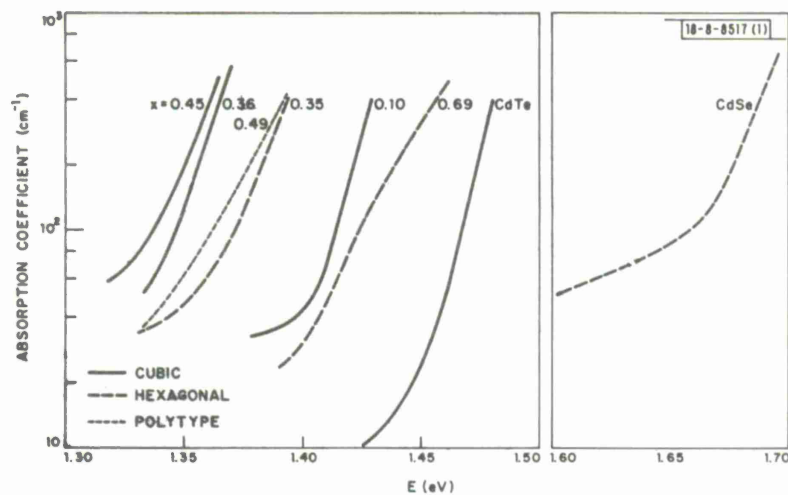


Fig. II-13. Absorption coefficient ( $\alpha$ ) at room temperature vs photon energy for  $\text{CdTe}_{1-x}\text{Se}_x$  alloys.

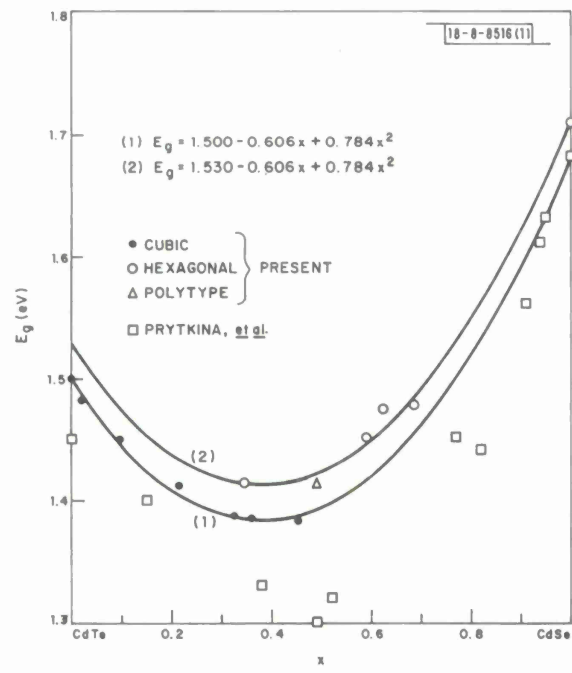


Fig. II-14. Energy gap at room temperature vs mole fraction  $x$  in  $\text{CdTe}_{1-x}\text{Se}_x$  alloys.

value of the first term, which gives the energy gap of CdTe. Therefore, the calculated energy gap values for the cubic and hexagonal forms differ by a constant amount, 0.03 eV, over the entire composition range. (The apparent variation in this difference in Fig. II-14 is an optical illusion.)

Figure II-14 also shows the energy gap data for CdTe-CdSe alloys obtained by Prytkina, et al.,<sup>25</sup> from absorption measurements. They too observe a minimum in the energy gap, but in comparison with our results the minimum is somewhat deeper and occurs at higher CdSe content. In addition, their energy gap values are systematically lower than ours, as shown by the results for CdTe and CdSe. It is not possible to give an explanation for these differences, since Prytkina, et al., do not present any absorption data or describe their procedure for evaluating the energy gap from the data.

A. J. Strauss

### G. ENERGY-LEVEL SCHEME FOR $\text{Ni}_{1-\delta}\text{O}: \text{Li}$

Evidence for localized d electrons in  $\text{MnO}$ ,  $\text{Fe}_{1-\delta}\text{O}$ ,  $\text{CoO}$  and  $\text{NiO}$  comes from optical-absorption spectra, the magnitudes of the atomic moments, and Jahn-Teller distortions below  $T_N$  in  $\text{Fe}_{1-\delta}\text{O}$  and  $\text{CoO}$ . On the other hand, dielectric loss measurements on  $\text{NiO:Li}$  ceramics indicate that any activation energy for hopping of the hole trapped at an  $\text{Li}^+$  center is  $< 0.01$  eV, and transport measurements have shown that although the activation energy for the conductivity is  $0.4 < q < 0.85$  eV in the temperature range  $300 < T < 1000^\circ\text{K}$ , the mobilities are not activated. These facts have led to a variety of speculations in the literature about the character of the d electrons and of the positive charge carriers. In none of these speculations has serious attention been given to the role of native defects.

Optical absorption and electroreflectance spectra permit placement of the ground state of the d-state manifold relative to the edge of the conduction band, as shown in Fig. II-15. The  ${}^6\text{A}_{1g}(\text{Mn}^{2+})$  level is relatively stable because of the large intra-atomic exchange stabilization associated with a half filled, high spin d shell. Otherwise there is a progressive stabilization with increasing atomic number. From band-calculation estimates and a shoulder in the absorption spectrum, the energy gap between the  $\text{O}^{2-}:2\text{p}$  bands and the  $\text{Ni}^+:d^84\text{s}$  band in  $\text{NiO}$  is about 5.5 eV.

$\text{MnO}$ ,  $\text{Fe}_{1-\delta}\text{O}$ ,  $\text{CoO}$  and  $\text{NiO}$  are all anion-excess compounds. The predominant defects are cation vacancies. Given localized d electrons, an isolated cation vacancy  $V_c$  traps a pair of

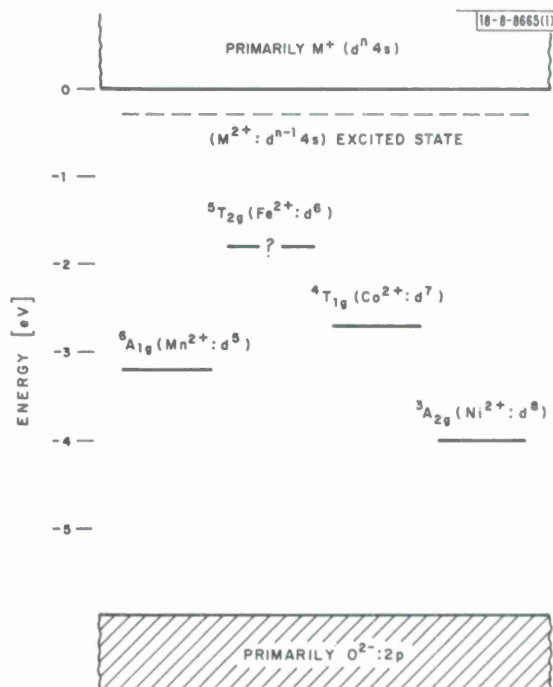


Fig. II-15. Energy level diagram for  $\text{MnO}$ ,  $\text{FeO}$ ,  $\text{CoO}$ , and  $\text{NiO}$  in the absence of lattice defects.

## Section II

trivalent cations, one on each side of it, and the first and second ionization potentials may be estimated as

$$\epsilon_1 \approx (2e^2/\kappa R) - (e^2/2\kappa R) \approx 0.6 \text{ eV} \quad (\text{II-2})$$

$$\epsilon_2 \approx 2e^2/\kappa R \approx 0.8 \text{ eV} \quad (\text{II-3})$$

where  $\kappa \approx 12$  is the dielectric constant and  $R$  is the nearest-neighbor cation-cation separation. The corresponding modification of Fig. II-15 is the creation of two  $M^{2+}:V_c$  levels above the filled ground-state  $M^{2+}$  level, as shown in Fig. II-16 for NiO. Although the  $Ni^{2+}:V_c$  levels are empty in the diagram, the axis of the  $Ni^{III}-V_c-Ni^{III}$  triplet may be rotated by an external electric field, the holes being free to hop between the twelve cations neighboring the cation vacancy.

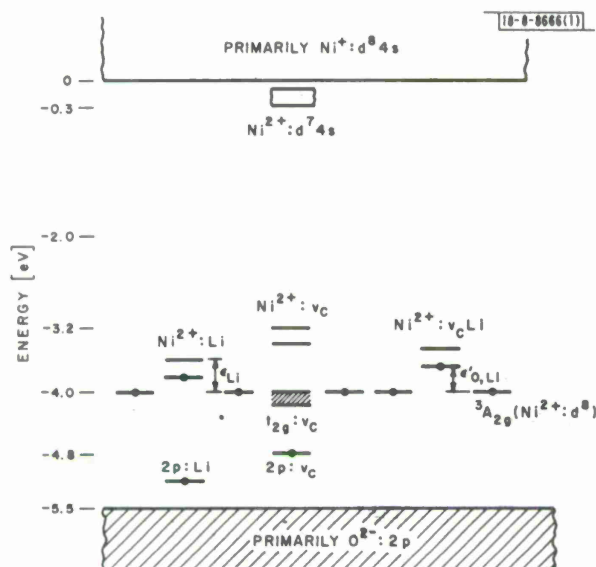


Fig. II-16. Energy level diagram for NiO, showing levels due to cation vacancies and Li impurity atoms.

Low-spin  $Ni^{III}$  ions are created from high-spin  $Ni^{2+}$  ions by the removal of an  $e_g$  electron (electron in an orbital that  $\sigma$  bonds with  $O^{2-}$  ions), and these may be localized to the cation to create discrete  $Ni^{III}$  ions. On the other hand, the  $t_{2g}$  orbitals, which are directed toward near-neighbor cations, are strongly perturbed by a cation vacancy. In fact, each cation vacancy would create symmetrized trap orbitals consisting of linear combinations of  $t_{2g}$  orbitals from neighboring cations admixed with anion  $p_\sigma$  orbitals that would  $\sigma$ -bond to the vacancy.

In  $TiO_x$  and  $VO_x$ , where the  $e_g$  orbitals are empty and the  $t_{2g}$  electrons are itinerant, these trap orbitals are lifted above the Fermi energy. In NiO, where localized holes are created by the removal of an  $e_g$  electron, removal of a trap electron requires the additional crystal-field energy  $10Dq$ . However, the added covalent mixing in the trap orbitals reduces the effective  $10Dq$  by about 1 eV, which places the energy of the trap orbitals, designated  $t_{2g}:V_c$  in Fig. II-16, about 1 eV below the  $Ni^{2+}:V_c$  localized-hole levels, or approximately at the  $^3A_{2g}(Ni^{2+}:d^8)$  level in Fig. II-16. In addition, a second trap orbital is lifted out of the  $O^{2-}:2p$  bands, in analogy to the anion-vacancy trap orbital dropped from the conduction band in alkali halides to form a color

center. This cation-vacancy trap orbital is designated  $2p:V_c$  in Fig. II-16. Because the  $t_{2g}:V_c$  and  $2p:V_c$  trap orbitals have the same symmetry, they mix with one another. This means that the closer the  $2p:V_c$  level comes to the  $t_{2g}:V_c$  level, the more 2p character is imparted to the  $t_{2g}:V_c$  orbital and hence the more extended it is in real space. It follows that, with strong mixing and relatively large concentrations [ $V_c$ ] of cation vacancies, holes in the  $t_{2g}:V_c$  levels may tunnel without activation energy between neighboring sites.

In Fig. II-16, the  $t_{2g}:V_c$  level is shown broadened into a narrow impurity band. Finally, the Fermi energy  $\epsilon_F$  would lie between the  $t_{2g}:V_c$  level (or band) and the first-ionization level at  $\epsilon_1$ . However, from Fig. II-15 it is clear that any iron or cobalt impurities would act as donor centers:  $Fe^{2+} \rightarrow Fe^{3+} + e^-$ , where the electrons fall into the levels at  $\epsilon_1$ . Thus the model accounts well for  $0.4 < q < 0.85$  eV from the resistivity vs temperature measurements, for variation in  $\sigma$  vs  $[PO_2]$  with iron impurities, and for isotropic p-type conduction having a small ( $\mu_d \approx 0.3$  cm<sup>2</sup>/V-sec), unactivated mobility while simultaneously preserving the localized character of the d electrons at the  $Ni^{2+}$  ions not neighboring a cation vacancy.

Since the  $Ni^{2+}-O^{2-}-Ni^{III}$  interactions are ferromagnetic whereas  $Ni^{2+}-O^{2-}-Ni^{2+}$  interactions are antiferromagnetic, it is also possible to rationalize with this model a  $\Delta q \approx 0.2$  eV on raising the temperature through  $T_N$ , an absorption peak at 0.24 eV below  $T_N$ , and a photocurrent peak at 0.23 eV in room-temperature, amorphous NiO films.

In order to generalize Fig. II-16 to include lightly Li-doped NiO, it is only necessary to add  $Ni^{2+}:Li$  levels, which represent the trapping energy

$$\epsilon_{Li} = e^2/\kappa R \approx 0.4 \text{ eV} \quad (\text{II-4})$$

of an  $Ni^{III}$  ion to a near-neighbor site of an  $Li^+$  ion. This energy is in good agreement with the appearance of an additional optical absorption peak at 0.43 eV in Li-doped NiO

J. B. Goodenough

#### H. POLARON MORPHOLOGY IN VANADIUM SPINELS FROM SEEBECK COEFFICIENTS

From a study<sup>26</sup> of the series of spinels  $M^{2+}[V_2^{3+}]O_4$ , it was possible to infer that the critical V-V separation  $R_c$  for a transition from localized to itinerant vanadium d electrons is approached in  $Mg[V_2]O_4$  and  $Zn[V_2]O_4$ , where  $R \approx 2.97 \text{ \AA}$ .  $Li^+[V_2]O_4$  is metallic and Pauli paramagnetic,<sup>27</sup> indicating itinerant d electrons, and variations in the physical properties with  $x$  in  $A_{1-x}^{2+}Li_x[V_2]O_4$ ,  $A = Mg$  or  $Zn$ , have suggested a critical composition  $x_c \approx 0.55$ , corresponding to  $R \approx 2.94 \text{ \AA}$ , for a transition from small-polaron to itinerant d electrons.<sup>28</sup> However, it was noted<sup>29</sup> that the Seebeck coefficients, although temperature-independent as required by the small-polaron formula

$$\Theta_+ = 198 \log [(N-p)/p] + S_t^*/e \quad (\text{II-5})$$

are not described by Eq. (II-5) either in this system or in the systems  $Mg[B_x^{2+}V_{2-x}]O_4$ , where  $B = Mg$  or  $Ni$ , if the number  $N$  of sites available to the p polarons is taken as the number of vanadium ions. In oxides  $S_t^*/e < 10 \mu\text{V}/^\circ\text{K}$  is small relative to the first term, so that Eq. (II-5) contains no adjustable parameters and therefore represents a strong constraint on any microscopic model for the polarons. Since  $p$  is given by the chemical composition, the model-dependent parameter is  $N$ . Adjustment of  $N$  to allow for intermediate size polarons has provided a successful

Section II

TABLE II-3

WEIGHTED PROBABILITY COEFFICIENTS  $\alpha_n = p_n \lambda_n$  DESCRIBING NUMBER OF POLARON SITES ASSOCIATED WITH A B-SITE VANADIUM ION HAVING  $n$  MAGNESIUM NEAREST NEIGHBORS

$n$	$p_n$	Clusters	$\lambda_n$	$\alpha_n$
0	1	$2V_4$	1	1
1	6	$2V_2 + V_4$	$\frac{5}{2}$	15
2	15	$\frac{2}{5} (V_2 + V_4) + \frac{3}{5} (4V_2)$	3	45
3	20	$\frac{1}{10} V_4 + \frac{9}{10} (3V_2)$	$\frac{11}{4}$	55
4	15	$2V_2$	2	30
5	6	$V_2$	1	6
6	1	$V^{4+}$	2	2

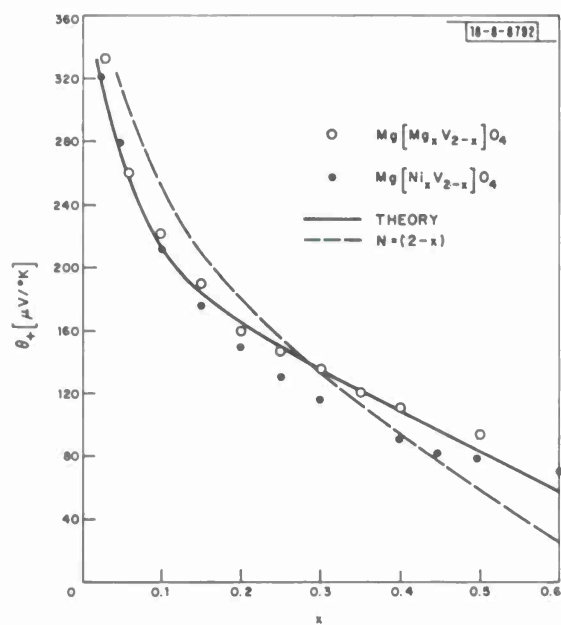


Fig. II-17. Seebeck coefficient vs  $x$  in  $\text{Mg}[\text{Mg}_x \text{V}_{2-x}] \text{O}_4$  and  $\text{Mg}[\text{Ni}_x \text{V}_{2-x}] \text{O}_4$  spinels.

interpretation of the temperature-independent Seebeck coefficients in the  $M_x V_2 O_5 - \beta$  systems,<sup>30</sup> which encourages use of the Seebeck coefficient to obtain indirect evidence of the morphology of the polarons in the vanadium spinels.

Examination of the crystal structure suggests three possible morphologies for polarons in spinels: (1) the charge carrier is localized to a discrete atomic position, creating an identifiable  $V^{4+}$  ion. (2) The charge carrier is shared between two neighboring cations, occupying a  $V_2$ -cluster molecular orbital. (3) The charge carrier is shared by the four neighboring cations of an elementary rocksalt-type cube, occupying a  $V_4$ -cluster molecular orbital. For the spinels  $A^{2+} [V_2]O_4$ , the molecular concentration  $N$  of available sites for each type of p-type polaron is

$$N(V^{4+}) = 2 \quad , \quad N(V_2) = 6 \quad , \quad N(V_4) = 1 \quad (II-6)$$

The third of these provides the only possible alternative for describing with Eq. (II-5) the measured Seebeck coefficients in  $A_{1-x}^{2+} Li_x [V_2]O_4$ ,  $A = Mg$  or  $Zn$ , and  $Mg[B_x^{2+} V_{2-x}]O_4$ ,  $B = Mg$  or  $Ni$ , spinels. However, with  $V_4$ -cluster polaron sites in the end members  $Mg[V_2]O_4$  and  $Zn[V_2]O_4$ , it is clear that in the systems  $Mg[B_x^{2+} V_{2-x}]O_4$  each  $B^{2+}$  ion disrupts the formation of  $V_4$  clusters, forcing nearest-neighbor vanadium ions to participate in  $V_2$  clustering instead. Therefore, in order to obtain  $N$  for the system, we must multiply the probability  $(1 - \frac{x}{2})$  of finding a vanadium ion on a particular site by the sum of the probabilities of finding 0, 1, ..., 6  $Mg$  nearest neighbors, each properly weighted by a factor  $\alpha_n$  that reflects the polaron clusters in which the vanadium ion participates. This weighting factor counts each  $V_4$  cluster as 1/2, each  $V_2$  cluster as 1 and the discrete  $V^{4+}$  ion as 2. This leads to

$$N = (1 - \frac{x}{2}) \sum_{n=0}^6 \alpha_n (\frac{x}{2})^n (1 - \frac{x}{2})^{6-n} \quad \text{and} \quad p = x \quad (II-7)$$

where the  $\alpha_n$  are given in Table II-3. Substitution of Eq. (II-7) into Eq. (II-5) with the constraint  $S_t^*/e = 0$  gives the solid curve of Fig. II-17.

Substitution of tetrahedral-site  $Li^+$  ions, on the other hand, can only increase the size of the polarons in the vicinity of the  $Li^+$  ions, since the electrons are all itinerant in the end member  $Li[V_2]O_4$ . The simplest model would have large-polaron clusters consisting of all the vanadium ions nearest-neighbor to  $Li^+$  ions. A negligible contribution to the Seebeck coefficient from charge carriers in these molecular orbitals is equivalent to  $2x$  polaron sites for  $p = x$ . Since the only intermediate-polaron sites are those  $V_4$  clusters having only A-site  $Mg^{2+}$  or  $Zn^{2+}$  ions as nearest neighbors, this gives an "effective"

$$N = 2x + (1 - x)^5 \quad \text{and} \quad p = x. \quad (II-8)$$

Jaskowsky,<sup>29</sup> although arguing from a different physical model, has already shown that these values of  $N$  and  $p$  in Eq. (II-5) give an excellent description of the measured Seebeck coefficients if  $S_t^*/e = 0$ , corresponding to no adjustable parameter.

In  $Fe[V_2]O_4$  the V-V separations are  $R = 2.99\text{\AA}$ , and in the system  $Fe[Fe_x V_{2-x}]O_4$  a conventional model ( $N = 2 - x$ ) is applicable for  $x > 0.15$ , the compositional range in which all the iron ions are divalent.

## Section II

These results illustrate use of a temperature-independent Seebeck coefficient to investigate polaron morphology and indicate that in the vanadium spinels the polarons change with decreasing V-V separation from identifiable  $V^{4+}$  cations to  $V_2$ -cluster and  $V_4$ -cluster polarons, and finally to itinerant electrons, in a narrow range  $2.99 > R > 2.94 \text{ \AA}$ . Furthermore, in the systems  $A_{1-x}^{2+} Li_x [V_2] O_4$ ,  $A = Mg$  or  $Zn$ , the polaron to itinerant-electron transition does not occur homogeneously at  $x_c \approx 0.55$ , but inhomogeneously in the vanadium shell of nearest neighbors to the  $Li^+$  ions.

J. B. Goodenough

## I. CRYSTAL STRUCTURE OF HEXAGONAL RbNiF<sub>3</sub>(6H)

<sup>+</sup>  $\text{ViF}_3$  exists in two modifications. At ambient pressure,<sup>31</sup> it has the hexagonal  $\text{BaTiO}_3$  (6H) structure<sup>32</sup> while at high pressure ( $\sim 25$  kbars) its structure transforms to the cubic perovskite type<sup>33, 34</sup> with  $a = 4.07 \text{ \AA}$ . This pressure transformation is similar to those found for many compounds with a general formula  $\text{ABX}_3$ , having hexagonal or cubic close-packed  $\text{AX}_3$  layers.<sup>33-36</sup>

The hexagonal form of  $\text{RbNiF}_3$  is of considerable interest because of its ferrimagnetic and optical properties. Since accurate bond distances and angles are necessary for any quantitative interpretation of physical properties, we undertook the refinement of the atomic position parameters of  $\text{RbNiF}_3(6\text{H})$ , as well as the determination of the temperature dependence of the lattice parameter.

We find the lattice parameters at room temperature to be  $a = 5.843 \text{ \AA}$  and  $c = 14.309 \text{ \AA}$ , which are identical to those previously reported.<sup>31</sup> The variation of the lattice parameters in the temperature range -175° to 600°C is shown in Fig. II-18. No change in symmetry or anomaly in the temperature dependence of the lattice parameters was noted over the entire temperature range, which includes the Curie point.

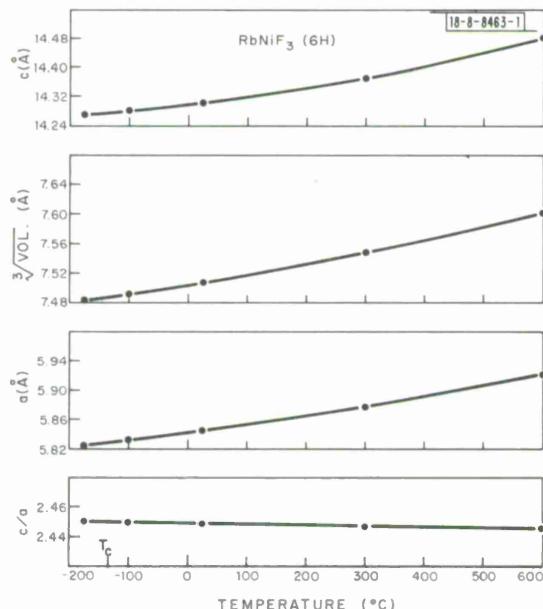


Fig. II-18. Crystallographic parameters of  $\text{RbNiF}_3$ (6H) as a function of temperature.

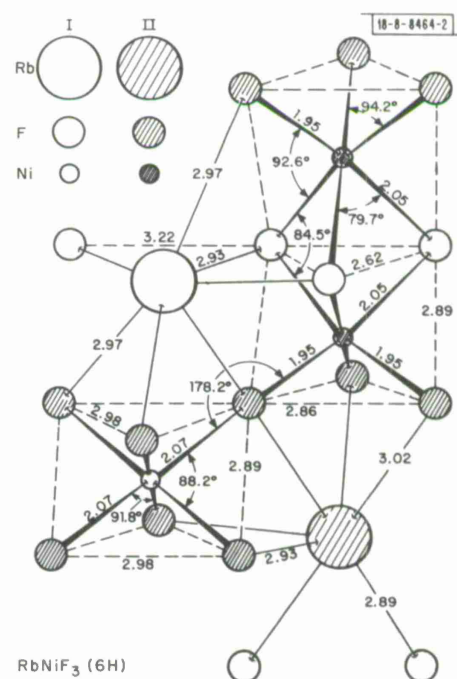


Fig. II-19. Essential features of the RbNiF<sub>3</sub>(6H) structure.

$\text{RbNiF}_3(6\text{H})$  has the hexagonal  $\text{BaTiO}_3$  structure indicated in Fig. II-19. It contains face-shared pairs of  $\text{NiF}_6$  octahedra connected by single octahedra sharing only corners. The rubidium ions, which fill the six large voids per unit cell of this octahedra network have twelvefold coordination. There are two different positions for each type of atom, as shown in Fig. II-19.

TABLE II-4  
CRYSTAL STRUCTURE OF  $\text{RbNiF}_3(6\text{H})$

Space Group	$P\bar{6}_3/mmc$ (No. 194)
Unit Cell Dimensions	$a = 5.843 \text{ \AA}$ ; $c = 14.309 \text{ \AA}$
Cell Contents	6 $\text{RbNiF}_3$
$\text{Rb}_{\text{I}}$ in (2b)	$\pm (0, 0, 1/4)$
$\text{Rb}_{\text{II}}$ in (4f)	$\pm (1/3, 2/3, z; 2/3, 1/3, 1/2 + z)$ $z = 0.0954(2), 0.0954(7)^*$
$\text{Ni}_{\text{I}}$ in (2a)	$(0, 0, 0; 0, 0, 1/2)$
$\text{Ni}_{\text{II}}$ in (4f)	$\pm (1/3, 2/3, z; 2/3, 1/3, 1/2 + z)$ $z = 0.8462(5), 0.8450(8)^*$
$\text{F}_{\text{I}}$ in (6h)	$\pm (x, 2x, 1/4; 2x, x, 3/4; x, \bar{x}, 1/4)$ $x = 0.517(1), 0.5023(82)^*$
$\text{F}_{\text{II}}$ in (12k)	$\pm (x, 2x, z; 2x, x, \bar{z}; x, \bar{x}, z; x, 2x, 1/2 - z; 2x, x, 1/2 + z,$ $\bar{x}, x, 1/2 + z)$ $x = 0.830(3), 0.8313(89)^*$ ; $z = 0.081(1), 0.0740(17)^*$
Cell Temperature Factor	$B = 1.9(1)$

\* Our results are listed first with estimated error limits in parentheses; Babel's results (37) are listed second for comparison.

The structure has only five variable parameters. Since the powder pattern is not complex, we chose to use intensity data collected on powdered samples. Refinement based on thirty-five intensities gave the cell temperature factor and the five variable position parameters listed in Table II-4 with a reliability factor  $R = 5.8$ . Babel's position parameters<sup>37</sup> from a single-crystal structure refinement are also included in Table II-4. They show good agreement with our cation parameters, but significant differences with our fluorine positions. Most affected by this discrepancy are the  $\text{F}_{\text{I}}-\text{F}_{\text{I}}$  distances and  $\text{Ni}_{\text{II}}-\text{F}_{\text{I}}-\text{Ni}_{\text{II}}$  angle. We find these distances to be 2.62 and 3.22  $\text{\AA}$ , compared to Babel's values of 2.88 and 2.96  $\text{\AA}$ , and we find the angle to be  $84.5^\circ$ , compared to Babel's value of  $78.5^\circ$ .

One can only speculate as to why there is a difference between our results and those of Babel. We do feel however that our atomic positions are more probable since they are in agreement with similar structures,<sup>32, 37, 38</sup> NMR data<sup>39</sup> on  $\text{RbNiF}_3(6\text{H})$ , and our understanding of electrostatic repulsion and screening. A detailed discussion of the  $\text{RbNiF}_3$  structure will be presented elsewhere.<sup>40</sup>

R. J. Arnott    J. R. O'Connor  
J. M. Longo

## Section II

TABLE II-5  
X-RAY DATA FOR ATMOSPHERIC PRESSURE FORM OF  $\text{CsMnCl}_3(9R)$   
 $a = 7.288 \text{ \AA}$ ,  $c = 27.44 \text{ \AA}$  (Ref. 42)

hkl	$I_{\text{calc}}$	$I_{\text{obs}}$	$d_{\text{obs}}$
1 0 4	25.5	24	4.64
0 1 5	43.5	45	4.13
1 1 0	87.4	80	3.64
1 0 7	8.6	10	3.33
0 2 1	12.0	13	3.13
2 0 2	5.2	6	3.07
0 0 9	29.4	34	3.04
0 1 8	23.5	20	3.01
0 2 4	71.5	67	2.864
2 0 5	100.0	100	2.732
1 0 10	10.3	13	2.516
0 2 7	14.1	18	2.458
1 1 9	3.4	2	2.342
2 0 8	21.1	28	2.319
0 1 11	3.8		
2 1 4	9.5	8	2.252
1 2 5	17.5	20	2.187
3 0 0	19.1	20	2.104
0 2 10	25.8	16	2.070
2 1 7	4.2	6	2.037
1 0 13	7.5	6	2.000
1 2 8	11.4	14	1.957
2 0 11	4.2		
0 1 14	2.1	2	1.872
2 2 0	44.7	45	1.823
2 1 10	6.4	8	1.799
0 2 13	16.5	14	1.753
1 2 11	2.5	2	1.725
1 3 4	3.5	3	1.696
3 1 5	6.9	20	1.664
2 1 14	15.1		

### J. EFFECT OF PRESSURE ON CRYSTAL STRUCTURE OF $\text{CsMnCl}_3$ , $\text{RbMnCl}_3$ , AND $\text{RbFeCl}_3$

The structures of  $\text{ABX}_3$  compounds, where A is a large univalent cation with  $1.0 < r_A < 1.9 \text{\AA}$  and B is a smaller divalent cation with  $0.5 < r_B < 1.0 \text{\AA}$ , can be described in terms of the hexagonal or cubic close packing of  $\text{AX}_3$  layers. Among the  $\text{ABF}_3$  and  $\text{A}^{2+}\text{B}^{4+}\text{O}_3$  compounds there are structures stable at atmospheric pressure in which the packing is entirely cubic (perovskite structure) or entirely hexagonal (2H, in polytype formalism), but there are also numerous examples of three structures in which the packing is partially hexagonal and partially cubic. With increasing pressure, these tend to transform into structures in which there is an increasing fraction of cubic packing.<sup>35, 36</sup>

According to the literature on  $\text{ABC}_3$  compounds, all the atmospheric pressure forms definitely identified have either the perovskite or 2H structure except for  $\text{CsCdCl}_3$ ,<sup>41</sup> which has the 6H structure in which two-thirds of the layers are cubic-close-packed (stacking sequence cchcch). However, examination of the data<sup>42</sup> for  $\text{CsMnCl}_3$  and  $\text{RbMnCl}_3$  indicated that the cell dimensions are not consistent with either entirely cubic or entirely hexagonal close packing. We have determined the atmospheric pressure structures of these two compounds and have investigated the effect of pressure on their structures and on the structure of  $\text{RbFeCl}_3$ , which is 2H at atmospheric pressure.<sup>43</sup>

Samples of  $\text{CsMnCl}_3$  were prepared by the reaction of stoichiometric quantities of  $\text{CsCl}$  and  $\text{MnCl}_2 \cdot 4\text{H}_2\text{O}$  in a stream of titanium-scrubbed  $\text{N}_2$ . The reactants were slowly heated to  $200^\circ\text{C}$  and held there a few hours to remove all the water of hydration, after which the temperature was raised to  $500^\circ\text{C}$  for a few more hours. The same procedure was used to prepare  $\text{RbMnCl}_3$  and  $\text{RbFeCl}_3$  from the appropriate reactants. The two Mn compounds are pink and the Fe compound brown. None is noticeably hygroscopic.

The X-ray diffraction data for the  $\text{CsMnCl}_3$  phase stable at atmospheric pressure, which are in good agreement with the published values,<sup>42</sup> show that this phase has the rhombohedral 9R structure, in which one-third of the layers are cubic-close-packed (stacking sequence chhhchhh). Table II-5 compares the observed intensities and those calculated by assuming ideal close-packed positions for all the atoms in the 9R structure and an overall temperature factor of 1.5. The agreement is good, which indicates that a detailed refinement would reveal the deviations from the ideal atom positions to be small, as they are for the 9R forms of  $\text{CsCoF}_3$  (Ref. 37) and  $\text{BaRuO}_3$  (Ref. 44).

The effect of pressure on the  $\text{CsMnCl}_3$  structure was determined by the same method used in previous investigations.<sup>36</sup> In a typical run, a gold encapsulated specimen was subjected to the desired pressure in a belt apparatus and then heated to the desired temperature by means of an internal graphite heater. After half an hour at this temperature, the sample was quenched to room temperature before the pressure was released. X-ray diffraction measurements were then made at atmospheric pressure on the quenched sample.

When pressure is applied to the 9R form of  $\text{CsMnCl}_3$ , it is transformed first to the 6H polytype and then to the perovskite form. Since the perovskite structure is entirely cubic, no further transformation can occur. The same progression is observed for  $\text{CsCoF}_3$ <sup>35</sup> and  $\text{BaRuO}_3$ .<sup>36</sup> The results of the high pressure experiments are summarized by the pressure-temperature phase diagram shown in Fig. II-20, which shows the stability range for each of the three polytypes. The

## Section II

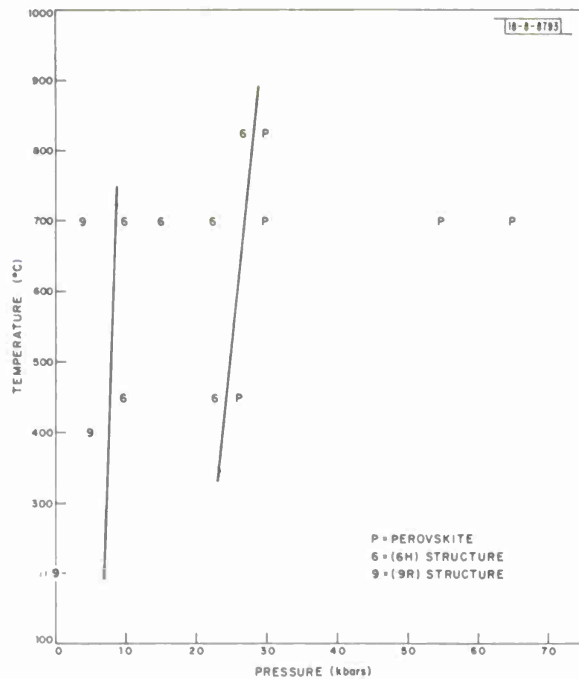


Fig. II-20. Pressure-temperature phase diagram for  $\text{CsMnCl}_3$ .

transformation pressures ( $\sim 10$  kbars for  $9\text{R} \rightleftharpoons 6\text{H}$ ,  $\sim 25$  kbars for  $6\text{H} \rightleftharpoons$  perovskite), like those for all other high pressure transformations of  $\text{CsBF}_3$  compounds, are not very sensitive to temperature.

Table II-6 compares the observed X-ray intensities for the 6H polytype of  $\text{CsMnCl}_3$  with those calculated by assuming ideal close-packed positions for all atoms and an overall temperature factor of 1.0. Some of the discrepancies between observed and calculated values are outside experimental error, indicating that the positions of some of the atoms are significantly different from the ideal ones. Structure refinements for other 6H polytypes, including those of  $\text{RbNiF}_3$  (Refs. 37 and 40) and  $\text{CsCdCl}_3$  (Ref. 41) have revealed significant distortions from the ideal positions.

Table II-7 gives the X-ray results for the perovskite form of  $\text{CsMnCl}_3$ . In this case there is good agreement between the observed intensities and those calculated by assuming ideal atom positions and an overall temperature factor of 1.5.

Both high pressure forms of  $\text{CsMnCl}_3$  are moderately stable at atmospheric pressure. There was no evidence of retransformation to the 9R structure after annealing in  $\text{N}_2$  for 3 days at  $200^\circ\text{C}$ , but complete retransformation occurred after only a few hours at  $300^\circ\text{C}$ . These retransformation temperatures are similar to those found for  $\text{CsBF}_3$  high pressure polytypes, which retransform between  $200^\circ$  and  $500^\circ\text{C}$ . This is in contrast to the more stable high pressure  $\text{ABO}_3$  polytypes, some of which retransform slowly even at  $1100^\circ\text{C}$ .

The x-ray data for the form of  $\text{RbMnCl}_3$  stable at atmospheric pressure, which are in good agreement with the published values,<sup>42</sup> show that this phase has the 6H structure. The x-ray pattern is very similar to the one given in Table II-6 for the high-pressure 6H polytype of  $\text{CsMnCl}_3$ . At  $700^\circ\text{C}$ , the 6H form of  $\text{RbMnCl}_3$  is transformed to the perovskite structure when the pressure exceeds 7 kbars. Table II-7 shows that the observed x-ray intensities are in good agreement with those calculated by assuming the ideal perovskite atom positions and an overall

TABLE II-6  
X-RAY DATA FOR HIGH PRESSURE  $\text{CsMnCl}_3$ (6H)

$a = 7.268(5) \text{ \AA}$ ,  $c = 17.85(5) \text{ \AA}$

$hkl$	$I_{\text{calc}}$	$I_{\text{obs}}$	$d_{\text{obs}}$	$hkl$	$I_{\text{calc}}$	$I_{\text{obs}}$	$d_{\text{obs}}$
1 0 2	1.6	4	5.12	3 0 3 2 1 5	0.1 1.0	26	1.984
0 0 4	1.1	2	4.43	2 0 7	25.0		
1 0 3	30.8	33	4.30	3 0 4 1 1 8	1.2 7.9	8	1.898
1 1 0	100.0						
1 0 4	72.6	175	3.48	2 2 0 2 0 8	54.1 17.0	75	1.819
1 1 2	2.3	—	—	2 1 7	18.8	15	1.743
2 0 1	14.4						
1 0 5	1.3	17	3.10	2 2 4 3 1 3	0.5 5.0	15	1.679
2 0 2	42.3						
0 0 6	27.2	70	2.961	2 0 9	10.4		
1 1 4	3.9	—	—	3 1 4 2 1 8	14.4 2.4	15	1.625
2 0 3	86.7	90	2.778	4 0 1 3 1 5	1.6 0.4	6	1.569
2 0 4	94.9	90	2.566	1 0 11	5.7		
2 1 1	0.3						
2 0 5	12.5						
1 0 7	24.0	32	2.360	4 0 2 2 2 6 2 0 10	5.1 19.5 8.2	22	1.552
2 1 2	0.4						
1 1 6	1.2	4	2.297	3 0 8	3.8	5	1.527
0 0 8	1.4	—	—	4 0 3 2 1 9	11.9 1.0	15	1.522
2 1 3	12.9	12	2.209	4 0 4 0 0 12	15.3 5.4	18	1.487
3 0 0	22.7						
2 1 4	31.1						
1 0 8	3.1	58	2.099				

## Section II

TABLE II-7  
X-RAY DATA FOR THE HIGH PRESSURE PEROVSKITE FORMS OF  $\text{CsMnCl}_3$  AND  $\text{RbMnCl}_3$

hkl	$\text{CsMnCl}_3$ ( $a = 5.111(3)$ Å)			$\text{RbMnCl}_3$ ( $a = 5.058(3)$ Å)		
	$I_{\text{calc}}$	$I_{\text{obs}}$	$d_{\text{obs}}$	$I_{\text{calc}}$	$I_{\text{obs}}$	$d_{\text{obs}}$
1 0 0	6	8	5.11	1.4	1	5.05
1 1 0	100	100	3.62	84	85	3.57
1 1 1	65	61	2.95	66	70	2.915
2 0 0	81	82	2.55	100	100	2.526
2 1 0	4	4	2.285	0.4	0	—
2 1 1	44	44	2.087	37	40	2.067
2 2 0	51	47	1.805	62	55	1.791
3 0 0	0.4	2	1.705	0.0	0	—
2 2 1	1.6			0.1		
3 1 0	18	19	1.616	15	16	1.595
3 1 1	22	22	1.541	21	16	1.520
2 2 2	16	16	1.475	19	16	1.457
3 2 0	0.9	0	—	0.0	0	—
3 2 1	20	18	1.366	16	14	1.350
4 0 0	7	8	1.278	8	9	1.262
4 1 0	0.6	0	—	0.0	0	—
3 2 2	0.6			0.0		
4 1 1	6	9	1.205	5	8	1.193
3 3 0	3			2		
3 3 1	8	8	1.172	8	7	1.159
4 2 0	18	16	1.143	21	16	—
4 2 1	0.9	1	1.117	0.0	0	—
3 3 2	4	4	1.090	3	2	—
4 2 2	13	10	1.044	16	10	—
5 0 0	0.1	0	—	0.0	0	—
4 3 0	0.4			0.0		
5 1 0	3	9	1.003	2	5	—
4 3 1	6			5		
5 1 1	5	5	0.983	5	2	—
3 3 3	1			2		

temperature factor of 1.5. The diffraction pattern is seen to be very similar to the one given in Table II-7 for the perovskite form of  $\text{CsMnCl}_3$ . At atmospheric pressure the perovskite form of  $\text{RbMnCl}_3$  retransforms to the 6H structure when annealed for a few hours at  $400^\circ\text{C}$ .

The stable form of  $\text{RbFeCl}_3$  at atmospheric pressure has the 2H structure,<sup>43</sup> and should have high pressure polytypes. The results of high pressure studies at  $700^\circ\text{C}$  are summarized in Table II-8. No single-phase pattern could be obtained for the 9R structure due to its very narrow stability range. The transformation pressures are not sensitive to temperature between  $400^\circ$  and  $700^\circ\text{C}$ .

Preliminary results show that when the atmospheric pressure forms of the materials discussed above are prepared in  $\text{HCl}$  and not  $\text{N}_2$ , they are very hygroscopic. There is no change in their x-ray patterns and in the  $\text{AMnCl}_3$  compounds, there is no change in any of the transformation pressures. For  $\text{RbFeCl}_3$ , however, all the transformation pressures are lowered by about 10 kbar and the  $6\text{H} \rightarrow 3\text{C}$  transformation cannot be retained by quenching to room temperature. We think now that use of  $\text{N}_2$  gas during preparation leads to nitride ions replacing chloride ions. The extent of replacement is probably very small in the Mn compounds but larger in  $\text{RbFeCl}_3$  with its easily oxidized  $\text{Fe}^{2+}$  ion.

TABLE II-8 CRYSTALLOGRAPHIC DATA FOR THREE $\text{ABC}_3$ COMPOUNDS			
Structure	Stability Range (kbars)	Cell Dimensions ( $\text{\AA}$ )	Volume ( $\text{\AA}^3$ ) per Formula Unit
$\text{CsMnCl}_3$			
9R	Atmospheric to 10	$7.288 \times 27.44$ (Ref. 42)	137.9
6H	10 to 25	$7.268 \times 17.85$	136.1
Perovskite	Above 25	5.115	133.8
$\text{RbMnCl}_3$			
6H	Atmospheric to $\sim 7$	$7.164 \times 17.798$ (Ref. 42)	131.8
Perovskite	Above 7	5.058	129.4
$\text{RbFeCl}_3$			
2H	Atmospheric to 25	$7.060 \times 6.020$ (Ref. 43)	129.9
9R	25 to 30	$7.050 \times 26.2$	125.3
6H	30 to 45	$7.04 \times 17.33$	124.0
Perovskite	Above 45	4.965	122.4

For all three  $\text{ABC}_3$  compounds investigated, the proportion of cubic packing in the high pressure polytypes increases with increasing pressure. The crystallographic data for all the polytypes of these compounds are summarized in Table II-8.

J. A. Kafalas  
J. M. Longo  
D. A. Batson

## Section II

### K. VOLUME COMPRESSION OF $\text{TiO}_x$

Titanium monoxide,  $\text{TiO}_x$ , has a cubic rock salt structure which is stable over an unusually wide range ( $0.75 < x < 1.30$  at  $1300^\circ\text{C}$ ) and has an unusually high vacancy content (up to 16 percent of the ideal lattice sites). As  $x$  increases from 0.75 to 1.30, the percentage of vacant oxygen sites decreases from 24 percent to 0 and the percentage of vacant metal sites increases from 8 to 24 percent. Thus the total number of vacancies decreases from 16 to 12 percent with increasing oxygen content. Even for the stoichiometric composition  $\text{TiO}_{1.0}$ , 15 percent of both metal and oxygen sites are vacant.<sup>45</sup> Some of the vacancies can be removed by annealing  $\text{TiO}_x$  at pressures from 50 to 100 kbars and temperatures of  $1100^\circ$  to  $1600^\circ\text{C}$ .<sup>46,47</sup> Because of the large and variable number of vacancies, some of which can be removed by pressure anneal,  $\text{TiO}_x$  might be expected to have a substantial and composition-dependent volume compression.

We are studying the volume compression of  $\text{TiO}_x$  at various values of  $x$  by using several diamond anvil high pressure x-ray units<sup>48</sup> to measure the lattice parameter as a function of pressure. Two of these units are gas loaded, a third has screw loaded flat springs and the fourth has direct screw loading. The internal pressure is determined by observing the decrease in lattice parameter of  $\text{NaCl}$  which is mixed with the  $\text{TiO}_x$ . The pressure value is obtained from the tabulated results<sup>49</sup> of pressure-volume calculations for  $\text{NaCl}$  made using equations of state and the elastic constants at one atmosphere. Some of the problems associated with this type of experiment are described in a recent review.<sup>48</sup>

A sample of -100 mesh  $\text{TiO}_x$  is mixed with dry -200 mesh  $\text{NaCl}$  in the ratio  $2\text{TiO}_x : 1\text{NaCl}$ , and the mix is prepressed into a wafer  $\sim 0.005$  to  $0.010$  inch thick. Small pieces of the wafer are glued to the fixed or "anvil" diamond of the squeezer. An atmospheric pressure reference pattern is made on a portion of the wafer by the standard Debye-Scherrer technique, and the lattice constants of both compounds are determined by using a modified Cohen extrapolation. An atmospheric pressure pattern is also attempted in the diamond-anvil squeezer. However, it is not possible to know when the diamonds are just touching the wafer so that the first film may be made at a pressure of 0.5 to 5 kbars. A series of patterns is then made at increasing loads,

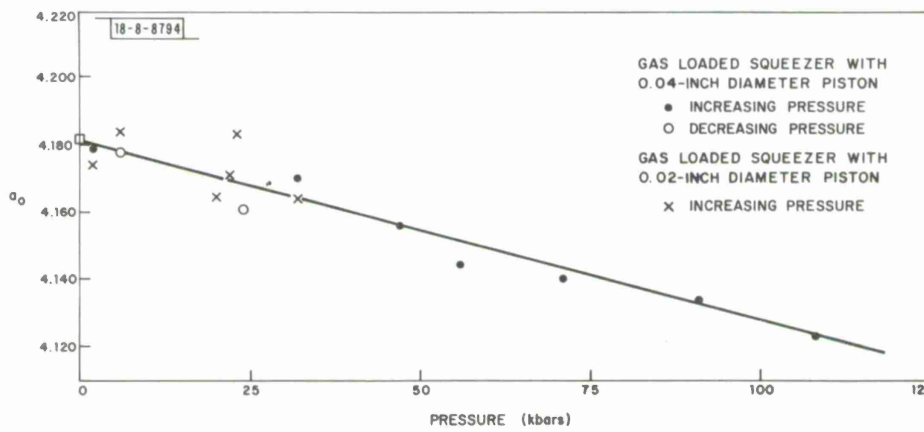


Fig. II-21. Lattice parameter of  $\text{TiO}_{1.0}$  as a function of pressure.

estimated to give 5 to 20 kbars pressure increments, until the working limit of the unit is reached (100 to 150 kbars) or until there is evidence of a failure in the sample or diamonds. If a series is completed without a failure, a final pattern is made with all the load removed to check that the fixed diamond has not moved in relation to the film during the pressure cycle.

The x-ray films for samples under pressure require exposures of 100 to 400 hours to Zr-filtered Mo radiation from a Norelco fine focus x-ray tube, or exposures of 15 to 40 hours to radiation from a Jarrell-Ash microfocus unit (used through the courtesy of the Jarrell-Ash Co.). The better films give four to six diffraction lines for each compound and the best films, which are obtained in the Bassett<sup>50</sup> screw loaded squeezer, have seven or eight lines for each with  $2\theta$  as high as  $44^\circ$ . For each compound a separate lattice parameter value is calculated from the d-value of each line. The lattice constant adopted is usually the numerical average of all the individual values. However, on occasion one or more low angle lines may appear grossly inconsistent and are not used.

Data for a typical series of measurements are shown in Fig. II-21, where the lattice constant of  $\text{TiO}_{1.0}$  is plotted vs pressure up to 108 kbars. This series was made in two different gas loaded squeezers using portions of the same  $\text{TiO}_{1.0}$ -NaCl mix. The values of volume compression ( $\Delta V/V_0 \Delta p$ ) for this and the other compositions studied are listed in Table II-9. Each value is based on the best straight line obtained by a visual fit to all the data points for that composition as shown in Fig. II-21, even though in some cases an individual run could be better described by a curve indicating a decrease in compression at higher pressures. The differences among the tabulated values, which range from  $2.6 \times 10^{-4}$  to  $4.0 \times 10^{-4} \text{ kbar}^{-1}$ , are probably not significant in view of the experimental errors.

TABLE II-9 VOLUME COMPRESSION OF $\text{TiO}_x$			
x	Pressure Range (kbars)	No. of Runs	$\frac{-\Delta V}{V_0 \Delta p}$ ( $\text{kbar}^{-1}$ )
0.83	0-124	2	$3.3 \times 10^{-4}$
0.85	0-39	3	$2.3 \times 10^{-4}$
1.00	0-108	2	$3.8 \times 10^{-4}$
1.10	0-139	1	$2.6 \times 10^{-4}$
1.25	0-52.5	1	$4.0 \times 10^{-4}$

There are two other reports of volume compression measurements on  $\text{TiO}_x$ , both carried out with tetrahedral-anvil pressure units, which generate nearly hydrostatic pressure. Taylor and Doyle<sup>51</sup> report a value of  $5.5(8) \times 10^{-4} \text{ kbar}^{-1}$  for  $\text{TiO}_{1.0}$  (with 15 percent vacancies) without giving any experimental details. Iwasaki, *et al.*,<sup>52</sup> measured the lattice parameter for

## Section II

$\text{TiO}_{1.25}$  to 60 kbars using  $\text{NH}_4\text{Cl}$  as a pressure marker. They give a compression value of  $8.6 \times 10^{-4} \text{ kbar}^{-1}$  based on their data above 10 kbars. (Between 1 atmosphere and 10 kbars they observed a slight increase in lattice parameter, but this is such an improbable result that all possible sources of experimental error must be eliminated before it can be accepted. Iwasaki, et al.,<sup>52</sup> do not report the diffraction lines they observed or give any analysis of errors.)

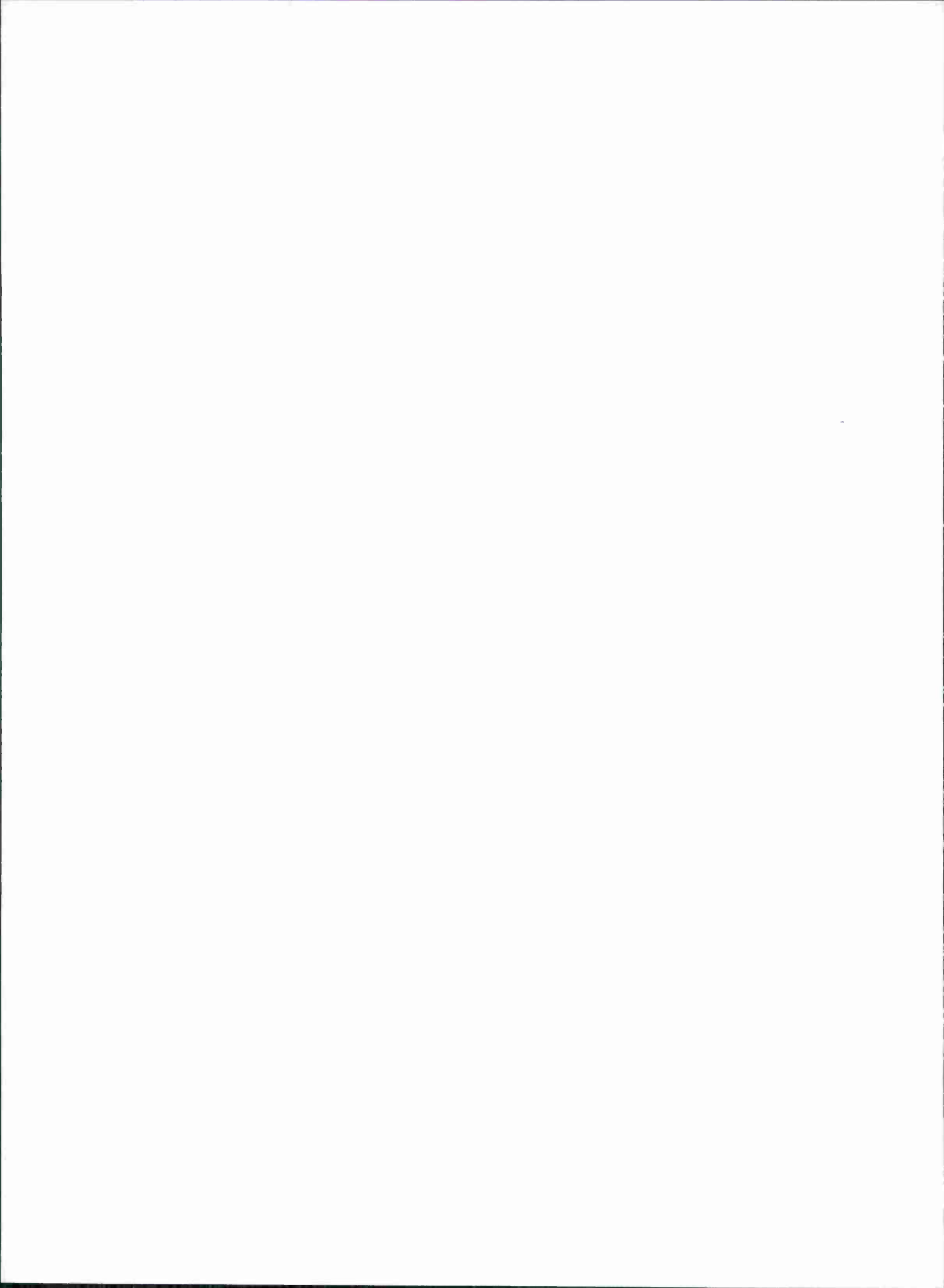
Although the quantitative values from the three investigations of  $\text{TiO}_x$  are somewhat different, it is clear that in spite of the large number of vacancies the volume compression of  $\text{TiO}_x$  is very small and not markedly dependent on the type or number of vacancies. In fact, its compression is close to those for  $\text{TiC}$  and  $\text{TiN}$  and of the same order as those for monoxides such as  $\text{MnO}$  and  $\text{CoO}$  which have very few vacancies.

M. D. Banus  
Mary C. Lavine

## REFERENCES

1. T.B. Reed and E.R. Pollard, J. Cryst. Growth 2, 243 (1968), DDC AD-681586.
2. G.M. Grover, T.P. Cotter and G.F. Erikson, J. Appl. Phys. 35, 1990 (1964).
3. G.Y. Eastman, Sci. Amer. 218, 28 (1968).
4. F.P. Koffyberg, Phys. Letters A30, 37 (1969) and private communication.
5. M. Altwein, H. Finkenrath, C. Konak, J. Stuke and G. Zimmerer, Phys. Stat. Solidi 29, 203 (1968).
6. S. Hayashi, Oyo Butsuri 34, 825 (1965).
7. P. Höschl, C. Konak, and V. Prosser, Mat. Res. Bull. 4, 87 (1969).
8. Solid State Research Report, Lincoln Laboratory, M.I.T. (1969:3), p. 15, DDC AD-696620.
9. Solid State Research Report, Lincoln Laboratory, M.I.T. (1969:4), p. 8, DDC AD-701022.
10. R. Hultgren, R.L. Orr, P.D. Anderson and K.K. Kelley, Supplement to Selected Values of Thermodynamic Properties of Metals and Alloys (Wiley, New York, 1963).
11. J.M. Haschke and H.A. Eick, J. Phys. Chem. 73, 374 (1969).
12. C.E. Holley, E.J. Huber and F.B. Baker in Progress in the Science and Technology of the Rare Earths 3, edited by L. Eyring (Pergamon Press, Oxford, 1968), p. 343.
13. S. Larach, R.E. Shrader and C.F. Stocker, Phys. Rev. 108, 587 (1957).
14. R.E. Halsted, D.T.F. Marple and M. Aven, Extended Abstracts, Electronics Div., Electrochem. Soc. 14, 6 (1965).
15. A.C. Aten, J. Phys. Chem. Solids 28, 1340 (1967).
16. G.W. Iseler and A.J. Strauss, J. Luminescence 3, 1 (1970).
17. M. Cardona, K.L. Shaklee and F.H. Pollak, Phys. Rev. 154, 696 (1967).
18. A.G. Thompson and J.C. Woolley, Canad. J. Phys. 45, 255 (1967).
19. J.A. Van Vechten and T.K. Bergstresser, Bull. Am. Phys. Soc. 15, 254 (1970).
20. L.R. Shiozawa and J.M. Jost, "Research on II-VI Compound Semiconductors," Clevite Corporation Electronic Research Division, Cleveland, Ohio (May 1965), p. 118, DDC AD-620297.

21. Solid State Research Report, Lincoln Laboratory, M.I.T. (1969:3), p. 21, DDC AD-696620.
22. J. Steininger, Mat. Res. Bull. 3, 595 (1968), DDC AD-674790.
23. D.T.F. Marple, Phys. Rev. 150, 728 (1966).
24. O. Brafman and I.T. Steinberger, Phys. Rev. 143, 501 (1966).
25. L.V. Prytkina, V.V.V. Volko, A.J. Mentser, A.V. Vanyukov and P.S. Kireev, Sov. Phys. - Semicon. 2, 509 (1968).
26. D.B. Rogers, R.J. Arnott, A. Wold and J.B. Goodenough, J. Phys. Chem. Solids 24, 347 (1963).
27. D.B. Rogers, J.L. Gillson and J.E. Gier, Solid State Comm. 5, 263 (1967).
28. B. Reuter and K. Müller, Naturwiss. 7, 164 (1967).
29. J. Jaskowsky, Ber. Bunsengesell. Phys. Chem. 70, 199 (1966).
30. J.B. Goodenough, J. Solid State Chem. 1 (in press).
31. W. Rüdorff, J. Kändler and D. Babel, Z. anorg. allgem. Chem. 317, 261 (1962).
32. R.D. Burbank and H.T. Evans, Acta Cryst. 1, 330 (1948).
33. J.A. Kafalas and J.M. Longo, Mat. Res. Bull. 3, 501 (1968), DDC AD-674785.
34. Y. Syono, S. Akimoto and K. Kohn, J. Phys. Soc. Japan 26, 993 (1969).
35. J.M. Longo and J.A. Kafalas, J. Solid State Chem. 1, 103 (1969), DDC AD-693900.
36. \_\_\_\_\_, Mat. Res. Bull. 3, 687 (1968), DDC AD-674791.
37. D. Babel, Z. anorg. allgem. Chem. 369, 117 (1969).
38. Z. Zalkin, K. Lee and D. Templeton, J. Chem. Phys. 37, 697 (1962).
39. G.A. Smolenskii, M.P. Petrov, V.V. Moskalev, V.S. L'vov, V.S. Kasperovich and E.V. Zhirnova, Sov. Phys. Solid State 10, 1040 (1968).
40. R.J. Arnott and J.M. Longo, J. Solid State Chem. (in press).
41. S. Siegel and E. Gebert, Acta Cryst. 17, 790 (1964).
42. M. Kestigian, W.J. Croft and F.D. Leipziger, J. Chem. Eng. Data 12, 97 (1967).
43. H.J. Seifert and K. Klatyk, Z. anorg. allgem. Chem. 342, 1 (1966).
44. P.C. Donohue, L. Katz and R. Ward, Inorg. Chem. 4, 306 (1965).
45. M.D. Banus and T.B. Reed, Chemistry of Extended Defects in Non-Metallic Solids, edited by L. Eyring and M. O'Keefe. (North-Holland, Amsterdam, 1970), p. 488.
46. M.D. Banus, Mat. Res. Bull. 3, 723 (1968), DDC AD-677839.
47. N.J. Doyle, J.K. Hulm, C.K. Jones, R.C. Miller and A. Taylor, Phys. Letters 26A, 604 (1968).
48. M.D. Banus, High Temperatures - High Pressures 1, No. 5 (in press).
49. D.L. Decker, W.A. Bassett, L. Merrill, H.T. Hall and J.D. Barnett, "High Pressure Calibration - A Critical Review," High Pressure Data Center, Brigham Young University, (October, 1969).
50. W.A. Bassett, T. Takahashi and P.W. Stook, Rev. Sci. Instr. 38, 37 (1967).
51. A. Taylor and N.J. Doyle, Chemistry of Extended Defects in Non-Metallic Solids, edited by L. Eyring and M. O'Keefe (North-Holland, Amsterdam, 1970), p. 523.
52. H. Iwasaki, K. Kamigaki, S. Ogawa, O. Terasaki and D. Watanabe, J. Phys. Soc. Japan (in press).



### III. PHYSICS OF SOLIDS

#### A. ELECTRONIC BAND STRUCTURE

##### 1. Fermi Surface and Optical Properties of Potassium

We have carried out a new calculation of the interband absorption of potassium. Until now the optical constants have been calculated using a local pseudopotential<sup>1</sup> model. However, it has been demonstrated<sup>2</sup> that the local pseudopotential formulation is inadequate to account for the experimentally measured Fermi surface of potassium. It has been shown<sup>3</sup> that the pseudopotential that appears in the optical matrix element will incorporate the effects of many-body correlations only if it is consistent with the experimental data of Fermi surface measurements (such as dHvA results). The two nonlocal pseudopotentials used here were selected with this requirement in mind.

One of the nonlocal pseudopotentials  $V_{\vec{k}}(\vec{G} - \vec{G}')$  used (where  $\vec{G}$  is a reciprocal lattice vector and  $\vec{k}$  the electron momentum) is a simple generalization of the local pseudopotential, consistent with bcc symmetry. It is parameterized phenomenologically by constants characterizing its local and nonlocal ( $\vec{k} \cdot \vec{G}$ -dependent) features. The other potential  $\langle \vec{k} + \vec{G} | \Gamma | \vec{k} + \vec{G}' \rangle$  is the Ziman<sup>4</sup> form of the KKR method in which the wavefunction external to the muffin-tin radius  $R_s$  is expressed as plane-waves. It is parameterized by s-, p-, and d-phase shifts.  $R_s$  was taken to be the atomic core radius.

Each potential, when inserted into a  $19 \times 19$  determinant and solved for the energy eigenvalues, gave an excellent fit (Fig. III-1) to the experimental Fermi surface. The KKR-Z result indicated that the d-phase shift was particularly important – which is probably the reason for the nonlocality required of any pseudopotential used in the case of potassium. It is of interest that each potential was weaker than the Ashcroft<sup>5</sup> local pseudopotential and the electronic states are thus more free-electron-like.

While permitting a good fit to the Fermi surface, nonlocal pseudopotentials suffer a disadvantage over local potentials when it comes to calculating properties dependent on the wavefunctions. In general, the wavefunctions are no longer expressed in terms of plane waves. However, the Ziman form of the KKR method is constructed so that the eigenfunctions are expressible simply as plane waves outside  $R_s$ . In the case of  $V_{\vec{k}}(\vec{G} - \vec{G}')$ , this is not necessarily true.

The optical conductivity  $\sigma(\omega)$  was calculated by solving the  $19 \times 19$  determinant at different points in the Brillouin zone as required by the Monte Carlo integration scheme used. With either nonlocal pseudopotential, the interband threshold occurs at about 1.3 eV and the absorption maximum at about 2 eV (Fig. III-2). The absorption magnitude depends on the potential, however  $\text{Re } \sigma(2 \text{ eV}) \sim 1.8 \times 10^{13} \text{ sec}^{-1}$  with the potential  $V$ , and five times smaller with the KKR-Z potential. The former result is closer to the measurements of Smith.<sup>6</sup> The source of the discrepancy seems most likely to occur in the KKR-Z calculation on account of the approximations made in the calculation – namely, neglect of the energy dependence of the pseudopotentials and truncation of the eigenfunctions to 19 plane waves. Consideration of these features should be included in further calculations.

A. R. Wilson  
C. Y. Young  
G. F. Dresselhaus

### Section III

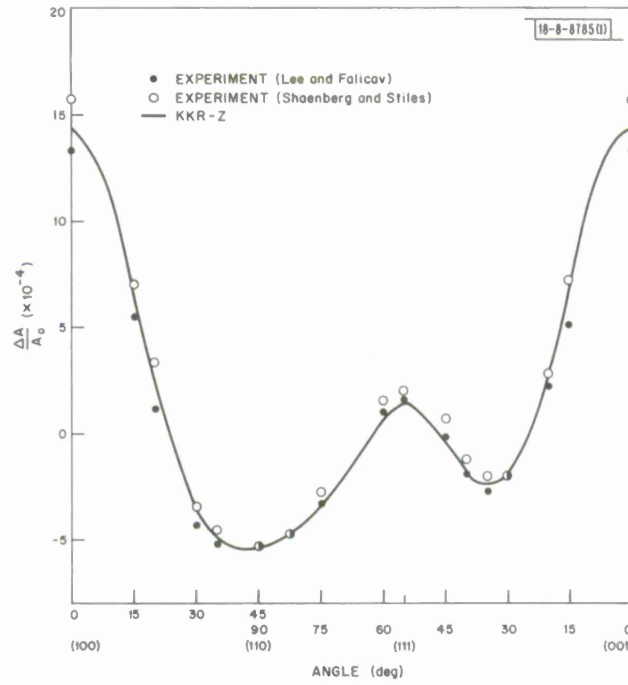


Fig. III-1. Best fit to experimental fractional change  $\Delta A/A$  of central cross sectional area with direction.

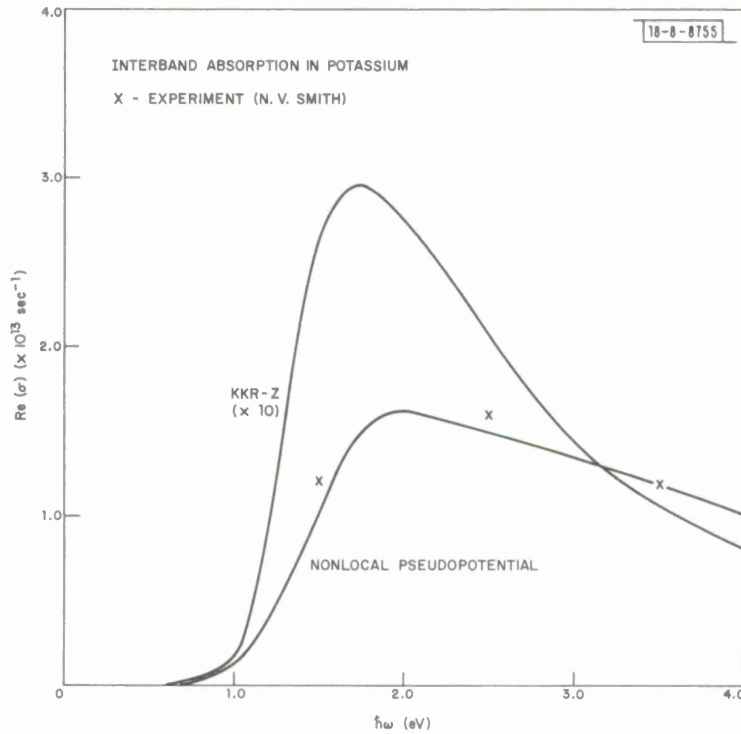


Fig. III-2. Interband absorption,  $\text{Re } \sigma(\omega)$ , for the two pseudopotentials used and the experimental point of N.V. Smith (Ref.6).

## 2. Model of the Insulator-Metal Transition in $Ti_2O_3$

In an attempt to understand the nature of the insulator-metal transition in  $Ti_2O_3$  (Ref. 7), we have explored a model based on the competition between elastic and electronic free energies of the system as a function of temperature. The model consists of two bands, one filled and one empty at  $T = 0^{\circ}K$ , separated by an energy gap which depends linearly on a lattice distortion parameter. The normalized free energy of the system is written,

$$F = \delta^2 - \kappa \left\{ kT \int \ln [1 + e^{-(\epsilon-\mu)/kT}] \rho_e(\epsilon) d\epsilon + kT \int \ln [1 + e^{-(\epsilon+\mu+[1-\delta])/kT}] \rho_h(\epsilon) d\epsilon \right\} \quad (III-1)$$

In Eq. (III-1),  $\delta$  is a normalized variable, proportional to the change in lattice distortion parameter at  $T = 0^{\circ}K$ . The first term is the lattice distortion free energy, the second is the free energy due to the excitation of electrons into the empty band, and the third term is the free energy of the holes excited in the filled band (see Fig. III-3).  $\epsilon$  is a normalized energy variable,  $\mu$ , the normalized Fermi energy, and  $[1 - \delta]$ , the normalized energy gap. All energies and  $kT$  have been normalized to the energy gap at  $T = 0^{\circ}K$ .  $\rho_e(\epsilon)$  and  $\rho_h(\epsilon)$  are the densities of states for the bands which are empty and filled, respectively, at  $T = 0^{\circ}K$ .  $\kappa$  is a dimensionless parameter which determines the relative scale of the lattice distortion and electronic free energies.

With this expression for the free energy, both  $\delta$  and  $\mu$  can be determined at any temperature by the conditions that  $\partial F / \partial \delta = 0$ ; and the number of electrons equals the number of holes.

Such a model is capable of giving a reasonable description of the change in c/a ratio in  $Ti_2O_3$  as a function of temperature. As an example, we show in Fig. III-4 the results of a computer calculation of  $\delta$  vs  $kT$ .

The same model should also describe the behavior of a Raman mode frequency associated with the displacement  $\delta$ , as a function of temperature, through the relation,  $\omega_{Raman} \propto \sqrt{d^2 F / d\delta^2}$ . A plot of  $d^2 F / d\delta^2$ , shown in Fig. III-5, predicts a very pronounced "mode softening" in the vicinity of the transition, due to the strong coupling of the electronic and lattice distortion free energy needed to explain the sharp change in c/a ratio observed in  $Ti_2O_3$  in the transition region since the Raman frequencies observed in  $Ti_2O_3$  (Ref. 8) show only a slight softening, we can conclude that this model based on lattice distortion as the driving mechanism for the transition in  $Ti_2O_3$  is inconsistent with the Raman scattering data.

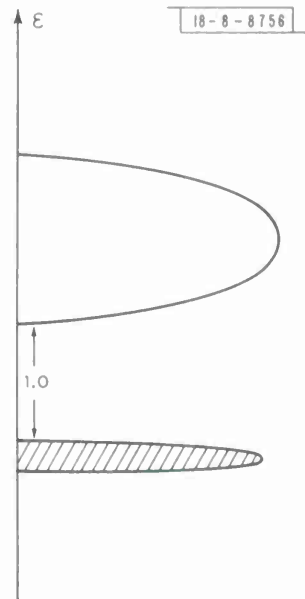


Fig. III-3. Schematic population of band model at  $T = 0^{\circ}K$ .

P. M. Raccah  
H. J. Zeiger

### Section III

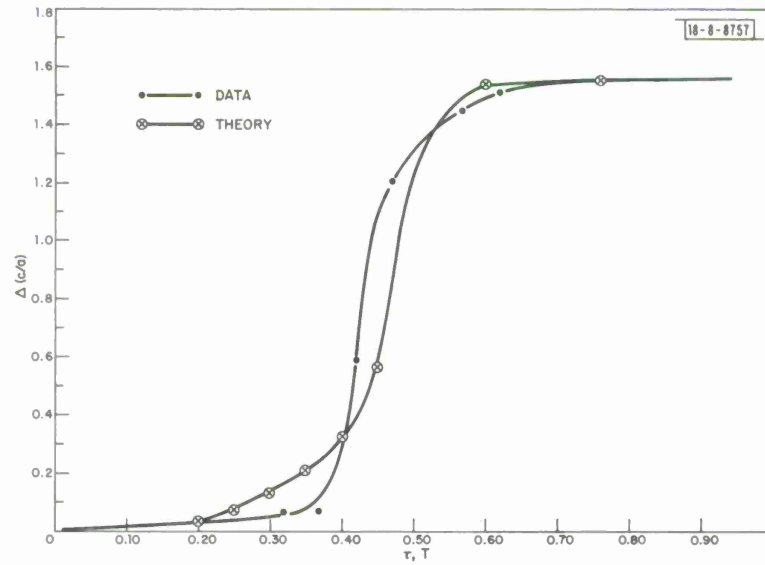


Fig. III-4. Theory curve shows  $\delta$  vs  $kT$  for normalized upper bandwidth = 5.0, lower bandwidth = 0.2 and  $k = 37$ . Data curve shows  $c/a$  behavior as function of temperature on same normalized scale.

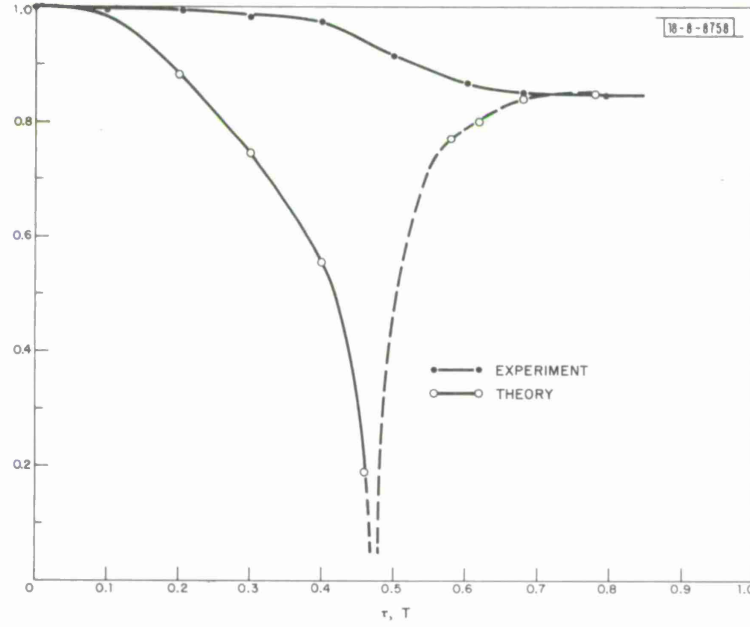
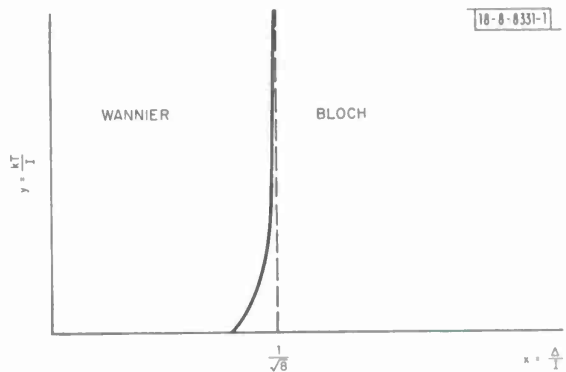


Fig. III-5. Comparison between experimental phonon frequencies and theoretical predictions.

### 3. Variational Approach to the Metal-Semiconductor Transition

A mechanism for a metal to semiconductor transition occurring with increasing temperature has been found in the context of a new variational approximation<sup>9</sup> to the half-filled band Hubbard Hamiltonian. We have found the stability boundary (based on minimum free energy) between the intuitively simple thermodynamic states representing localized (Wannier state) and band (Bloch state) behavior. This is shown in Fig. III-6, in which  $I$  is the Coulomb repulsion,  $\Delta$  is a measure of the bandwidth defined by  $\Delta^2 = \sum_j b_{ij}^2$  is the transfer integral between sites  $i$  and  $j$  and

Fig. III-6. Stability boundary between Wannier (localized) and Bloch (band) states.



$b_{ii} \equiv 0$ . While this boundary had previously been given<sup>10</sup> for a linear chain with nearest-neighbor  $b_{ij}$ , the present boundary was calculated using the density of states

$$\rho(\epsilon) = \frac{1}{\pi\Delta} \sqrt{1 - \left(\frac{\epsilon}{2\Delta}\right)^2} \quad |\epsilon| < 2\Delta$$

$$= 0 \quad |\epsilon| > 2\Delta \quad (\text{III-2})$$

which was used by Hubbard<sup>11</sup> in his investigation of an insulator-metal transition at  $T = 0^\circ\text{K}$ . Equation (III-2) is not unreasonable for a more realistic 3-dimensional band structure.

We make the following points.

- (a) The qualitative behavior is very similar to that for the linear chain,<sup>10</sup> and indeed can be understood in general terms as follows:

The fact that the low temperature slope is positive can be understood easily if we note that (1) the zero-temperature entropy is  $Nk \ln 2$  for the Wannier state and zero for the Bloch state and (2) the ground-state energy difference between the Bloch and Wannier states,  $E_B - E_W$ , decreases with increasing bandwidth. Thus at low  $T$ , the free energies

$$F_W = E_W - kT \ln 2 + \dots$$

$$F_B = E_B + O(T^2) \quad (\text{III-3})$$

so that on the boundary,  $kT \ln 2 = E_W - E_B$ . Hence on the boundary

$$\frac{\partial T}{\partial \Delta} = -\frac{1}{k \ln 2} \frac{\partial(E_B - E_W)}{\partial \Delta} > 0 \quad (\text{III-4})$$

### Section III

Also, the fact that the boundary asymptotes to a vertical line can be understood when it is considered that (1) as  $T \rightarrow \infty$  the entropy for the Wannier and the Bloch states are the same ( $Nk \ln 4$ ) and (2) the internal energies approach a constant independent of  $T$ . The equality of the entropies comes from the fact that for  $kT \gg U$ , polar states are highly probable in the Wannier state as well as in the Bloch state.

Clearly the positive slope implies a transition from band to localized behavior with increasing  $T$  for

$$\left(\frac{\Delta}{I}\right)_0 < \frac{\Delta}{I} < \frac{1}{\sqrt{8}} \quad (\text{III-5})$$

where  $(\Delta/I)_0$  is the zero-temperature intercept of the boundary.

- (b) The phase boundary obtained here is in qualitative disagreement with one presented by Mott<sup>12</sup> (the slope of his curve is negative). The reason for the difference is that Mott considered a transition from a magnetically-ordered insulating state to a paramagnetic metallic state whereas we have considered paramagnetic states on both sides of the transition. It seems to us that in a consistent treatment, one should consider magnetically ordered states on both sides of the transition at low temperatures, as we have done.<sup>10</sup> The present treatment is restricted to temperatures greater than any magnetic-ordering temperature.
- (c) We note that the zero-temperature intercept  $(\Delta/I)_0 = 0.295$ , is very close to the value 0.289 at which Hubbard<sup>11</sup> obtained a nonmagnetic insulator-metal transition at 0°K.

T. A. Kaplan  
R. A. Bari

#### 4. Interaction of Bound Electrons with Local and Resonant Modes in Semiconductors

It is suggested that some of the multiple pinning phenomena observed in the optical and infrared spectra of impurities and other imperfections in semiconductors<sup>13,14</sup> may be due to pinning to local or resonant modes. As a model problem, we have considered the optical absorption spectrum of an electron in an insulator bound to an impurity, interacting with the L-O branch of the lattice vibrational spectrum, as affected by the presence of the impurity. A Green's function calculation for the spectrum in the case of a local mode, gives a pinning effect due to interaction with the local mode in the vicinity of the impurity, as well as pinning due to the lattice modes. The nature of the pinning phenomena in the case of a resonant mode, and the criteria for the observation of such pinning, are being investigated.

R. W. Davies  
H. J. Zeiger

#### 5. Band Theory of Optical Activity

Optical activity arises from terms linear in  $\vec{q}$  in the wavevector- and frequency-dependent dielectric tensor,  $\epsilon(\vec{q}, \omega)$ . In crystals  $\epsilon(\vec{q}, \omega)$  is given compactly to all powers of  $\vec{q}$  (all multipole moments) using a Bloch state band formalism. The linear  $\vec{q}$  part of  $\epsilon$  is obtained by a first order  $\vec{q} \cdot \vec{p}$  perturbation expansion of either the band state's energy or wavefunction. For the uniaxial crystal classes,  $D_3$ ,  $D_4$ ,  $D_6$ ,  $C_3$ ,  $C_4$ ,  $C_6$ , the dielectric tensor component responsible for the optical activity for propagation parallel to the c-axis is

$$\epsilon_{xy}(q_z, \omega) = - \sum_{k\gamma\gamma'} \frac{4q_z(k\gamma' | p_z | k\gamma')}{m\omega_{\gamma'\gamma}} \epsilon'_o \left[ \frac{3\omega_{\gamma'\gamma}^2 - \omega^2}{\omega_{\gamma'\gamma}^2 - \omega^2} \right] \quad (\text{III-6a})$$

where

$$\epsilon'_o \doteq \frac{4\pi e^2 f_{k\gamma}}{m^2 \hbar \Omega} \frac{(k\gamma | p_x | k\gamma') (k\gamma' | p_y | k\gamma)}{\omega_{\gamma'\gamma} (\omega_{\gamma'\gamma}^2 - \omega^2)} \quad (\text{III-6b})$$

and for propagation in the basal plane

$$\epsilon_{yz}(q_z, \omega) = -i \sum 2q_x a [\epsilon''_e - \epsilon''_o] \quad (\text{III-7a})$$

where

$$a \doteq (k\gamma' | x | k\gamma'') = i(k\gamma' | p_x | k\gamma'') / m\omega_{\gamma'\gamma''} \quad (\text{III-7b})$$

$$\epsilon''_e \doteq \frac{4\pi e^2 f_{k\gamma}}{m^2 \hbar \Omega} \frac{(k\gamma | p_y | k\gamma') (k\gamma'' | p_z | k\gamma)}{\omega_{\gamma''\gamma} (\omega_{\gamma''\gamma}^2 - \omega^2)} \quad (\text{III-7c})$$

and  $\epsilon''_o$  is given by an expression similar to Eq. (III-7c) with  $\omega_{\gamma''\gamma} \rightarrow \omega_{\gamma'\gamma}$ . Here  $\hbar\omega_{\gamma'\gamma}$  is the energy difference between Bloch states  $|k\gamma'\rangle$  and  $|k\gamma\rangle$ ; and  $f_{k\gamma}$  is the Fermi distribution function,  $[\exp(E_{k\gamma} - E_f)/kT + 1]^{-1}$ . The rotary powers parallel and perpendicular to the c-axis are

$$\rho_{||} = -iq_z \epsilon_{xy} / 2\epsilon'_o^{1/2} \quad (\text{III-8a})$$

$$\rho_{\perp} = -iq_x \epsilon_{yz} / 2(\epsilon'_o \epsilon'_e)^{1/4} \quad (\text{III-8b})$$

where  $\epsilon'_o$  and  $\epsilon'_e$  are the ordinary and extraordinary  $q = 0$  dielectric constants. These expressions may be used to calculate the optical activity from a given band model or, conversely, to adjust the band parameters to fit the rotary power data.

The general results above take on a revealing form in a simple four-band model of  $D_3$  symmetry with a direct gap at the  $\Gamma$ -point. Here the filled band is assumed to have  $\Gamma_1$  symmetry and the conduction band, to consist of a  $\Gamma_2$  singlet (transforming as  $z$ ) and a  $\Gamma_3$  doublet (transforming as  $x, y$ ). Then  $\sum_k \epsilon'_k = \epsilon'_o$ ; and, if we also assume that  $(\Gamma_1 | p_y | \Gamma_3) \simeq (\Gamma_1 | p_z | \Gamma_2)$ ,  $\sum_k [\epsilon''_e - \epsilon''_o] = \epsilon'_e - \epsilon'_o$ . This latter "cubic" approximation is equivalent to attributing the total birefringence to the energy denominators and not to the matrix elements. The spatial matrix element,  $a$ , has an upper limit of the size of the unit cell. Thus the pairwise near-cancellation of two resonances, manifest in the birefringence, yields the correct order-of-magnitude of the optical activity. In the case of small birefringence, i.e.,  $|\omega_{\gamma''\gamma'}| \ll \omega_{\gamma'\gamma} \sim \omega_{\gamma''\gamma}$ , the anisotropy of the rotary power is

$$\frac{\rho_{||}}{\rho_{\perp}} \simeq -2 \frac{(\Gamma_3 | p_z | \Gamma_3)}{(\Gamma_2 | p_x | \Gamma_3)} \quad (\text{III-9})$$

Section III

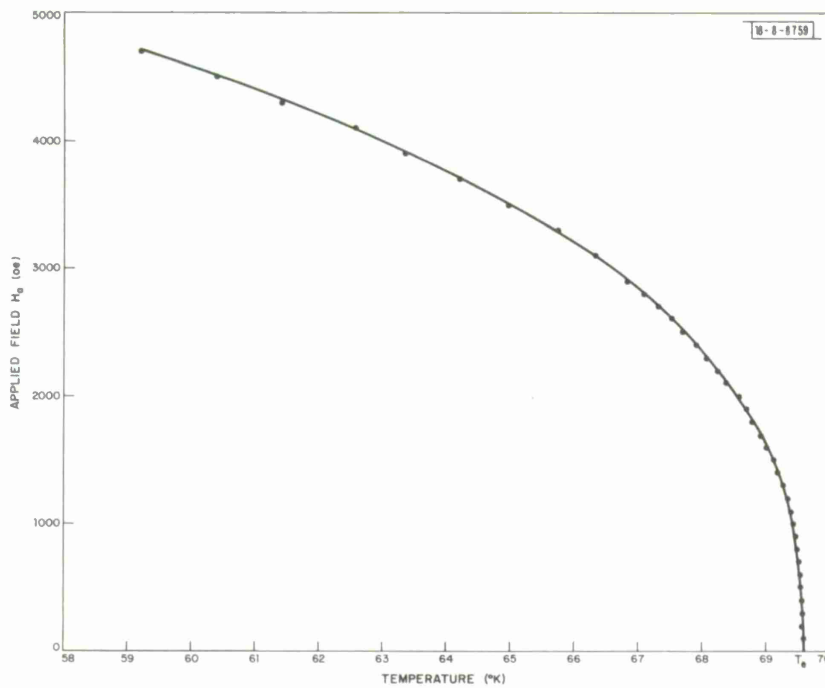


Fig. III-7(a). Temperature of kink in magnetization vs temperature curves of EuO as a function of applied field  $H_k$ .

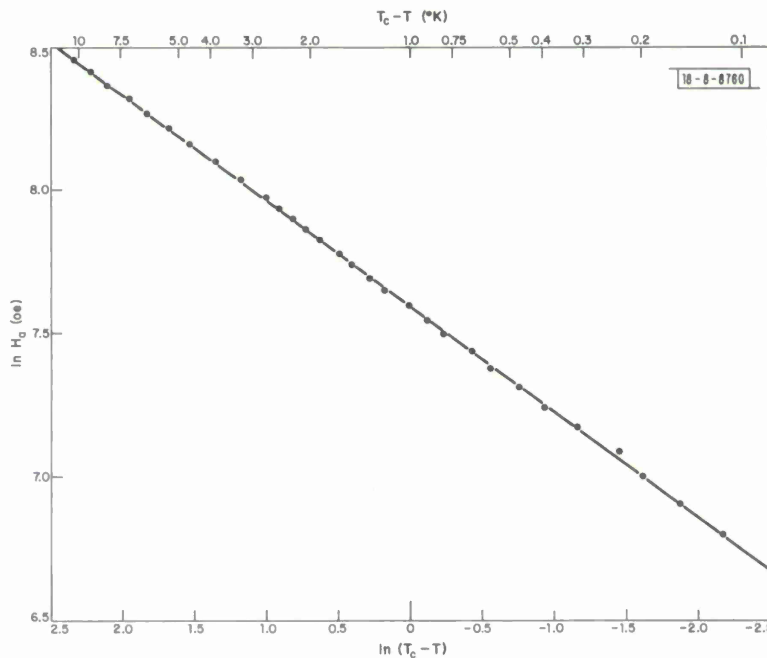


Fig. III-7(b). Deviation of kink temperature from  $T_c$  as a function of applied field. Slope corresponds to  $\beta = 0.368$ .

If the "cubic" approximation is again invoked, the matrix element ratio is  $\sim 1$  since  $\Gamma_2^+ \rightarrow T$  (triplet). Then  $\rho_{||}/\rho_{\perp} \sim -2$ , which is close to the measured ratio in  $\alpha$ -quartz.

A. S. Pine  
G. F. Dresselhaus

## B. MAGNETISM

### 1. Critical Magnetic Properties of EuO

A study is being made of the magnetic properties of single crystal EuO<sup>†</sup> in the vicinity of the Curie temperature. We have analyzed the measurements to determine the magnetic critical indices  $\beta$ ,  $\delta$  and  $\gamma$ , which are defined by the equations

$$\sigma \propto (T_c - T)^{\beta} \quad \text{for } T < T_c \quad (\text{III-9a})$$

$$H \propto \sigma^{\delta} \quad \text{for } T = T_c \quad (\text{III-9b})$$

$$\chi_o^{-1} \propto (T - T_c)^{\gamma} \quad \text{for } T > T_c \quad (\text{III-9c})$$

where  $\sigma$  represents the magnetic moment of the sample,  $H$  is the magnetic field internal to the sample (applied field minus demagnetization effects),  $\chi_o$  is the initial susceptibility and  $T_c$  is the Curie temperature.

The critical index  $\beta$  was determined by the method proposed by Rayl and Wojtowicz,<sup>15</sup> which utilizes the fact that there is a sharp kink in the magnetization vs temperature curve at the temperature where the applied field ( $H_a$ ) is equal to the demagnetizing field of the sample. At this point the applied field is proportional to the magnetization according to the relationship  $H_a = NM$ , where  $N$  is the demagnetizing factor ( $4\pi/3$  for a sphere). This kink was extremely sharp in our crystal, occurring over less than  $0.01^\circ\text{K}$ , indicating high sample homogeneity. The locus of kink points as a function of applied field is shown in Fig. III-7a. It is seen that extrapolation of this curve to  $H_a = 0$  gives an accurate measure of  $T_c$ . Replotting the points in Fig. III-7a on a log-log scale gives the linear relationship predicted by Eq. (III-9a) with  $\beta = 0.368$ , as shown in Fig. III-7b. The relationship is seen to be valid over at least two decades, from  $T_c - T = 0.1^\circ$  to  $10^\circ$ .

The critical temperature exponent  $\delta$  is determined directly from measurement of the magnetic moment vs internal field at  $T = T_c$ . The results of this measurement, as given in Fig. III-8, correspond to  $\delta = 4.46$ .

The initial susceptibility in the region immediately above the Curie temperature was determined by measuring the magnetic moment as a function of temperature at several fields and extrapolating the  $\sigma^2$  vs  $H/\sigma$  isotherms obtained to  $H = 0$ . The resultant values of  $\chi_o$  were analyzed by two distinct methods. The first was the  $T^*$  technique introduced by Kouvel and Fisher.<sup>16</sup> This involves the determination of  $T^* = \chi_o^{-1}/d\chi_o^{-1}/dT$  as a function of temperature. Defining a temperature-dependent effective exponent  $\gamma^*(T) = (T - T_c)/T^*$ , then  $\gamma^*(T) = \gamma$  in the limit  $T = T_c$ . A computer program was written to evaluate  $\gamma^*(T)$  according to this procedure, and

---

<sup>†</sup>This crystal was grown by T. B. Reed.

Section III

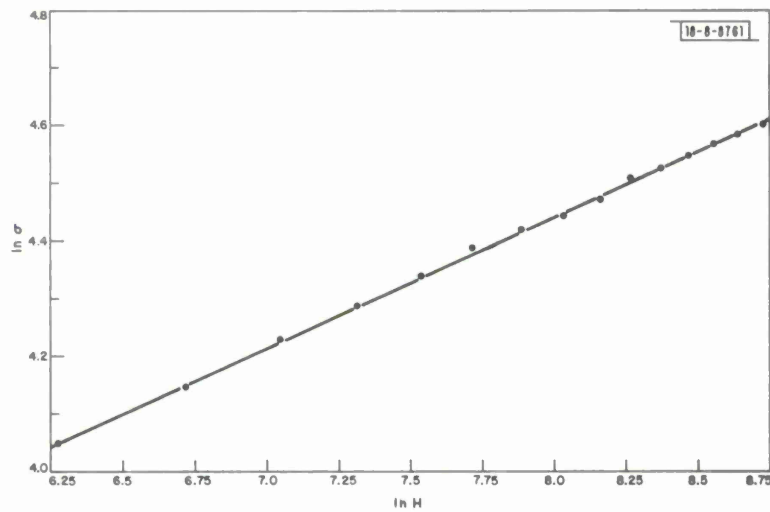


Fig. III-8. Magnetic moment  $\sigma$  vs internal magnetic field in EuO at  $T = T_c$ . Slope corresponds to  $\delta = 4.46$ .

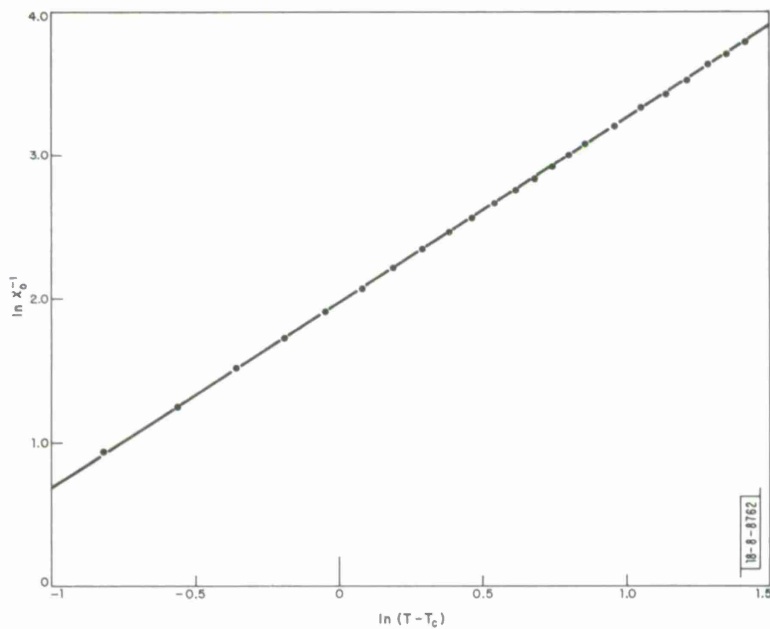


Fig. III-9. Inverse of initial susceptibility  $\chi_o$  vs  $T - T_c$ , assuming  $T_c = 69.594^\circ\text{K}$ . Slope corresponds to  $\gamma = 1.285$ .

it was found that for  $T_c = 69.59^\circ\text{K}$ , the value of  $\gamma$  was essentially constant and equal to  $1.278 \pm 0.002$  for  $T - T_c$  between 0.6 and  $4^\circ\text{K}$ . At higher temperatures  $\gamma^*$  decreases with increasing temperature.

A second method involved the assumption that  $\gamma$  remains constant over the temperature interval being measured, and the use of a computer to obtain a direct determination of the best values of  $\gamma$  and  $T_c$  on the basis of our data and Eq. (III-9c). The resultant value from this method is  $\gamma = 1.285$  with a Curie temperature  $T_c = 69.594^\circ\text{K}$ . Most importantly, all the theoretical values of  $\chi_0^{-1}$  for an exact fit with these values fall within the experimental error of the values measured. The nature of the agreement is indicated by the logarithmic plot of  $\chi_0^{-1}$  vs  $T_c - T$  shown in Fig. III-9. On the basis of these results, we can conservatively bracket the value of the  $\gamma$  by setting  $\gamma = 1.282 \pm 0.008$ .

These results agree with the scaling law prediction<sup>17</sup>  $\gamma = \beta(\delta - 1)$  to well within experimental uncertainty. The scaling laws further predict that  $\alpha = 2 - \beta(\delta + 1) = -0.009 \approx 0$ , where  $\alpha$  is defined in terms of the magnetic specific heat  $C_M$  near  $T_c$  by  $C_M \propto |T - T_c|^{-\alpha}$ . For  $\alpha = 0$ , a logarithmic dependence  $C_M \propto \ln |T - T_c|$  is expected, and is observed<sup>18</sup> in EuO for  $T > T_c$ . However, this apparent agreement is clouded by the fact that a logarithmic dependence is not observed for  $T < T_c$ .

An investigation has been initiated to determine whether our data above  $T_c$  can be fitted to a single magnetic equation of state. Preliminary results indicate that this can be done, and that a further transformation of the data by the method introduced by Schofield<sup>19</sup> yields a straight line relationship. Data taken for  $T < T_c$  is now being analyzed to see if a single linear relationship can describe the data both above and below  $T_c$ .

N. Menyuk  
K. Dwight

## 2. Impurity Magnon Modes in $\text{KNiF}_3:\text{Mn}$

We have continued our study of two-magnon Raman scattering in  $\text{KNiF}_3$  (Ref. 20) by using samples doped with  $\text{Mn}^{2+}$  impurities. In addition to the intrinsic two-magnon excitation previously seen in the pure samples, we observe a relatively narrow line shifted from the  $5145\text{-}\text{\AA}$  excitation by an energy  $\sim 550\text{ cm}^{-1}$ . This is well below the maximum energy of the intrinsic two-magnon line,  $850\text{ cm}^{-1}$ . Only diagonal elements of the scattering tensor have been observed for the impurity excitation. Samples having two different impurity concentrations, 3.7 percent and  $\sim 2$  percent (atomic), were studied; the impurity mode intensity was stronger in the higher concentration sample. This line disappeared at temperatures approaching  $T_N = 253^\circ\text{K}$ .

From its temperature dependence and energy, it seems likely that this is a two-magnon excitation associated with the  $\text{Mn}^{2+}$  impurities, most probably with one spin excitation on the impurity and another on the surrounding intrinsic spins. This situation differs from the previously reported case<sup>21</sup> of  $\text{KMnF}_3:\text{Ni}$  since the two-magnon  $s_o + d$  impurity mode observed there was a true local mode, lying above the intrinsic two-magnon band. The present situation in which the impurity-host exchange constant is less than the host constant, and in which an impurity spin excitation lies within the host magnon band, should result in resonant or virtual<sup>22</sup> modes.

A complete theoretical treatment of this problem must include not only the different spin and exchange of the impurity, but magnon-magnon binding<sup>23</sup> as well. Since the approximations which

### Section III

entered the theoretical Green's function treatment<sup>24</sup> of KMnF<sub>3</sub>:Ni may not be valid for KNiF<sub>3</sub>:Mn, we are presently examining this theory in the general case where single magnon local modes may not occur.

S. R. Chinn  
H. J. Zeiger  
J. R. O'Connor

#### 3. Raman Scattering in CsMnF<sub>3</sub>

The Raman spectrum of the antiferromagnet CsMnF<sub>3</sub> has been observed using 4880-Å radiation from an argon ion laser. This compound, which is isomorphic with the ferrimagnet RbNiF<sub>3</sub>, whose Raman spectrum has also been observed,<sup>24,25</sup> belongs to the space group D<sub>6h</sub><sup>4</sup> and has 30 atoms per unit cell. Of the possible 19 Raman active phonon modes<sup>25</sup> we have so far tentatively identified 5 E<sub>1g</sub>, 5 A<sub>1g</sub>, and 7 E<sub>2g</sub> modes ranging in energy from 47 cm<sup>-1</sup> to 470 cm<sup>-1</sup>. Several of these modes have a marked temperature dependence, with observed linewidths increasing from the instrumental linewidth ( $\sim 3$  cm<sup>-1</sup>) to  $\sim 20$  cm<sup>-1</sup>, as the temperature is raised from 5°K to 300°K. Small energy shifts also occur in some of these modes in this temperature range. These features suggest that anharmonic interactions are quite large in this material, and we are presently investigating this question in a more quantitative fashion.

CsMnF<sub>3</sub> orders antiferromagnetically below 53.5°K.<sup>26</sup> A Raman mode has been observed whose shape, position, temperature dependence and polarization indicate that it arises from the excitation of two magnons. Maximum intensity occurs near an energy shift of 93 cm<sup>-1</sup> at low temperature, and the line broadens, shifts to lower energy, and decreases in intensity as the temperature approaches T<sub>N</sub>. The line shape suggests that magnon-magnon interactions are also important in this material. The low temperature energy of this excitation is also consistent with the approximate energy of two high-density-of-states, zone-edge magnons, as determined using exchange constants found by Seavey.<sup>27</sup>

S. R. Chinn

#### C. LASER SCATTERING

##### 1. Light Scattering from Acoustic Plasma Waves and Single-Electron Excitations in Magnetoplasmas

In an effective mass approximation, the differential cross section for the Stokes scattering of light from low temperature electrons in an n-type spherical band semiconductor, with or without a DC magnetic field  $\vec{B}_0$ , is given approximately by

$$\frac{d^2\sigma}{d\Omega d\omega} \approx (\vec{\epsilon}_F \cdot \vec{\epsilon}_I)^2 \sigma_T^* \left( \frac{\hbar q^2 V \epsilon_\infty^2}{4\pi^2 e^2} \right) \text{Im} \left[ \frac{1}{\epsilon(\omega, \vec{q})} \right] \quad (\text{III-10})$$

where  $\vec{\epsilon}_F$  and  $\vec{\epsilon}_I$  are the incident and scattered light polarization vectors,  $\omega = \omega_I - \omega_F$ ,  $\vec{q} = \vec{q}_I - \vec{q}_F$ ,  $\sigma_T^* = (e^2/m^* c^2)^2$  is the effective Thomson cross section, and  $\epsilon(\omega, \vec{q})$  is the longitudinal dielectric constant. The light effectively couples to longitudinal density fluctuations of the Fermi gas, and the scattering shows the peaks of  $\text{Im}(1/\epsilon)$ . For long wavelengths and zero magnetic field the cross section exhibits (1) broad quasi-elastic scattering of single electrons from just inside to just outside the Fermi surface in the frequency range  $0 < \omega \lesssim qv_F$ ; and (2) plasmon scattering near  $\omega = \omega_p$ , the electron plasma frequency. Both of these scattering

processes have been observed.<sup>28,29</sup> If a strong magnetic field is applied to the electron plasma, so that the Landau orbital quantization is important and the geometry  $\vec{q} \parallel \vec{B}_0$  is considered, the scattering spectra peaks occur in the same frequency bands. One expects plasmon scattering at  $\omega = \omega_p$  and quasi-elastic scattering in the range  $0 < \omega \lesssim qv_F$ . However, the nature of the quasi-elastic scattering is drastically altered (see Ref. 30 for a discussion of the qualitative features of this scattering). The electrons on each occupied Landau level effectively become a one-dimensional electron gas, and the single-electron scattering has multiple peaks at  $\omega = qv_{Fn\sigma}$ , where  $v_{Fn\sigma}$  is the velocity along  $\vec{B}_0$  of an electron at the Fermi surface with Landau orbital quantum number  $n$  and spin  $\sigma$ . Furthermore, for long relaxation times the quasi-elastic scattering will have additional peaks due to the excitation of longitudinal acoustic plasma waves at frequencies in between the single electron peaks. The acoustic plasma wave scattering results from a low frequency zero of the longitudinal dielectric constant. Several authors<sup>31-33</sup> have independently suggested the existence of such waves, but they have not been observed. Neither of the above features of magnetoplasma quasi-elastic light scattering have been observed. Although Wolff<sup>34</sup> has given some theoretical discussion of this scattering in addition to that given in Ref. 30, no detailed spectra have been calculated and a number of features of the magneto-plasma scattering have not been discussed. With these matters in mind, we have made some preliminary calculations of the quasi-elastic scattering spectra using Eq. (III-10) to treat scattering from electrons in n-type InSb.

Because of the multiplicity of scattering resonances in the frequency range  $[0, qv_F]$  the inclusion of relaxation effects in the calculation of  $\epsilon(\omega, \vec{q})$  is important. For very short relaxation times the multiple peaks may strongly overlap, yielding a broad, smooth spectrum similar to that found for zero magnetic field. For simplicity, we use a relaxation time ansatz with a constant relaxation time  $\tau$  in the equation of motion for the density matrix (which is used to derive  $\epsilon$ ). The use of the relaxation time ansatz in quantum transport theory has some hazards. Very simple forms fail (1) to be gauge invariant and/or (2) to conserve charge density.<sup>35</sup> Green, et al.,<sup>36</sup> have given one reasonably satisfactory formulation for the conductivity problem. However, their ansatz does not conserve the spin density, as would be expected for orbital relaxation processes. We have modified their treatment to eliminate this difficulty and find for  $\epsilon$ ,

$$\epsilon(\omega, \vec{q}) = \epsilon_\infty - \frac{4\pi e^2}{q^2} (1 + i\omega\tau) \sum_{\sigma} \frac{K_\sigma^{(1)} K_\sigma^{(2)}}{K_\sigma^{(1)} + i\omega\tau K_\sigma^{(2)}} \quad (\text{III-11})$$

where

$$K_\sigma^{(1)} = \sum_{\alpha, \beta} |\langle \alpha\sigma | e^{i\vec{q} \cdot \vec{r}} | \beta\sigma \rangle|^2 \left[ \frac{f_{\beta\sigma} - f_{\alpha\sigma}}{\hbar(\omega - i/\tau) + E_{\beta\sigma} - E_{\alpha\sigma}} \right] \quad (\text{III-12})$$

and

$$K_\sigma^{(2)} = \sum_{\alpha, \beta} |\langle \alpha\sigma | e^{i\vec{q} \cdot \vec{r}} | \beta\sigma \rangle|^2 \left[ \frac{f_{\beta\sigma} - f_{\alpha\sigma}}{E_{\beta\sigma} - E_{\alpha\sigma}} \right] \quad (\text{III-13})$$

with  $|\alpha, \sigma\rangle$  the eigenstate of the electron effective mass Hamiltonian  $[H|\alpha\sigma\rangle = E_{\alpha\sigma}|\alpha\sigma\rangle]$  and  $f_{\alpha\sigma}$  the Fermi occupation factor.

### Section III

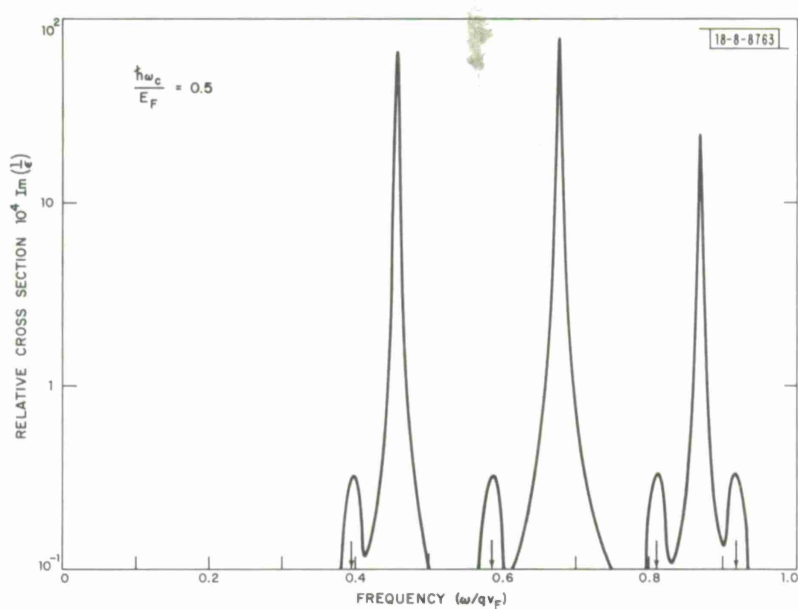


Fig. III-10. Relative cross section vs frequency for InSb for a fixed magnetic field and  $qv_F\tau = 500$ .

Figures III-10 and III-11 show relative scattering spectra computed for InSb with the following parameters:  $\lambda_1 = 10 \mu$ ,  $m^*/m = 0.015$ ,  $g^* = 50$ ,  $\epsilon_\infty = 16$ ,  $n_e = 10^{17} \text{ cm}^{-3}$ . The curve in Fig. III-10 was calculated for a very long relaxation time,  $qv_F\tau = 500$ , and illustrates the features described above. The three strong peaks each result from excitation of an acoustic plasma wave and dominate the scattering. The four small peaks result from single-electron excitations on each of the four occupied Landau levels. Note the correlation of the latter peaks with the values of  $qv_{Fn\sigma}$  which are marked by the arrows. Figure III-11 shows the development of the spectra as the magnetic field is varied for a fixed  $qv_F\tau = 10$ . For a field such that there are  $N$  occupied Landau levels there are  $(N - 1)$  acoustic waves. Since the acoustic wave scattering is dominant, there are  $(N - 1)$  scattering peaks. As the field increases there are fewer and fewer levels occupied and, therefore, fewer scattering peaks. The existence of an acoustic wave requires the occupation of more than one level, since, roughly, the wave involves the motion of electrons on different Landau levels in a manner yielding an almost charge-neutral wave. For  $\hbar\omega_c/E_F = 1.5$ , only one Landau level is occupied, no acoustic waves exist, and the scattering is dramatically reduced to a broad smear.

Although this model calculation illustrates some of the general features of magnetoplasma quasi-elastic scattering, it is not expected to be quantitatively accurate for InSb. A value of  $qv_F\tau = 10$  is optimistic by a factor of five for  $10 \mu$  light and typical  $n$ -InSb. For  $qv_F\tau = 2$ , the spectra of Fig. III-11 are strongly smeared and tend to become lost in the wings of the plasmon scattering. Also, coupling mechanisms involving the spin degree of freedom and spin-orbit coupling are important in real semiconductors,<sup>29,37,30,34</sup> and are not treated here. These mechanisms can significantly alter the order of magnitude of the cross section, the polarization selection rules, and the nature of the lineshapes. A more realistic calculation extending the treatments of Refs. 30 and 34 is in progress.

F. A. Blum  
R. W. Davies

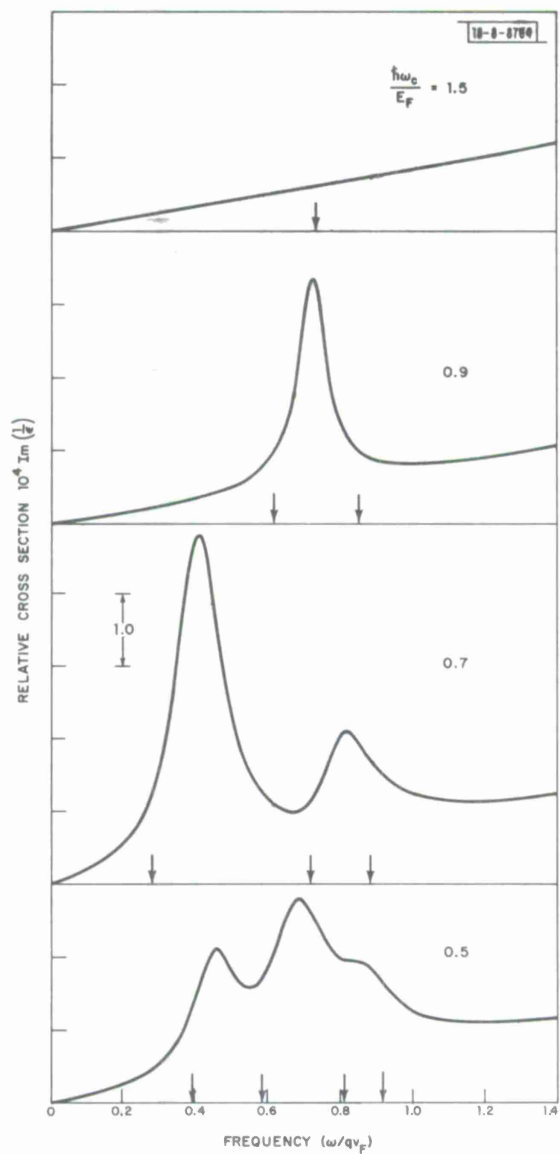


Fig. III-11. Relative cross section vs frequency for InSb with magnetic field as a parameter and  $qv_F\tau = 10$ .

### Section III

#### 2. Millimeter and Far Infrared Frequency Mixing in GaAs

Heterodyne experiments with both millimeter and infrared sources have been performed in high purity, epitaxial GaAs. The millimeter waves produce avalanche breakdown, and mixing via hot electrons is observed. At laser frequencies the DC bias level determines whether detection proceeds via a similar hot electron mechanism or through photothermal ionization of shallow donor states. The time constant associated with the latter process is significantly faster than the hot carrier relaxation.

At 4 mm, which corresponds to  $\sim 0.3$  meV, the response of GaAs cannot take place by the photothermal ionization of shallow impurity levels. However, since the conduction electron scattering time is approximately  $10^{-12}$  sec ( $\sim 170$  GHz), the comparatively slow 4-mm radiation can transfer energy to the electrons and induce impact ionization. Mixing (and detection) can then proceed via a hot electron mechanism which has been extensively investigated in InSb.<sup>38</sup> Two 4-mm sources, a DX-151 klystron and a CSF carcinotron, were combined in a 4-mm waveguide directional coupler and the resulting radiation transmitted down a lightpipe to the detector immersed in liquid helium at 4.2 °K. The IF signal resulting from the mixing was fed into a spectrum analyzer and measured between 0.1 and 40 MHz. Stabilization to a particular IF frequency was provided by a 10-MHz syncriminator which controlled the reflector voltage of the klystron. The 10 MHz was obtained by mixing the IF signal with a local oscillator in a balanced diode mixer. In order to insure independence of possible amplitude variations in the primary beams, a constant IF signal was maintained on a reference silicon crystal diode.

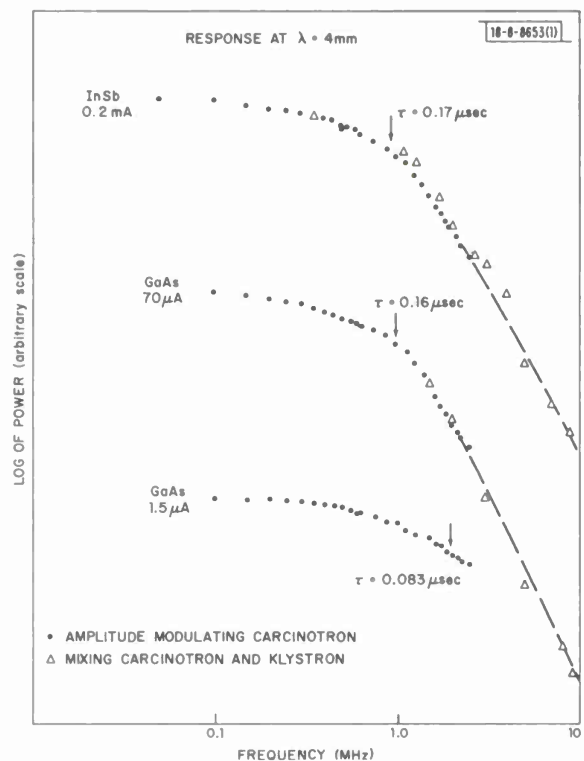


Fig. III-12. IF power versus IF frequency for InSb and GaAs at two DC bias levels.

A second method used to measure the microwave frequency response of GaAs was to sinusoidally amplitude modulate the carcinotron between 0.1 and 2.5 MHz by varying the anode voltage. This resulted in a depth of modulation of about 10 percent. In order to obtain response time curves for these high impedance devices, care was taken in all measurements to load the detectors with a low impedance, wide band amplifier.

The IF signal frequency roll-off of InSb and GaAs at two bias levels is shown in Fig. III-12. Values determined for InSb are in good agreement with previous measurements and quite similar to GaAs at high bias levels. At very low bias levels a definite decrease in GaAs time constant conforms with the usual model that at high electric fields hot carrier effects can increase the lifetime. Additional insight into the origin of the carriers active in microwave mixing is obtained from the I-V curves of Fig. III-13(a) and 13(b). In these curves a dramatic reduction of the DC bias voltage at breakdown occurs with increasing microwave power. Since  $1\text{ mW/cm}^2$  of

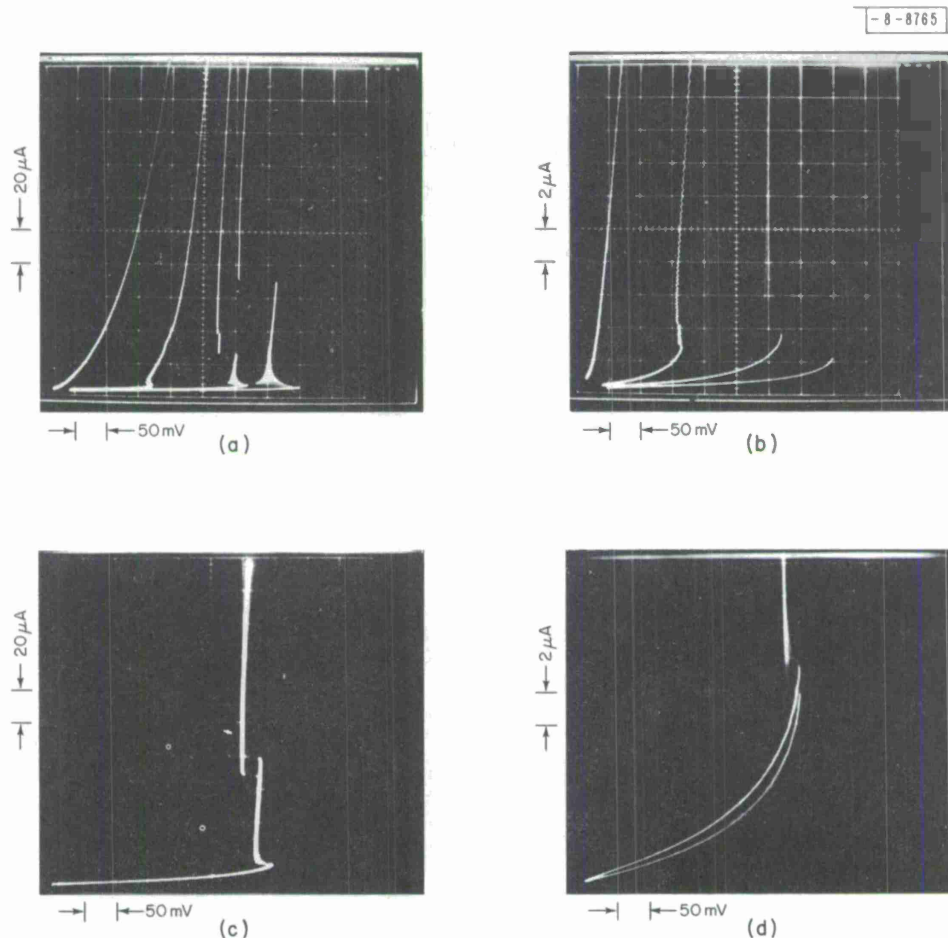


Fig. III-13.  $I$  vs  $V$  curves of GaAs. (a) From left to right, 4-mm radiation of 10, 5, and 2.5 mW and no radiation. (b) Same as (a) with vertical scale changed. (c)  $I$  vs  $V$  curve with  $\sim 3$  mW HCN laser radiation ( $20 \mu\text{A}/\text{div}$ ). (d) Same as (c) but with  $2 \mu\text{A}/\text{div}$ . Note that laser radiation causes increase in photoconductivity with little change in breakdown voltage.

4-mm radiation is equivalent to approximately 1 volt/cm, the total electric field (microwave plus DC) required for breakdown remains constant. The 10 mW of microwave power actually used in these mixing experiments was therefore sufficient (even at the lowest DC bias) to induce impact ionization and generate free carriers in the detector.

In Figs. III-13(c) and 13(d) the effects of HCN laser radiation on the I-V curves of GaAs differ markedly from those of the microwaves. The 890-GHz laser radiation cannot cause impact ionization but rather a change in conductivity which results from the photo-ionization of shallow donor levels into the conduction band.<sup>39</sup> To further investigate the response at these wavelengths the outputs of two HCN lasers were combined in a TPX beam splitter and directed onto the GaAs. The mixed IF signal was displayed on a spectrum analyzer as the lasers were tuned apart in frequency. Because of the limited width of the spontaneous HCN emission line, laser oscillation could only be maintained up to a separation of 4 to 5 MHz. In Fig. III-14 the laser beats are displayed as a function of frequency up to 2.5 MHz. The InSb and GaAs biased above breakdown show an IF frequency fall-off below 1 MHz. At high bias the GaAs response time is associated

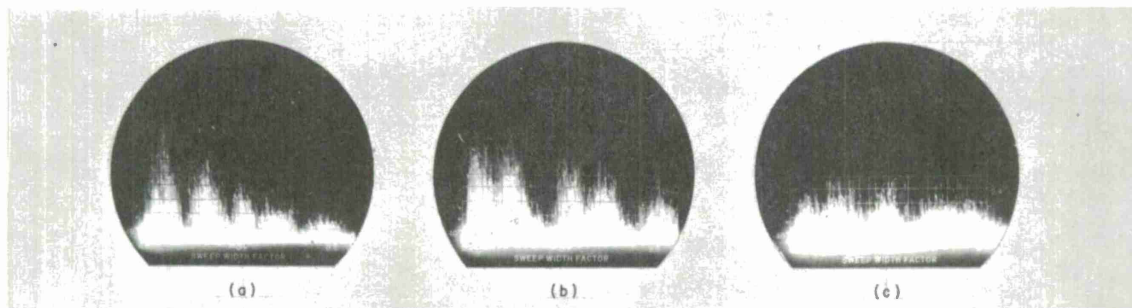


Fig. III-14. Output of spectrum analyzer (0 to 2.5 MHz). Photographs represent a superposition of 2-sec exposures at each of 5 frequency settings. Mixing signals of two HCN lasers are obtained from (a) InSb (bias = 0.2 ma), (b) GaAs above breakdown ( $70\ \mu\text{a}$ ), (c) GaAs below breakdown ( $1.5\ \mu\text{a}$ ). Response in the last case extends beyond 4 MHz.

with hot electron relaxation to the equilibrium distributed in the conduction band. Below breakdown, the response takes place via a photo-ionization mechanism. In this case, after correcting for variation in primary laser power drop-off, the IF signal shows essentially flat response well out to 4.0 MHz ( $\tau < 40\ \text{nsec}$ ). The recombination to shallow donor states in this case had already been shown to be faster than  $1\ \mu\text{sec}$  by means of a germanium impact ionization modulator, and estimated to be as short as  $10\ \text{nsec}$  by pulsed ionization measurements in GaAs.<sup>40</sup>

H. R. Fetterman  
P. E. Tannenwald  
C. D. Parker

### 3. Nonlinear Effects on the Polarization and Linewidth of Intense Broadband Maser Signals

The circular polarization properties of the many galactic sources of maser emission by interstellar OH molecules has eluded simple explanation. Explanations of three types have been proposed: first, that the maser is being pumped by circularly polarized sources; second, that systematic Doppler shifts and Zeeman splitting along the propagation path produces significant maser gain for only one sense of circular polarization; and third, that nonlinear competition between opposite circularly polarized signals is occurring, as in saturated laser amplifiers in the laboratory. Without cataloging their shortcomings, let it suffice to say that all three explanations do not correlate well with the observations and are not free of theoretical objections. However, a new means of nonlinear competition, parametric down-conversion of one Zeeman-split microwave mode into the lower frequency microwave mode, and an electron cyclotron idler-wave, seem to provide an adequate explanation of the observations. This process does not require, as in the laboratory case, Raman-type cross saturation, which is negligible for these signals because they have bandwidths that are much larger than the inverse-lifetimes of the maser molecular states. The current-source for the low frequency cyclotron wave is driven by the  $\vec{v} \times \vec{B}$  force due to two phase matching microwave Zeeman modes. Details will appear soon in The Physical Review.<sup>41</sup>

Further work on nonlinear effects deals with the linewidth of a broadband maser signal when the maser amplifier becomes saturated. The expected line narrowing by a factor  $(\ln A)^{-1/2}$ , where  $A$  is the amplification, gives way to a line broadening due to saturation. The appropriate spectral power output for a saturated two-level maser amplifier has been calculated from

approximate solutions to an integral equation that is obtained from the equations of motion for the density matrix for a two-level system and for Gaussian statistics for the signal. The following were considered: the signals are either quasi-monochromatic or broadband relative to the inverse-lifetimes of the states, the molecular line broadening is either homogeneous or inhomogeneous, and the saturation rate is either much less or much greater than the signal bandwidth. The results for the case of inhomogeneous broadening, broadband signals, and moderate saturation have been used to obtain the saturated linewidth and intensity for the OH and H<sub>2</sub>O travelling-wave masers as a function of amplifier length. This should be helpful in understanding the many observations.

M. M. Litvak

#### REFERENCES

1. P.N. Butcher, Proc. Phys. Soc. (London) A64, 765 (1951); A.O.E. Animalu, Phys. Rev. 163, 557 (1967).
2. M.J.G. Lee and L.M. Falicov, Proc. Phys. Soc. A304, 319-334 (1968).
3. C.Y. Young, Phys. Rev. (to be published).
4. J.M. Ziman, Proc. Phys. Soc. 86, 337 (1965).
5. N.W. Ashcroft, Phys. Rev. 140, 935 (1965).
6. N.V. Smith, Phys. Rev. 183, 634 (1969).
7. J.M. Honig and T.B. Reed, Phys. Rev. 174, 1020 (1968), DDC AD-685692, and references contained therein.
8. Solid State Research Report, Lincoln Laboratory, M.I.T. (1970:1),
9. T.A. Kaplan and P.N. Argyres, Int. J. Quan. Chem. III S, 851 (1970).
10. T.A. Kaplan and R.A. Bari, J. Appl. Phys. 41, 875 (1970).
11. J. Hubbard, Proc. Roy. Soc. A281, 401 (1964).
12. N.F. Mott, Phil. Mag. 6, 287 (1961).
13. D.M. Larsen and E.J. Johnson, J. Phys. Soc. Japan 21S, 443 (1966), DDC AD-646484.
14. R.C. Brandt and D.M. Larsen, private communication.
15. M. Rayl and P.T. Wojtowicz, Phys. Letters 28a, 142 (1968).
16. J.S. Kouvel and M.E. Fisher, Phys. Rev. 136, A1626 (1964).
17. R.B. Griffiths, Phys. Rev. 158, 176 (1967).
18. D.T. Teaney, Critical Phenomena, edited by M.S. Green and J.V. Sengers (National Bureau of Standards, 1965), pp. 50-57.
19. P. Schofield, Phys. Rev. Letters 22, 606 (1969).
20. S.R. Chinn, H.J. Zeiger, and J.R. O'Connor, J. Appl. Phys. 41, 894 (1970).
21. M.F. Thorpe, Phys. Rev. Letters 23, 472 (1969).
22. T. Wolfram and J. Callaway, Phys. Rev. 130, 2207 (1963).
23. R.J. Elliott and M.F. Thorpe, J. Phys. C 2, 1630 (1969).
24. S.R. Chinn and H.J. Zeiger, Phys. Rev. Letters 21, 1589 (1968), DDC AD-688025.
25. P.A. Fleury, J.M. Worlock, and H.J. Guggenheim, Phys. Rev. 185, 738 (1969).

### Section III

26. K. Lee, A.M. Portis and G.L. Witt, Phys. Rev. 132, 144 (1963).
27. M.H. Seavey, Phys. Rev. Letters 23, 132 (1969).
28. A. Mooradian and A.L. McWhorter, in Light Scattering Spectra of Solids, edited by G.B. Wright (Springer, New York, 1969), p.297, DDC AD-695752; A. Mooradian, ibid., p.285.
29. D.C. Hamilton and A.L. McWhorter, ibid., p.309.
30. F.A. Blum, Phys. Rev. 1, 1125 (1970).
31. A.L. McWhorter and W.G. May, IBM J. Res. Develop. 8, 285 (1965).
32. V.L. Ginsburg, O.V. Konstantinov and V.I. Perel, Sov. Phys. - Solid State 9, 1684 (1968); O.V. Konstantinov and V.I. Perel, Sov. Phys. - JETP 26, 1151 (1968).
33. G. Benford and D. Book, Phys. Rev. Letters 21, 898 (1968).
34. P.A. Wolff, Phys. Rev. (to be published).
35. S. Tosima, J.J. Quinn and M.A. Lampert, Phys. Rev. 137, A833 (1965).
36. M.P. Green, H.J. Lee, J.J. Quinn and S. Rodriguez, Phys. Rev. 177, 1019 (1969).
37. Y. Yafet, Phys. Rev. 152, 858 (1966); G.B. Wright, P.L. Kelley and S.H. Groves, in Light Scattering Spectra of Solids, edited by G.B. Wright (Springer, New York, 1969), p.335; V.P. Makarov, Sov. Phys. - JETP 28, 366 (1969).
38. E. Putley, Phys. Stat. Sol. 6, 571 (1964).
39. G.E. Stillman, C.M. Wolfe and J.O. Dimmock, Solid State Commun. 7, 921 (1969), DDC AD-693903.
40. G.E. Stillman, C.M. Wolfe, I. Melngailis, C.D. Parker, P.E. Tannenwald and J.O. Dimmock, Appl. Phys. Letters 13, 83 (1968), DDC AD-681589.
41. M.M. Litvak, Phys. Rev. (to be published).

## IV. MICROELECTRONICS

### A. ALUMINUM BEAM LEADS AND BEAM-LEAD CROSSOVERS ON CERAMIC

Beam leads and beam-lead crossovers have been fabricated on ceramic substrates using gold metallization systems.<sup>1-3</sup> However, because of the potential problems and failure modes associated with bonds between gold beams and the aluminum metallization on an integrated circuit chip, a program to develop a technique for forming interconnections, crossovers and beam leads on ceramic substrates using an all aluminum metallization system has been pursued.

The ceramic substrates are prepared either by ultrasonically drilling the required holes in as-fired, 99.5 percent  $\text{Al}_2\text{O}_3$  with an 8-micro-inch or better surface finish, or by having the ceramic manufacturer prepunch the holes in green ceramic tape before firing. The latter method is preferred as it greatly reduces the amount of cracking encountered during subsequent processing of the substrate.

In order to form the beam leads over the holes in the ceramic, the hole must be filled or covered (tent) with a material that can be leached away without affecting the aluminum. The low-melting glass used as a filler material for gold beam lead fabrication cannot be used because the HF used to leach the glass will rapidly attack aluminum. A promising material that has been used to tent the holes is Riston, a sheet photoresist product of DuPont. The photoresist sheet is applied to the entire substrate and exposed, leaving squares slightly larger than, and covering the holes. Using a filament evaporator, 75,000 to 100,000 Å of aluminum are deposited on the substrate. The interconnection pattern (minus crossovers) and beam leads are delineated and etched using standard photolithographical techniques. The Riston is removed using either commercial photoresist strippers that do not attack aluminum, or an oxygen-plasma photoresist asher. The latter method is much preferred because of its speed and the completeness of the Riston removal, a prerequisite for reliable beam to chip-pad bonding.

The technique used to apply the Riston is quite critical. The ceramic is degreased in boiling trichloroethylene, rinsed in three separate beakers of electronic grade methanol, and blown dry with nitrogen. The substrate is then preheated for 15 minutes at 80°C and the Riston preheated at 80°C for 2 minutes. After pressing the heated Riston onto the heated substrate, the substrate is placed Riston side down on a smooth ceramic plate and baked for 15 minutes at 120°C, and then baked another 15 minutes at 120°C with the Riston side up. The substrate is then removed from the oven and allowed to cool. After exposure with collimated light from a high pressure mercury arc lamp, the Riston is spray developed and the excess developer blown off with nitrogen. The exposed and developed Riston is post-baked for 10 minutes at 180°C before loading into the evaporator for aluminum deposition.

The technique for forming air-gap, beam-leaded crossovers with aluminum is similar in philosophy to that used for beam-leaded crossovers with gold.<sup>3</sup> However, photoresist KTFR is used as the leachable base for forming the crossover instead of copper. The entire interconnection and beam-lead pattern is coated with 40,000 to 60,000 Å of KTFR, and holes down to the pads of the interconnection pattern where the crossovers will make contact are exposed and developed in the photoresist. The substrate is then baked at 180°C for 30 minutes to thoroughly remove all the solvents from the KTFR. 50,000 to 75,000 Å of aluminum are evaporated over the entire

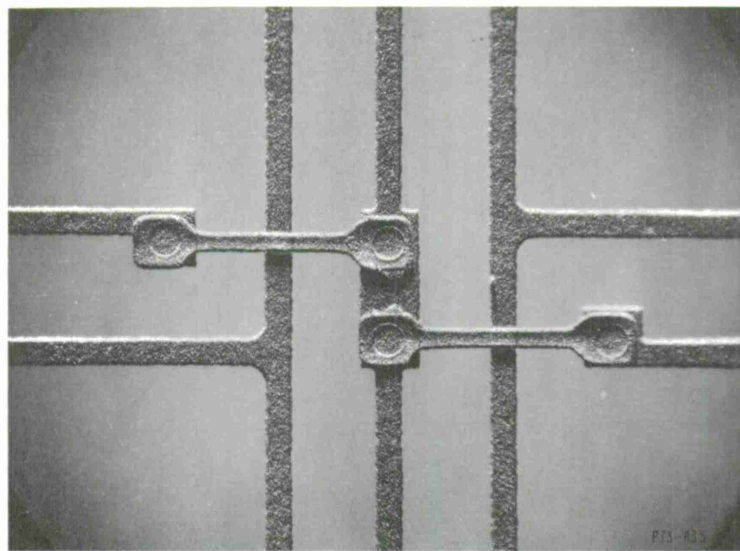


Fig. IV-1. Aluminum beam-leaded crossover.

substrate, keeping the substrate temperature at approximately 100°C. The crossover pattern is delineated and etched using standard photolithographic techniques, and all the photoresist removed using commercial strippers or an oxygen-plasma, dry photoresist ash. The final step is to sinter the aluminum to aluminum contacts between the crossovers and the interconnection pattern for 10 minutes in nitrogen at 575°C. Figure IV-1 shows the aluminum beam-leaded crossover.

F. J. Bachner

#### B. PASSIVATED MESA TECHNIQUE

Most semiconductor devices and monolithic integrated circuits are fabricated using the planar process which by its nature affects total protection of the sensitive diffused junctions during as well as after various process steps. Mesa devices have many desirable advantages over planar devices and are used primarily to achieve special performance characteristics not possible with planar techniques. However, the mesa process results in exposed junctions and no practical passivation method has been developed that fully protects the junctions. The process described here is a combination of the mesa and planar which incorporates all the advantages of the two processes. This process is given the acronym SIMTOP for the Silicon Nitride ( $\text{Si}_3\text{N}_4$ ) Masked, Thermally Oxidized, Post Diffused Mesa Process. The process procedure is basically as follows: A silicon wafer is deposited with a thin layer of  $\text{Si}_3\text{N}_4$  (Ref. 4). The  $\text{Si}_3\text{N}_4$  is etched<sup>5</sup> to form a desired geometry using photolithography and the appropriate etchants. The mesa is then formed by etching the silicon. The resulting mesa will have smooth crystallographic planes if the silicon material is  $\langle 100 \rangle$  orientation and is etched using an anisotropic etch.<sup>6-8</sup> Then the silicon is thermally oxidized to a thickness of 8,000 to 10,000 Å. The  $\text{Si}_3\text{N}_4$  is removed<sup>9</sup> and the p-n junction formed by diffusion. The metallized contacts are formed by evaporating or plating the appropriate metal, Al, Ni-Au, Cr-Au, etc. Figure IV-2 shows the cross section of a SIMTOP device and Fig. IV-3 the top view.

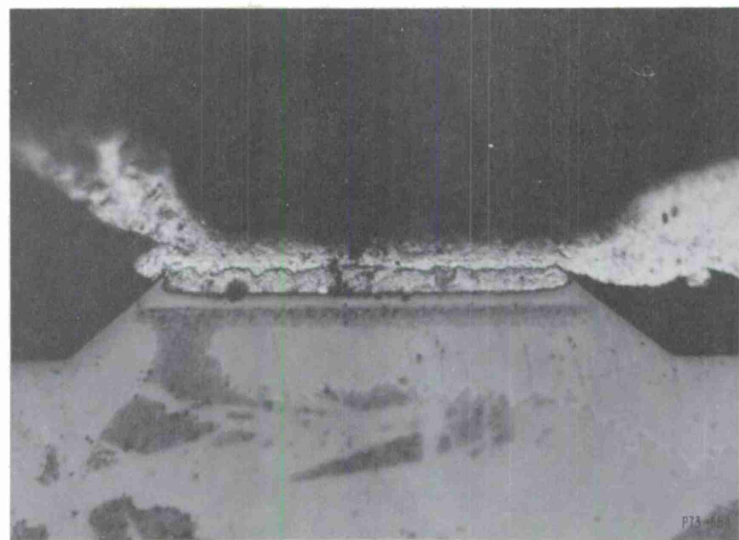


Fig. IV-2. Cross section of a SIMTOP device.

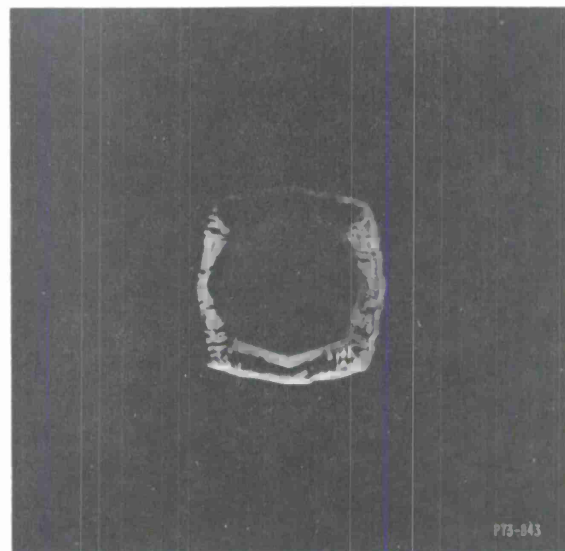


Fig. IV-3. Top view of a SIMTOP device.

## Section IV

The post-diffusion feature of this mesa process results in devices which have all the advantages of the planar process; high reliability, uniform electrical and physical characteristics and fabrication simplicity. In addition, the mesa structure eliminates the curved junction and lateral space-change widening typical of planar structures and provides lower capacitance and high breakdown voltages. Reliability is enhanced over the prior mesa process since the crystallographic planes of this mesa structure tend to reject impurities and contamination which would be incorporated in the subsequent oxidation. Since the junction formation is similar to the planar p-n junction formation, no difference in reliability is anticipated. Thermal properties should be enhanced when these devices are mounted junction side down since the entire mesa top is metallized and contact oxide on the surface is not required as it is for deposited glass or thermal oxide grown on normal mesa devices. The thermal oxide in these SIMTOP devices is confined to the slopes of the mesa only.

An Impatt diode was fabricated with this process to illustrate the feasibility of the process. Although the diode design was not optimized for X-band it did oscillate in X-band in a CW mode and more important, it did exhibit stable sharp reverse breakdown voltage at low leakage and good forward voltage drop in either conventional or flip mounted configuration. The diode absorbed and dissipated 5 watts CW power although it was a small (2 pf at 0 volts) area device. It is expected that with further work in the microwave field, more efficient diodes will be fabricated which will also retain all the advantages of the SIMTOP process.

New geometrical designs such as the ring,<sup>10</sup> star, cross, grid or comb structures are possible in mesa form for devices such as the PIN, varactor, Impatt and Trapatt elements. The SIMTOP process also has considerable advantages in high voltage devices for high power and high frequency applications.

R. A. Cohen

### C. COMPUTER AIDED DESIGN AND DEVELOPMENT

Work on the Mannplot and Digitizer mask making programs has continued over the past quarter. The programs are continually being refined.

An on-line version of the CIRCUS circuit analysis program has essentially been completed. This program is designed to allow a circuit designer to enter circuit descriptions to the program via a time shared console and get back a limited analysis of his circuit's behavior interactively. Complete analyses may then be submitted for batch processing using the data entered through the time shared program. It is hoped that this will increase use of the CIRCUS program by making it easily accessible to all laboratory designers. Documentation will be distributed within the Laboratory and will also be available to all interested outside parties as soon as it is printed.

N. B. Childs

## REFERENCES

1. F. Bachner, R. A. Cohen, R. Mountain and R. E. McMahon, "A Beam Lead Substrate Package for a Six-Stage TTL Shift Register," *Microelectronics and Reliability* 8, 307 (1969).
2. F. Bachner, R. A. Cohen and R. E. McMahon, "Rigid and Nonrigid Beam Lead Substrates," *Solid-State Circuits Conf. Digest* (February 1970).
3. H. Besseches and A. Pfahl, "Crossovers for Interconnections on Substrates," *Proc. of 1969 Electron. Comp. Conf.*, Washington, D.C. 30 April – 2 May 1969.
4. T. L. Chu, J. R. Szedon and C. H. Lee, "The Preparation and C-V Characteristics of Si-Si<sub>3</sub>N<sub>4</sub> and Si-SiO<sub>2</sub>-Si<sub>3</sub>N<sub>4</sub> Structures," *Solid-State Electron.* 10, 897 (1967).
5. N. C. Tombs and F. A. Sewell, Jr., "Silicon Oxide as an Etching Mask for Silicon Nitride," *J. Electrochem. Soc.* 115, 101 (1968).
6. W. C. Roswold, W. H. Legat and R. L. Holden, "Air Gap Isolated Microcircuits – Beam Lead Devices," *Trans. IEEE ED-15*, 640 (1968).
7. J. C. Greenwood, "Ethylene Diamine-Catechol-Water Mixture Shows Preferential Etching of p-n Junction," *J. Electrochem. Soc.* 116, 1325 (1969).
8. D. B. Lee, "Anisotropic Etching of Silicon," *J. Appl. Phys.* 10, 4569 (1969).
9. V. Y. Doo, "Silicon Nitride, A New Diffusion Mask," *Trans. IEEE ED-15*, 561 (1966).
10. L. P. Marinaccio, "Ring-Geometry Impatt Oscillator Diodes," *Proc. IEEE Letters* 56, 1588 (1968).

UNCLASSIFIED

Security Classification

## **DOCUMENT CONTROL DATA - R&D**

(Security classification of title, body of abstract and Indexing annotation must be entered when the overall report is classified)

Printed by  
United States Air Force  
L. G. Hanscom Field  
Bedford, Massachusetts

